

Supporting Information

Co_{1-x}Fe_xO_y Oxygen Evolution Nanocatalysts: On the Way to Resolve (Electro)Chemically Triggered Surface-Bulk Discrepancy

Dino Aegerter,^{1*} Emiliana Fabbri,^{1*} Nur Sena Yüzbaşı,² Nataša Diklič,¹ Adam H. Clark,³ Maarten Nachtegaal,³ Cinthia Piamonteze,³ Jan Dreiser,³ Thomas Huthwelker,³ Thomas Graule² and Thomas J. Schmidt^{1,4}

¹Electrochemistry Laboratory, Paul Scherrer Institute, Forschungsstrasse 111, CH-5232 Villigen PSI, Switzerland.

²Laboratory for High Performance Ceramics, Empa - Swiss Federal Laboratories for Materials Science and Technology, CH-8600 Dübendorf, Switzerland.

³Photon Science Division, Paul Scherrer Institute, Forschungsstrasse 111, CH-5232 Villigen PSI, Switzerland.

⁴Institute of Molecular Physical Science, ETH Zurich, CH-8093 Zürich, Switzerland.

*Corresponding Authors: dino.aegerter@psi.ch & emiliana.fabbri@psi.ch

Table of Contents

Methods	S4
Material Syntheses	S4
Physicochemical Characterization of As-Synthesized Materials	S4
Electrochemical Characterization.....	S6
Operando / Ex Situ XAS and Ex Situ XRD	S7
Supporting Information Figures	S9
Figure S1	S9
Figure S2	S10
Figure S3	S10
Figure S4	S11
Figure S5	S11
Figure S6	S12
Figure S7	S13
Figure S8	S14
Figure S9	S15
Figure S10	S16
Figure S11	S17
Figure S12	S18
Figure S13	S19
Figure S14	S20
Figure S15	S21
Figure S16	S22
Figure S17	S23
Figure S18	S24
Figure S19	S25
Figure S20	S26
Figure S21	S27
Figure S22	S28
Figure S23	S29
Supporting Information Notes.....	S30
Note S1	S30
Note S2.....	S30
Note S3.....	S30
Note S4.....	S30
Note S5.....	S31
Note S6.....	S31
Note S7.....	S31
Note S8.....	S31
Note S9.....	S31
Note S10.....	S32
Note S11	S32
Note S12.....	S32
Supporting Information Tables.....	S33
Table S1	S33

Table S2S33

Table S3S33

Table S4S34

Table S5S34

Table S6S35

Table S7S35

Table S8S35

References.....S36

Methods

Material Syntheses. The $\text{Co}_{1-x}\text{Fe}_x\text{O}_y$ series with nominally $x = 0.00$ (0.01 from ICP-OES), 0.20, 0.30, 0.40, 0.50, and 0.70 were flame-spray synthesized.^{1,2} The stoichiometric amounts of cobalt nitrate hexahydrate ($\text{Co}(\text{NO}_3)_2 \cdot 6\text{H}_2\text{O}$, 99.9%, Sigma-Aldrich, Germany) and iron nitrate nonahydrate ($\text{Fe}(\text{NO}_3)_3 \cdot 9\text{H}_2\text{O}$, $\geq 98\%$, Sigma-Aldrich, Germany) were dissolved in a 3-to-1 volume solvent mixture of ultrapure water (MicroPure UV, Thermo Scientific, Germany) and acetic acid (AcOH , $\geq 99.0\%$, Roth, Switzerland) to finally have a total metal concentration of 0.1 M. This precursor solution mixture was pumped with a speed of $20 \text{ mL} \cdot \text{min}^{-1}$ into the spraying nozzle with a three piston pump (C-610, Büchi, Switzerland). The continuous precursor solution liquid stream was dispersed into small droplets with an oxygen (99.5%, PanGas, Switzerland) gas flow rate of $35 \text{ L} \cdot \text{min}^{-1}$ shortly before entering the flame. The combustion gas for igniting the flame was a mixture of acetylene (99.6%, PanGas, Switzerland) and oxygen (99.5%, PanGas, Switzerland) with flow rates of 13 and $17 \text{ L} \cdot \text{min}^{-1}$, respectively. The dispersion and combustion gas flow rates were set with mass flow controllers (Bronkhorst, Netherlands). The synthesized nanoparticles were collected on four ashless filter papers (Whatman®, GE Healthcare, United Kingdom) with two vacuum pumps (VACFOX VC 50, Rietschle Thomas, Germany). 0.5 L of precursor solution was sufficient to collect $\sim 1 \text{ g}$ of the so-called as-synthesized powder per electrocatalyst synthesis.

The standard reference material β -cobalt oxyhydroxide (CoOOH) was synthesized following the procedure described in the literature.^{3,4} 80 mL of a 0.05 M cobalt nitrate hexahydrate solution ($\text{Co}(\text{NO}_3)_2 \cdot 6\text{H}_2\text{O}$, $\geq 98\%$ ACS reagent, Sigma-Aldrich, Germany mixed in ultrapure water ($18.2 \text{ M}\Omega \cdot \text{cm}$ (Type I+/I), PURELAB Chorus 1, Elga Veolia, United Kingdom)) was heated up to 50°C in a triple-neck round-bottom flask. Afterwards, 50 mL of a 0.1 M sodium hydroxide solution (NaOH , 99.99% semiconductor grade, Sigma-Aldrich, Germany and ultrapure water) was added dropwise, so that the initial clear pink solution formed pink precipitates out of cobalt hydroxide ($\text{Co}(\text{OH})_2$). The $\text{Co}(\text{OH})_2$ precipitates were centrifuged and washed three times with ultrapure water. The washed precipitates were then dispersed in 40 mL ultrapure water and heated up to 45°C under stirring in a triple-neck reflux cooled round-bottom flask. Afterwards, 10 mL of an 8 M NaOH solution was added dropwise followed by the addition of 4 mL of a commercial hydrogen peroxide solution (H_2O_2 , 35%, Sigma-Aldrich, Germany). The suspension was then stirred for 12 h overnight at 45°C , which finally resulted in brown precipitates of CoOOH . The precipitates were centrifuged and washed three times with ultrapure water and dried at 80°C for 2 days. The successful synthesis was confirmed with powder X-ray diffraction (Figure S23a).

Physicochemical Characterization of As-Synthesized Materials. The final metal ratio in all as-synthesized electrocatalysts from the $\text{Co}_{1-x}\text{Fe}_x\text{O}_y$ series was determined with inductively coupled plasma optical emission spectroscopy (ICP-OES, 5110, Agilent, USA) using axial viewing mode. Approximately $50 \text{ mg}_{\text{cat}}$ of the as-synthesized powder was mixed with 1 mL of nitric acid (HNO_3 , 65% AnalaR NORMAPUR, VWR Chemicals, Germany) and 3 mL of hydrochloric acid (HCl , 37% fuming EMSURE® ACS ISO Reag. Ph Eur for analysis, Supelco Merck, Germany). This suspension was several times shaken with a vortex mixer and heated up in a water bath until a clear solution was obtained. After that, this solution was cooled down and ultrapure water ($18.2 \text{ M}\Omega \cdot \text{cm}$ (Type I+/I), PURELAB Chorus 1, Elga Veolia, United Kingdom) was added to have a final volume of 15 mL. 0.2 M HNO_3 was then added for dilution to reach a final metal concentration in the range between 1 and 10 ppm. To assign the Co and Fe concentration, standard solution of 1, 2, and 10 ppm were prepared by diluting commercial standard solutions (CertiPrep PLCO2-3Y Assurance® Grade Cobalt and CertiPrep PLFE2-3Y Assurance® Grade Iron for AA and ICP in 5% HNO_3 , Spex, USA) with ultrapure water. The total mass and mole fraction of oxygen were determined based on the remaining mass, which was not assigned to cobalt and iron. The Co and Fe signal of the used electrolyte (0.1 M KOH) was determined by diluting it by a factor of 10 with the blank solution (0.2 M HNO_3). The measured Co and Fe concentrations of this diluted solution were similar as for the blank itself as determined by using standard solution of 0.2, 1, 2, and 5 ppm. Therefore, the Co and Fe concentrations were below the detection limit (DL), which was determined for each element by using the following equation: $\text{DL (ppm)} = (3\sigma) \cdot (C_1 - C_0) / (I_1 - I_0)$ with σ as standard deviation of 10 blank measurements (intensity), C_1 as concentration of lowest standard (0.2 ppm), C_0 as concentration of blank (0 ppm), I_1 as intensity of lowest standard and I_0 as intensity of blank. The peak at 230.786 nm was used to determine the Co concentration and at 259.940 nm for Fe in all measurements. The calibration fits was quadratic and was forced to go through the blank intensity (0 ppm).

The crystalline structures of the as-synthesized powders were analyzed on Si-zero-background holders with powder X-ray diffraction (XRD, SmartLab, Rigaku, Japan) in Bragg-Brentano mode using a $\text{K}\beta$ -filtered rotating copper anode at 40 kV and 160 mA. No $\text{K}\alpha_2$ filter was used so that a slight peak splitting is observable in all XRD patterns at higher 2θ angles. The pattern of the following ICSD collection codes were plotted as references: 136039 (fcc-Co),⁵ 9865 (rs-CoO),⁶ 266257 (rs- $\text{Co}_{0.7}\text{Fe}_{0.3}\text{O}$),⁷ 33181 (sp- CoFe_2O_4),⁸ 98551 (sp- FeCo_2O_4),⁹ and 36256 (sp- Co_3O_4).¹⁰

The transmission electron microscopy (TEM) images, the annular dark-field scanning TEM (ADF-STEM) images and the energy-dispersive X-ray spectroscopy (EDX) maps were recorded for $\text{Co}_{0.60}\text{Fe}_{0.40}\text{O}_y$ with a cold field emission gun (FEG) at 200 kV as electron beam source (JEM-ARM200F NEOARM, JEOL, Japan). The EDX maps were recorded by

two SDD detectors covering 1.7 sr. The sample preparation included two steps. First, the TEM grid (continuous ultrathin carbon film coated lacey carbon (400 mesh) supported copper grid, Sigma-Aldrich, Germany) was dipped with the carbon side into the as-synthesized $\text{Co}_{0.60}\text{Fe}_{0.40}\text{O}_y$ powder followed by a carbon-sputtering step (MED010, BalTec, Switzerland) on the $\text{Co}_{0.60}\text{Fe}_{0.40}\text{O}_y$ powder covered grid side to increase the stability of the nanoparticles under the electron beam. The N_2 adsorption isotherms (Autosorb-1, Quantachrome Instruments, USA) were analyzed with the Brunauer-Emmett-Teller (BET) equation to determine the specific surface area (SSA) for all as-synthesized electrocatalysts of the $\text{Co}_{1-x}\text{Fe}_x\text{O}_y$ series. The weighed-in mass of the powder before the outgassing step was used for the gravimetric normalization. The outgassing was performed at 85 °C for 1.5 h. The measurements were repeated three times for all the electrocatalysts, except for $\text{Co}_{0.70}\text{Fe}_{0.30}\text{O}_y$ and $\text{Co}_{0.50}\text{Fe}_{0.50}\text{O}_y$, which were measured only once. The average particle size d in nm was calculated with the help of the following equation:¹¹ $d = 6000 / (\text{SSA}_{\text{BET}} \cdot \rho)$, where SSA_{BET} is in $\text{m}^2 \cdot \text{g}^{-1}$ and ρ is the estimated density in $\text{g} \cdot \text{cm}^{-3}$. The estimated density was linearly interpolated for the different materials using the density of $6.44 \text{ g} \cdot \text{cm}^{-3}$ for rs-CoO ($x = 0$) and of $5.17 \text{ g} \cdot \text{cm}^{-3}$ for sp- Fe_3O_4 ($x = 1$).¹² The surface area-to-bulk volume ratio can be calculated by $(4 \cdot \pi \cdot r^2) / (4/3 \cdot \pi \cdot r^3) = 3 / r = 6 / d$. Therefore, the ratio of the surface area-to-bulk volume ratio can be calculated by $(6 / d_1) / (6 / d_2) = d_2 / d_1$. Spherical particle shapes were assumed in these calculations.

The X-ray absorption spectroscopy (XAS) experiments at the Co K-edge (7709 eV) and Fe K-edge (7112 eV) using hard X-rays were undertaken at the SuperXAS beamline of the Swiss Light Source (SLS, PSI, Switzerland). This beamline is capable to measure in quick extended X-ray absorption fine structure (QEXAFS) mode, which allows the acquisition of 120 spectra per min.¹³ For these measurements, the polychromatic photon beam at the beamline, produced by a 2.9 T superbend magnet source, got collimated with a Si-coated mirror at 2.9 mrad, monochromatized with a liquid N_2 cooled channel-cut Si(111) crystal oscillating with a 1 Hz frequency, and focused on a spot size of 0.2 mm x 1 mm with a Rh-coated toroidal mirror. All Co and Fe K-edge XAS spectra were recorded in transmission mode using three 15 cm long ionization chambers filled with 1 bar of N_2 . The sample position was always between the first and second ionization chamber, while the reference foil for energy calibration was placed between the second and third ionization chamber. A Co or Fe metal foil (99.9%, GoodFellow, United Kingdom) was used as the reference to calibrate the sample spectra at the Co and Fe K-edge, respectively, by assigning the first peak of the first derivative of the reference foil spectra to the appropriate absorption energy (Figure S23b). The energy calibrated spectra were then normalized and averaged with the ProQEXAFS software.¹⁴ The samples were glucose-diluted pellets (D-(+)-Glucose, $\geq 99.5\%$ GC, Sigma-Aldrich, Germany) of the as-synthesized powder from the $\text{Co}_{1-x}\text{Fe}_x\text{O}_y$ series or out of standard reference material powder. The pellets had a diameter of 1.3 cm and a total mass of approximately 100 mg with a mass ratio of approximately 1-to-9 between the sample powder and glucose. The pellets were finally wrapped in a Kapton[®] tape. The standard reference materials were composed either out of self-made β -cobalt(III) oxyhydroxide (CoOOH) or out of as-purchased cobalt(II) oxide (CoO , $\geq 99.99\%$, Sigma-Aldrich, Germany), cobalt(II) iron(III) oxide (CoFe_2O_4 , 98%, abcr, Switzerland), cobalt(II,III) oxide (Co_3O_4 , 99.9985% Puratronic[®], Thermoscientific - Alfa Aesar, Germany), iron(II) oxide (FeO , 99.7%, Sigma-Aldrich, Germany), iron(II,III) oxide (Fe_3O_4 , 99.999%, Sigma-Aldrich, Germany), and α -iron(III) oxide (Fe_2O_3 , $\geq 99.995\%$, Sigma-Aldrich, Germany). The measurement time for all pellets was 2 min (240 spectra). The Co oxidation state was determined by a linear interpolation between the two standard measurements of CoO and Co_3O_4 for the energy of half-normalized edge step from the X-ray absorption near-edge spectroscopy (XANES) measurements. The FT-EXAFS spectra were fitted over a k -range of 3 to 11.5 \AA^{-1} for the Co K-edge and over a range of 3 to 11.3 \AA^{-1} for the Fe K-edge with a k^3 -weighting using Artemis from the Demeter software package.¹⁵ The model for the best fits were computed from CIF-files out of the ICSD database with the collection code 136039 (fcc-Co),⁵ 9865 (rs-CoO),⁶ 33181 (sp-Co Fe_2O_4),⁸ 624573 (sp-Co Co_3O_4),¹⁶ 22285 (β -CoOOH),¹⁷ 631736 (Fe),¹⁸ and 633038 (FeO).¹⁹ The CIF-file of CoFe_2O_4 was modified before being used in a fit so that the A- and B-sites can be independently fitted for both edges. In the original file does Co occupy 21% of the A-sites (Fe 79%) and 39% of the B-sites (Fe 61%) lattice positions resulting in a chemical formula of $\text{Co}_{0.21}\text{Fe}_{0.79}(\text{Co}_{0.39}\text{Fe}_{0.61})_2\text{O}_4$, which is typical for such a material. Thus, the CIF-file was modified to have finally two different versions. In the first version called CoFe_2O_4 did Co occupy only the A-sites and Fe only the B-site, and in the second version called FeCo_2O_4 did Co occupy only the B-sites and Fe only the A-sites. To be able to fit the coordination number of the different structure models, an amplitude reduction factor S_0^2 must be assumed. This S_0^2 value was determined for each sample by fitting the first coordination shell of the corresponding reference foil, while keeping the coordination number fixed at the theoretical value. Only the first scattering path was needed to fit the first shell of the Co reference foil FT-EXAFS, while the first two scattering path were needed to fit the first shell of the Fe reference foil FT-EXAFS. To determine the relative ratio of different phases in the as-synthesized powder FT-EXAFS, a so-called phase composition fraction p_{fit} parameter was fitted, while keeping the coordination number ratio for a given model structure constant as defined by the theoretical value. Thus, the fitted coordination number N_{fit} is the product of the theoretical coordination number N_{th} and the fitted phase composition fraction p_{fit} . The magnitude of the k^3 -weighted FT-EXAFS is shown in all cases without phase correction as indicated with the x-axis label of $R + \Delta R$.

The Co (778 eV) and Fe (707 eV) L₃-edge XAS spectra were measured using soft X-rays at the X-Treme²⁰ and PHOENIX beamlines at SLS, PSI. All Co and Fe L₃-edge XAS spectra were recorded in total-electron-yield (TEY) mode, at room temperature, in ultra-high-vacuum at X-Treme (10⁻¹¹ mbar) and in high vacuum at PHOENIX (10⁻⁵ mbar). The scan rate was 80 eV per 3 min (26.67 eV·min⁻¹) and the energy step size was approximately 0.025 eV. Each shown spectrum is an average of three measurements. A relative energy calibration was performed to align the spectra measured during different beamtimes and beamlines. The position of the α , β , γ , and δ peaks of a Co²⁺ containing material was used to align the Co L₃-edge spectra and the position of the β and γ peaks of the standard material Fe₂O₃ was used to align the Fe L₃-edge spectra. The samples were either as-synthesized or as-purchased standard material powder, which were pressed on carbon tape and then mounted on a copper sample holder. The standard materials were the same as used for the Co and Fe K-edge XAS experiments and thus, either as-synthesized (CoOOH) or as-purchased (CoO,²¹⁻²⁵ Co₃O₄,^{23,26,27} FeO,^{22,28} Fe₃O₄,^{22,29} CoFe₂O₄³⁰⁻³² (only for Fe), and Fe₂O₃^{22,28,29}) standard powders. The spectrum of the as-purchased CoO and FeO standard material showed the presence of an oxidized layer at the surface. Two argon-ion sputtering steps were needed to remove this superficial oxidized passivation layer. The first sputtering was performed for 1 h with an argon-ion energy of 1 keV and a sputter current of $I_{sp} = 2.2 \mu\text{A}$. This sputtered sample was then exposed to air for 1 min before the Co and Fe L₃-edge TEY-XAS measurement, since the sputtering was not performed inside the preparation chamber of the beamline. The second sputtering step was performed on the same sample for 10 min with an argon-ion energy of 1 keV and a sample current of $I_{sp} = 12 \mu\text{A}$ inside the preparation chamber of the X-Treme beamline. Thus, the sample was measured directly after the second sputtering step without being exposed to any oxidizing agent in the meanwhile. All spectra were divided by the I_0 signal of an Au grid, which was positioned between the sample and the X-ray source. These I_0 corrected data was then baseline corrected and normalized. The Co L₃-edge spectra were normalized by dividing the averaged maximum β and δ peak intensity. The Fe L₃-edge spectra were normalized by dividing the averaged maximum β and γ peak intensity. The surface Co oxidation state for as-purchased CoO, 1x Ar-ion sputtered CoO and as-synthesized Co_{1-x}Fe_xO_y series between +2 and +2.67 was estimated by linearly interpolating the normalized maximum δ peak intensity ($I_{\text{norm,max},\delta}$) between the Co²⁺ (2x Ar-ion sputtered CoO) and Co^{2.67+} (Co₃O₄) standard spectra. The surface oxidation states between +2.67 and +3 were estimated by linearly interpolating $I_{\text{norm,max},\delta}$ between the Co^{2.67+} (Co₃O₄) and Co³⁺ (CoOOH) standard spectra. The mole fraction weighted average surface metal oxidation state was calculated by the sum of the molar fraction weighted individual surface oxidation states (sOS) with $(1-x) \cdot \text{sOS}_{\text{Co}} + x \cdot 3$ and assuming $\text{sOS}_{\text{Fe}} = 3$ for all materials. The fraction of surface Co, which is +2 and octahedrally (O_h) coordinated by oxygen atoms (B in AB₂O₄) with a high-spin (hs) state, was determined by using the normalized maximum α peak intensity in the Co L₃-edge, which is proportional to the fraction of the hs Co²⁺-ions in O_h-sites. Other fractions such as low-spin (ls) Co²⁺ in O_h-sites,^{33,34} Co²⁺ which is tetrahedrally (T_d) coordinated by oxygen atoms (e.g. wurtzite-like-CoO and Co₃O₄)^{21,23,27,35,36} or Co³⁺ in O_h- (e.g. Co₃O₄ and CoOOH)^{23,24,27} or T_d-sites³⁵ have no significant α peak intensity. Therefore, the Co²⁺ in O_h-sites fraction for the Co_{1-x}Fe_xO_y series were determined by linearly interpolating the normalized maximum α peak intensity of the standard CoO (sp. 2x) L₃-edge spectra, which was assumed to have a hs Co²⁺ in O_h-sites fraction of 100%, and of the standard CoOOH L₃-edge spectra, which was assumed to have a hs Co²⁺ in O_h-sites fraction of 0%. The Co²⁺ in T_d-sites fraction was calculated by $3 - \text{sOS}_{\text{Co}} - \text{Co}^{2+} \text{ in O}_h\text{-sites fraction}$, which requires the reasonable assumption for spinel's that Co²⁺ can only occupy O_h- or T_d-sites. The Co³⁺ fraction was calculated by $\text{sOS}_{\text{Co}} - 2$. The literature values from XRD refinements for the fractions of Co₃O₄ were determined by assuming that no Co²⁺ will occupy O_h-sites, whereas for FeCo₂O₄ and CoFe₂O₄ a Fe oxidation state of 3+ was assumed. A 10% systematic error for the surface Co oxidation state and Co²⁺ sites fraction assignment is assumed.

Electrochemical Characterization. A three-electrode setup equipped with a rotating disk electrode (RDE), an impedance spectroscopy (IS) capable multichannel potentiostat (VMP-300, BioLogic Science Instruments, France), a modulated speed rotator (MSR, Pine Research Instrumentation, USA) and a homemade cell out of a halved Nalgene fluorinated ethylene propylene (FEP) bottle (500 mL, Nalge Nunc International, USA) covered with a Teflon cap was used to determine the electrocatalytic activity for OER of the as-synthesized Co_{1-x}Fe_xO_y series.³⁷ Synthetic air (syn air, 5.6 purity, PanGas AG, Switzerland) saturated daily freshly prepared 0.1 M potassium hydroxide solution (KOH, 99.99%, Sigma Aldrich, Germany and ultrapure water (18.2 M Ω ·cm (Type I+I), PURELAB Chorus 1, Elga Veolia, United Kingdom)) was used as electrolyte and filling solution for the mercury/mercury oxide (Hg/HgO, RE-61AP, ALS, Japan) reference electrode (RE) in each RDE measurement. The potentials in all RDE studies are given with respect to the reversible hydrogen electrode (RHE) scale indicated with the unit V_{RHE} . Thus, the RE was calibrated against a polycrystalline platinum disk insert (Pt_{pe}, 5.0 mm OD (0.196 cm²), Pine Research Instrumentation, USA) in the hydrogen (5.0, PanGas, Switzerland) saturated electrolyte^{2,38-40} (Figure S23c). All RDE studies were performed with a RDE speed rate of 900 rpm, at room temperature and with a freshly flame-annealed gold mesh (Gold WOVEN Mesh/Gauze, Advent Research Materials Ltd, United Kingdom) as counter electrode (CE). 2 x 5 μL of an electrocatalyst containing ink suspension with a

concentration of $2.0 \text{ g}_{\text{cat}} \cdot \text{L}_{\text{ink}}^{-1}$ was drop casted on freshly polished ($0.3 \mu\text{m}$ and $0.05 \mu\text{m}$ MicroPolish alumina solution used on different MicroCloths, Buehler, USA) glassy carbon disk insert (GC, SIGRADUR G, 5.0 mm OD (0.2 cm^2), HTW GmbH, Germany) to prepare the working electrode (WE). Approximately $5 \text{ mg}_{\text{cat}}$ of the investigated as-synthesized electrocatalyst from the $\text{Co}_{1-x}\text{Fe}_x\text{O}_y$ series was ultrasonically (Ultrasonic Cleaner, VWR, USA) mixed for 30 min in a solution mixture of 2 mL 2-Propanol (IPA, 99.9% (HPLC Plus), Sigma Aldrich, Germany), 0.5 mL ultrapure water and $10 \mu\text{L}$ of Na^+ -exchanged Nafion (NaOH , 99.99% and Nafion® perfluorinated resin solution, 5 wt.% in lower aliphatic alcohols and water, contains 15-20% water, Sigma Aldrich, Germany) to prepare the ink.⁴¹ After the drop casting, the WEs were dried in the air with a final loading of $0.1 \text{ mg}_{\text{cat}} \cdot \text{cm}_{\text{geom}}^{-2}$.

Two different electrochemical protocols were used to determine the OER activity and stability of the $\text{Co}_{1-x}\text{Fe}_x\text{O}_y$ series. The OER activity protocol included 25 cyclic voltammograms (CV) between 1.0 and $1.7 \text{ V}_{\text{RHE}}$ measured with a scan rate of $10 \text{ mV} \cdot \text{s}^{-1}$, followed by 15 chronoamperometric (CA) measurements between 1.3 and $1.7 \text{ V}_{\text{RHE}}$ while holding each potential for 30 s. Three IS measurements with an amplitude of 10 mV at $1.2 \text{ V}_{\text{RHE}}$ and a frequency range of 1 MHz to 1 Hz, before the CV and after the CA steps, and at $1.4 \text{ V}_{\text{RHE}}$ at the end of the protocol were performed to correct for the ohmic drop. Finally, the mass-normalized averaged steady-state current (J) in the linear range of three independent CA measurements were then plotted against the IR-free potential ($E_{\text{IR-free}}$) in the Tafel plot, except for $\text{Co}_{0.70}\text{Fe}_{0.30}\text{O}_y$ and $\text{Co}_{0.50}\text{Fe}_{0.50}\text{O}_y$, which were measured only once. The OER stability behavior of the electrocatalysts were investigated with potentiostatic stability measurements. The protocol started with a IS measurement at $1.2 \text{ V}_{\text{RHE}}$ using an amplitude of 10 mV and a frequency range of 1 MHz to 1 Hz, and two CV cycles between 1.0 and $1.6 \text{ V}_{\text{RHE}}$ with a scan rate of $50 \text{ mV} \cdot \text{s}^{-1}$. After that, CA experiments at 1.0 (lower potential value) and $1.6 \text{ V}_{\text{RHE}}$ (upper potential value) were performed by staying at each potential for 10 s. These two CA experiments were repeated 505 times and were interrupted five times after each 101th cycle by three CV cycles in the same potential range with a scan rate of $50 \text{ mV} \cdot \text{s}^{-1}$. The protocol ended with the same IS measurement as at the beginning. Finally, the mass-normalized averaged steady-state current at $1.6 \text{ V}_{\text{RHE}}$ ($J@1.6 \text{ V}_{\text{RHE}}$) for each potential CA cycle of four independent measurements were then plotted against the cycling number, except for $\text{Co}_{0.50}\text{Fe}_{0.50}\text{O}_y$, which was measured only once. The absolute current density change in $\text{A} \cdot \text{g}_{\text{cat}}^{-1}$ ($\Delta J@1.6 \text{ V}_{\text{RHE}}$) was achieved by subtracting all data points with the current density of the first cycle. The relative current density change in % ($\Delta J@1.6 \text{ V}_{\text{RHE}}$) was achieved by dividing all data points with the current density of the first cycle. To investigate the influence of the O_2 bubble formation at the WE during the stability protocol, so-called differential potentiostatic measurements were performed. This type of protocol is a combination of galvanostatic and potentiostatic measurements. In the original potentiostatic stability measurement is the lower ($1.0 \text{ V}_{\text{RHE}}$) and upper ($1.6 \text{ V}_{\text{RHE}}$) potential value in the CA measurements constant for all electrocatalysts. In contrast, the differential potentiostatic stability measurements can have a different upper potential value for each of the electrocatalysts. However, the difference in the lower and upper potential value remains constant in all cycles also in this new protocol. The goal of a differential potentiostatic stability measurements is, that the initial current density, and with that the initial O_2 bubbles formation, should be for all electrocatalysts more or less identical. Thus, the initially more OER active electrocatalysts such as $\text{Co}_{0.80}\text{Fe}_{0.20}\text{O}_y$, $\text{Co}_{0.60}\text{Fe}_{0.40}\text{O}_y$ and $\text{Co}_{0.50}\text{Fe}_{0.50}\text{O}_y$ had a higher potential value of $1.6 \text{ V}_{\text{RHE}}$ (thus, there is no difference in the two protocols for these materials), while the initially less OER active electrocatalysts such as $\text{Co}_{0.99}(\text{Fe}_{0.01})\text{O}_y$ and $\text{Co}_{0.30}\text{Fe}_{0.70}\text{O}_y$ had a upper potential value of $1.608 \text{ V}_{\text{RHE}}$ during all potential cycles. These differential potentiostatic stability measurements for $\text{Co}_{0.99}(\text{Fe}_{0.01})\text{O}_y$ and $\text{Co}_{0.30}\text{Fe}_{0.70}\text{O}_y$ were only performed one times.

To estimate the Co-mass normalized cumulated net charge (Q_{net}) from pseudocapacitive processes, the 1st and 25th CV cycle of $\text{Co}_{0.99}(\text{Fe}_{0.01})\text{O}_y$, $\text{Co}_{0.80}\text{Fe}_{0.20}\text{O}_y$, $\text{Co}_{0.60}\text{Fe}_{0.40}\text{O}_y$ and $\text{Co}_{0.30}\text{Fe}_{0.70}\text{O}_y$ was shifted on the y-axis ($J + \Delta J$) so that at $1.05 \text{ V}_{\text{RHE}}$ the modulus of the current densities for the positive and negative going potential scan (afterwards) are equal. The value of $1.05 \text{ V}_{\text{RHE}}$ was selected because only double-layer capacitive processes are expected at this potential value for all four materials and that the current density at this potential value is marginally affected by imperfections in the ohmic drop correction. Then, the current densities for the positive (J_+) and negative going potential scan afterwards (J_-) were individually interpolated to reach two vectors with the same x-values (potential scale). After that, the net current density (J_{net}) for these common x-values between 1.05 and $1.5 \text{ V}_{\text{RHE}}$ was calculated by $J_{\text{net}} = J_+ - |J_-|$. Therefore, J_{net} has ideally only contributions from pseudocapacitive processes as the double-layer capacitive processes contribute in the same extent to J_+ and $|J_-|$, which is cancelled out in J_{net} . Then, J_{net} was divided by the scan rate of $10 \text{ mV} \cdot \text{s}^{-1}$ and integrated over the potential range between 1.05 and $1.5 \text{ V}_{\text{RHE}}$ to calculate the Co-mass normalized cumulated net charge (Q_{net}). The non-capacitive faradaic current density for OER was not subtracted in this analysis so that the J_{net} and Q_{net} values above $\sim 1.45 \text{ V}_{\text{RHE}}$ has to be considered with caution.

Operando / Ex Situ XAS and Ex Situ XRD. The sample for the operando Co and Fe K-edge XAS experiments was an as-prepared electrode out of $\text{Co}_{0.60}\text{Fe}_{0.40}\text{O}_y$. This as-prepared electrode was composed out of a conductive carbon coated Kapton® foil (Kapton® 200RS100, DuPont, USA), where a small part in the middle with a geometrical area of

0.126 cm²_{geom} was sprayed-coated with an Co_{0.60}Fe_{0.40}O_y containing ink suspension using an airbrush-pistol (Sogolee HP-200 Double Action with a 0.2 mm nozzle diameter, Taiwan Airbrushes & Equipments, Taiwan). To further improve the conductivity of the carbon coated Kapton[®] foil, an approximately 100 nm thick Au layer was sputtered around the area of the electrocatalyst prior to the spray-coating preparation step.⁴² The Co_{0.60}Fe_{0.40}O_y containing ink suspension, used for the spray-coating step, was a 22.5-to-1 volume mixture of ultrapure water and Na⁺-exchanged Nafion (NaOH, 99.99% semiconductor grade and Nafion[®] perfluorinated resin solution, 5 wt.% in lower aliphatic alcohols and water, contains 15-20% water, Sigma Aldrich, Germany)⁴¹ with a Co_{0.60}Fe_{0.40}O_y concentration of 68 mg_{cat}·mL⁻¹_{ink}. The final mass on the electrode was approximately 0.36 mg_{cat} (2.9 mg_{cat}·cm⁻²_{geom}) quantified with a microbalance (XPE206DR, Mettler Toledo, Switzerland).⁴³ The operando Co and Fe K-edge XAS experiments were performed in an in-house developed PEEK flow cell.⁴² A 0.1 M potassium hydroxide solution (KOH, 99.99%, Sigma Aldrich, Germany and ultrapure water (18.2 MΩ·cm (Type I+/I), PURELAB Chorus 1, Elga Veolia, United Kingdom)), black pearl (2000 carbon black, Cabot Corporation, USA) spray-coated (Au-sputtered and carbon coated) Kapton[®] foil and an Ag/AgCl electrode (low-leakage 3 M NaCl filled, Harvard Apparatus, USA) was used for the electrochemical experiments in the flow cell as electrolyte, as counter (CE) and as reference electrode (RE), respectively. The electrolyte was pumped with a withdraw syringe pump (Legato[®] 210, KD Scientific, USA) with a flow rate of 0.4 mL·min⁻¹ through the flow cell. The CE was prepared with the same method as the sample electrode and was pre-wetted with ultrapure water before use. The RE was calibrated before and after the operando experiment against a 0.1 M KOH filled mercury/mercury oxide RE (Hg/HgO, RE-61AP, ALS, Japan), which in turn was calibrated against a RHE. First, the as-prepared sample electrode was measured in the flow cell, then the electrolyte was pumped into the cell and the open circuit voltage (OCV) spectra was measured. Then the chronoamperometric (CA) measurement was started. The spectra under potential control were recorded always 1 min after reaching an electrochemical steady-state of the new applied potential. Operando spectra were recorded at 1.000, 1.100, 1.200, 1.300, 1.400, 1.450, 1.500, 1.525, and 1.550 V_{RHE} in the so-called positive scan. Afterwards, the potential was again decreased and spectra at 1.200 and 1.000 V_{RHE} were measured in the so-called negative scan. These potentials are not ohmic drop corrected. After that, 10 cyclic voltammograms (CV) between 1.000 and 1.600 V_{RHE} were recorded. Finally, an electrochemical impedance spectroscopy (EIS) was measured at 1.200 V_{RHE} to correct for the high-frequency resistance (HFR), which includes the resistance of the liquid electrolyte layer, but not the resistance in the electrocatalyst layer. The highly conductive Au layer of the sample electrode was as well in contact with the electrolyte, which will close a circuit path with a lower resistance in comparison when the electrocatalysts layer would be included (Figure S23d). The Co and Fe K-edge XAS measurement time for all the electrodes was 1 min (120 spectra) and no edge jump loss was detected during the operando experiment at both edges revealing a stable electrode and a reliable measurement (Figure S23f).⁴⁴ The crystalline structures of the as-prepared and ex situ after the operando XAS measurement (after OER) electrodes of Co_{0.60}Fe_{0.40}O_y were determined by XRD in transmission mode. The bare Au-sputtered electrode was measured to assign the additional peaks in the transmission spectra from crystalline Au (ICSD collection code 52700).⁴⁵ All transmission XRD patterns were background corrected. A typical XRD pattern measured in transmission has a significant decrease in intensity towards higher angles so that most of the peaks vanishes after a 2θ of 50°. Moreover, the noise in the background is decreasing as well towards higher 2θ values.

The samples for the ex situ 'after OER' Co and Fe L₃-edge TEY-XAS experiments were drop-casted electrocatalyst covered glassy carbon (GC) disk inserts and therefore identical with the samples used for the electrochemical characterization in the RDE setup. Briefly, the electrocatalysts containing ink suspension composed out of an ultrapure water, 2-propanol and Na⁺-exchanged Nafion mixture was drop casted on a GC for the 'as-prepared' sample with a final loading of 0.1 mg_{cat}·cm⁻²_{geom}. The 'after OER' GC was prepared in the same way but was then electrochemically treated with the same OER activity protocol in the same RDE setup as previously used to electrochemically characterize the electrocatalysts (refer to the Electrochemical characterization). After the OER activity protocol, the CA part was repeated so that the last applied potential was 1.7 V_{RHE}. Finally, the 'after OER' GC's were dipped into ultrapure water to remove the KOH and was then dried in the air. The 'as-prepared' and 'after OER' GC's were both stored at 0.1 mbar in a desiccator directly after preparation for few days until they were glued onto carbon tape on a copper sample holder, shortly before the sample were loaded into the beamline endstation. The surface oxidation states (Co and metal mole fraction weighted average) as well as the Co²⁺ in O_h-sites, Co²⁺ in T_d-sites and Co³⁺ fractions were determined as described for the as-synthesized materials. The assignment of the different sources for the irreversible surface Co oxidation was done by subtracting the 'as-synthesized' or 'as-prepared' Co²⁺ O_h- and T_d-sites fractions from the corresponding 'after OER' fractions. A 10% systematic error for the surface Co oxidation state and fractions assignment is assumed and the presence of negative values (lower Co²⁺ in O_h-site fraction than CoOOH, which was assumed to be 0%) are within this error range. All Fe L₃-edge TEY-XAS spectra measured with the 'as-prepared' and 'after OER' samples were corrected for the Fe K-edge background corrected originating from Na⁺-exchanged Nafion. This background was determined by measuring a GC electrode, where an electrocatalysts-free ink (only ultrapure water and Na⁺-exchanged Nafion) was drop casted (Figure S23e).

Supporting Information Figures

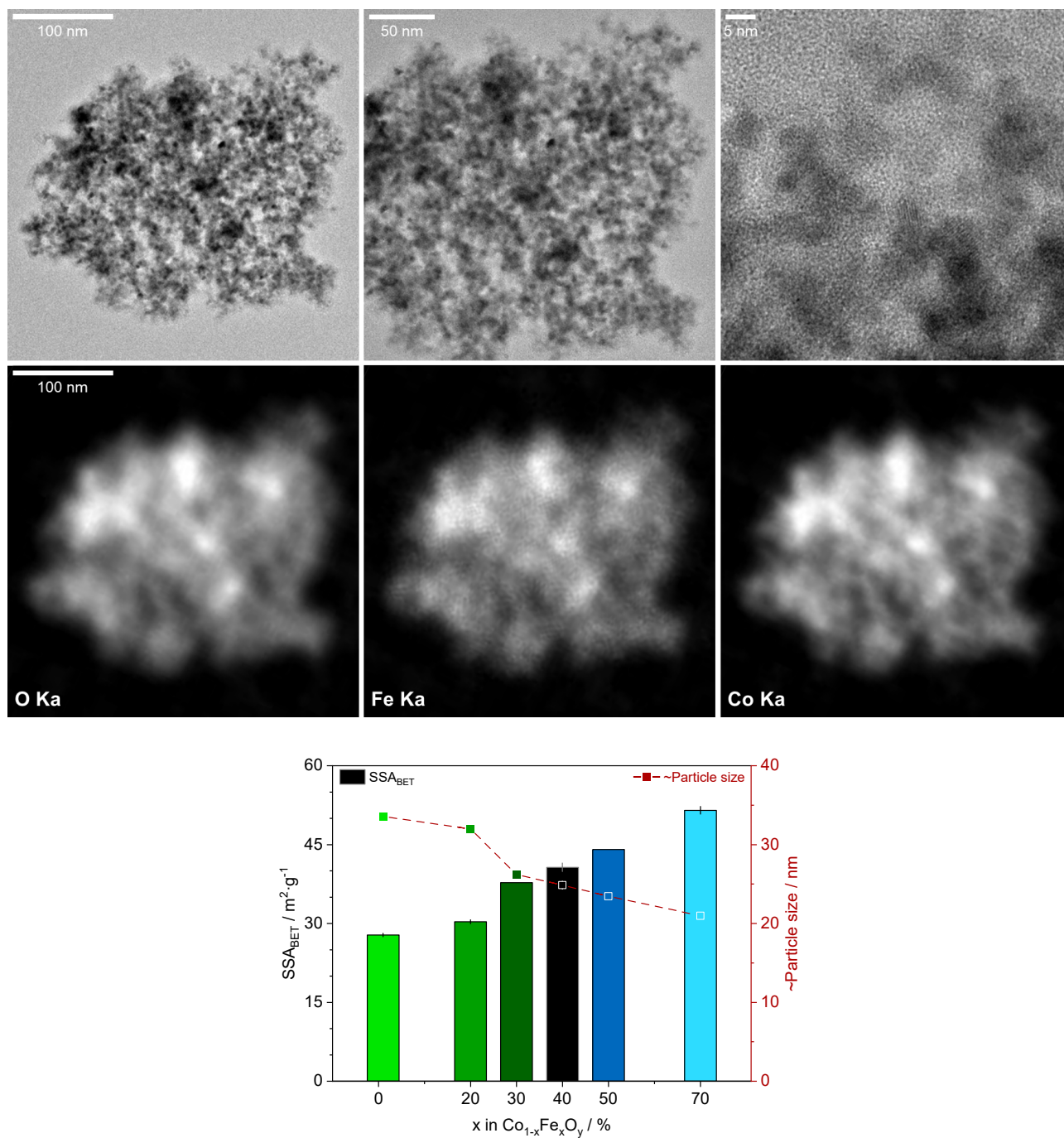


Figure S1. TEM images and EDX maps recorded in ADF-STEM mode of flame-spray synthesized $\text{Co}_{0.60}\text{Fe}_{0.40}\text{O}_y$ and SSA_{BET} of $\text{Co}_{1-x}\text{Fe}_x\text{O}_y$ series. Top row, TEM images of agglomerated nanoparticles recorded with different magnifications representative for the particles at the lower size range between 5 and 30 nm. Middle row, EDX maps from ADF-STEM of the same agglomerated nanoparticles as in the top row revealing a homogeneous distribution of O, Fe, and Co atoms. Bottom row, Specific surface area (SSA_{BET}) using BET methodology (left axis and bar chart) and corresponding (calculated) approximate average particle size (right axis and square dots). The vertical lines indicate the error bar of three independent averaged measurements. The surface area-to-bulk volume ratio increases from $\text{Co}_{0.99}(\text{Fe}_{0.01})\text{O}_y$ to $\text{Co}_{0.30}\text{Fe}_{0.70}\text{O}_y$ by a factor of maximum ~ 1.8 (35 nm / 20 nm).

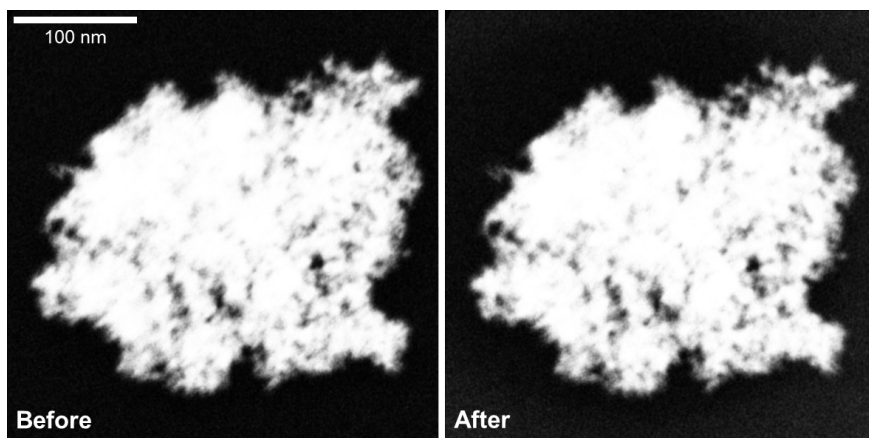


Figure S2. ADF-STEM images of flame-spray synthesized $\text{Co}_{0.60}\text{Fe}_{0.40}\text{O}_y$. The same agglomerated nanoparticles as shown in Figure S1 before and after the EDX mapping revealing the stability of the agglomerated nanoparticles with the used conditions during the recording.

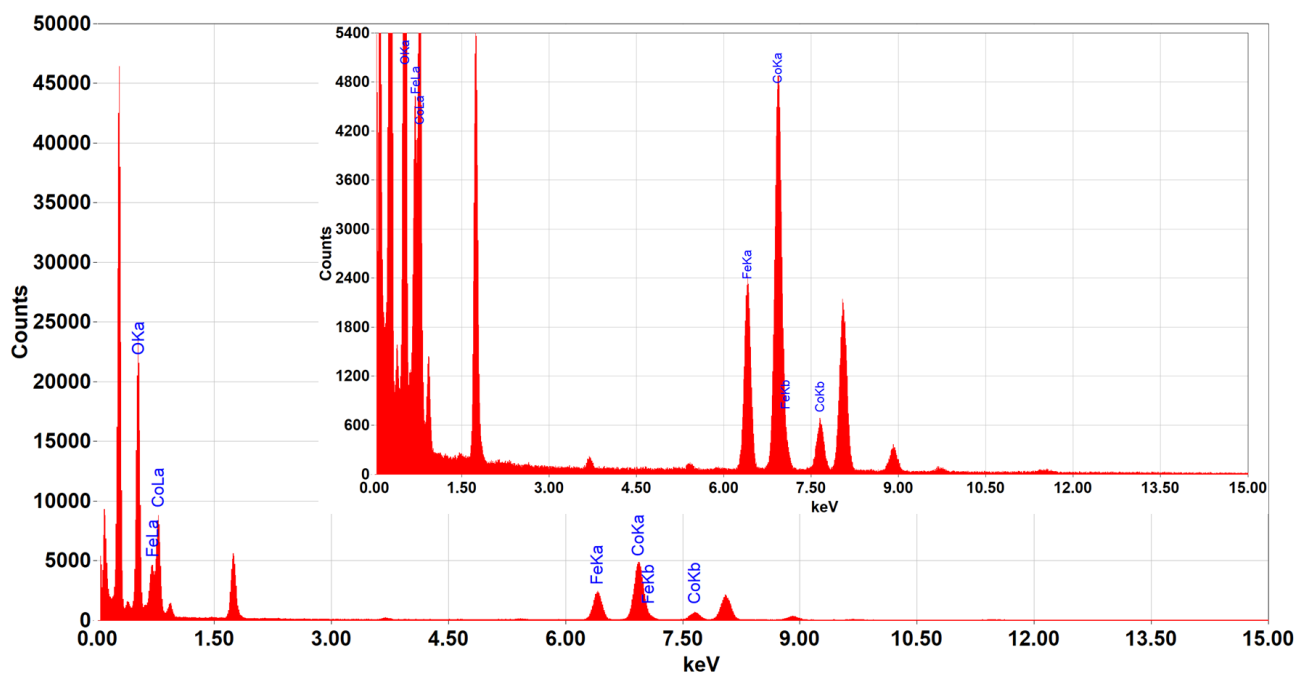


Figure S3. EDX spectrum of flame-spray synthesized $\text{Co}_{0.60}\text{Fe}_{0.40}\text{O}_y$. Integrated EDX spectrum over the whole ADF-STEM scanning range of the EDX map in Figure S1 revealing the presence of other elements beside of the expected O, Fe and Co signal.

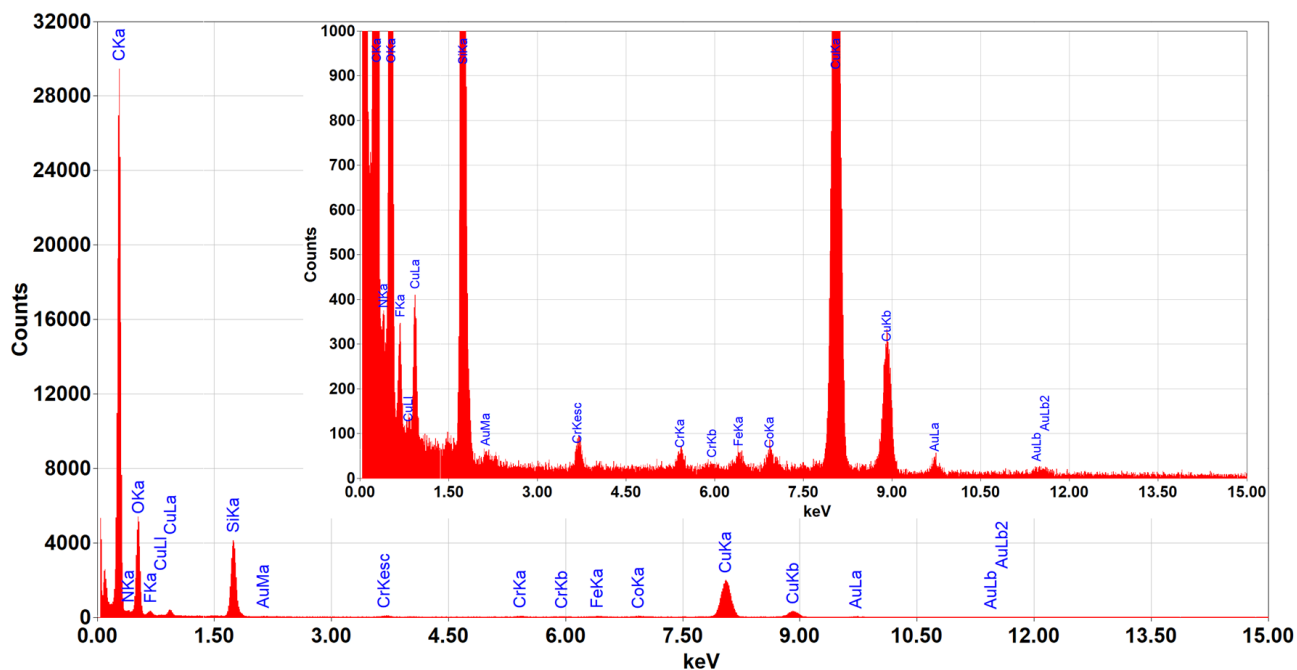


Figure S4. EDX spectrum of the TEM grid background. Integrated EDX spectrum over the whole ADF-STEM scanning range of the background (TEM grid without a sample) revealing that the unassigned peaks in Figure S3 are coming all from the background. C, O, and Cu is coming from the grid. O, F, and Si probably from grease. Au, Cr, and small amounts of Fe and Co from the instrument.

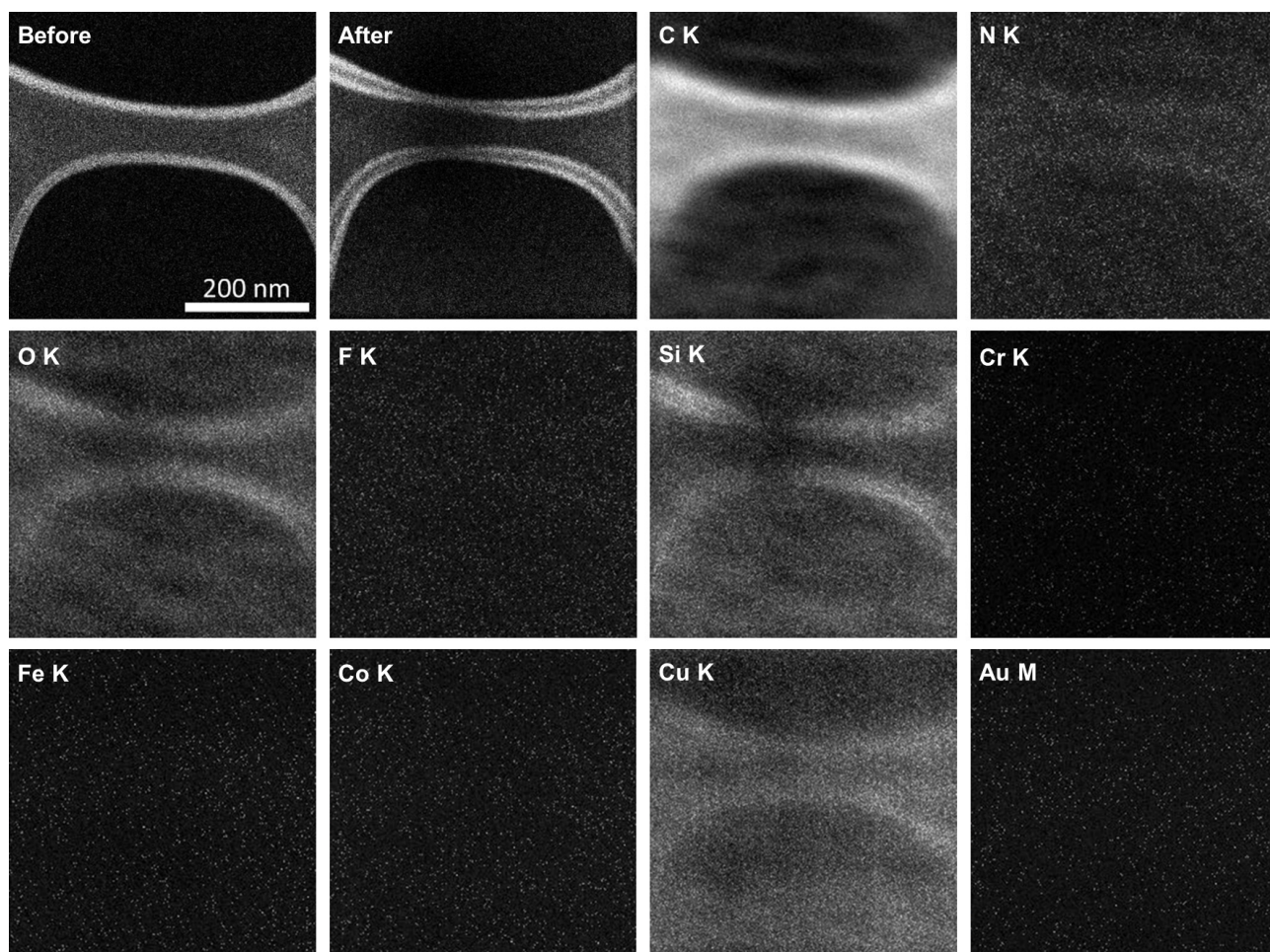


Figure S5. ADF-STEM background images and corresponding EDX maps of the TEM grid background. ADF-STEM images before and after the EDX mapping of the background (TEM grid without a sample) revealing only small carbon accumulation during the map recording in the 'after' image. Corresponding EDX maps of all elements found and shown in the background spectrum in Figure S4.

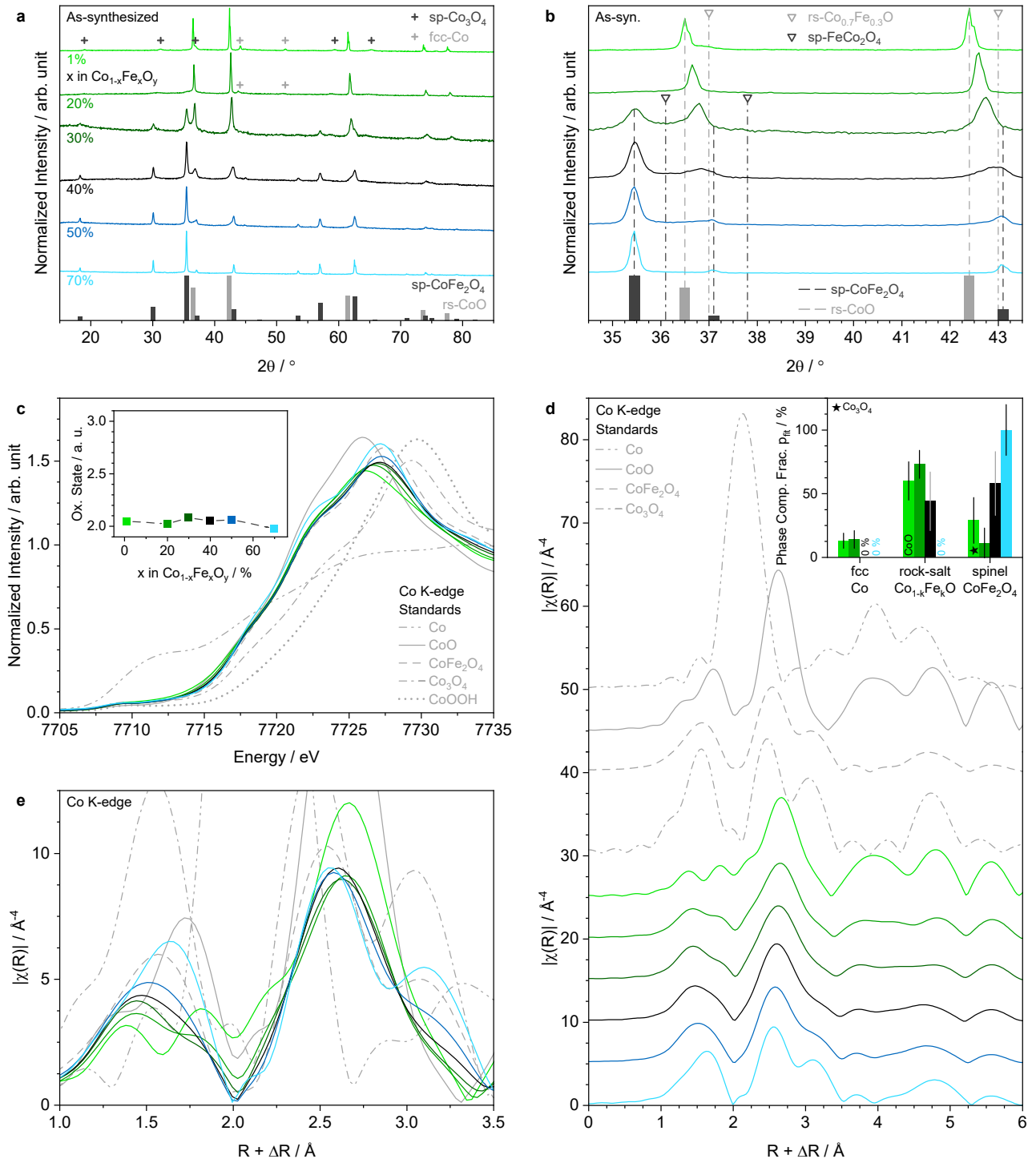


Figure S6. As-synthesized bulk: Co^{2+} but gradual rock-salt (rs) to spinel (sp) structure change within $\text{Co}_{1-x}\text{Fe}_x\text{O}_y$ series. (a) and (b) As-synthesized powder XRD of the $\text{Co}_{1-x}\text{Fe}_x\text{O}_y$ series (x by ICP-OES) measured in Bragg-Brentano mode. The dashed or dash-dotted vertical lines were added for several reference patterns to guide the eyes of the reader. (c) XANES of Co K-edge spectra. Inset (c) Bulk Co oxidation state trend as a function of the Fe-content. (d) Magnitude of k^3 -weighted Fourier transformed- (FT) EXAFS from Co K-edge spectra (k -range from 2.7 to 12 \AA^{-1}). Inset (d) Phase composition fractions (p_{fit}) for as-synthesized materials with $x = 0.01, 0.20, 0.40$, and 0.70 extracted from FT-EXAFS best fits in Figure S8 with fitting errors as vertical lines. (e) Same data as shown in (d) but overlaid and magnified. XANES, FT-EXAFS, and p_{fit} of the corresponding Fe K-edge are in Figure S7. Refer to Methods for ICSD collection code of the reference materials shown in XRD patterns and of the standards used in hard XAS (XANES, FT EXAFS, and fitting process). The best fitting values are listed in the Tables S2-S5. The color code of the $\text{Co}_{1-x}\text{Fe}_x\text{O}_y$ series as defined in (a) is valid in all figures.

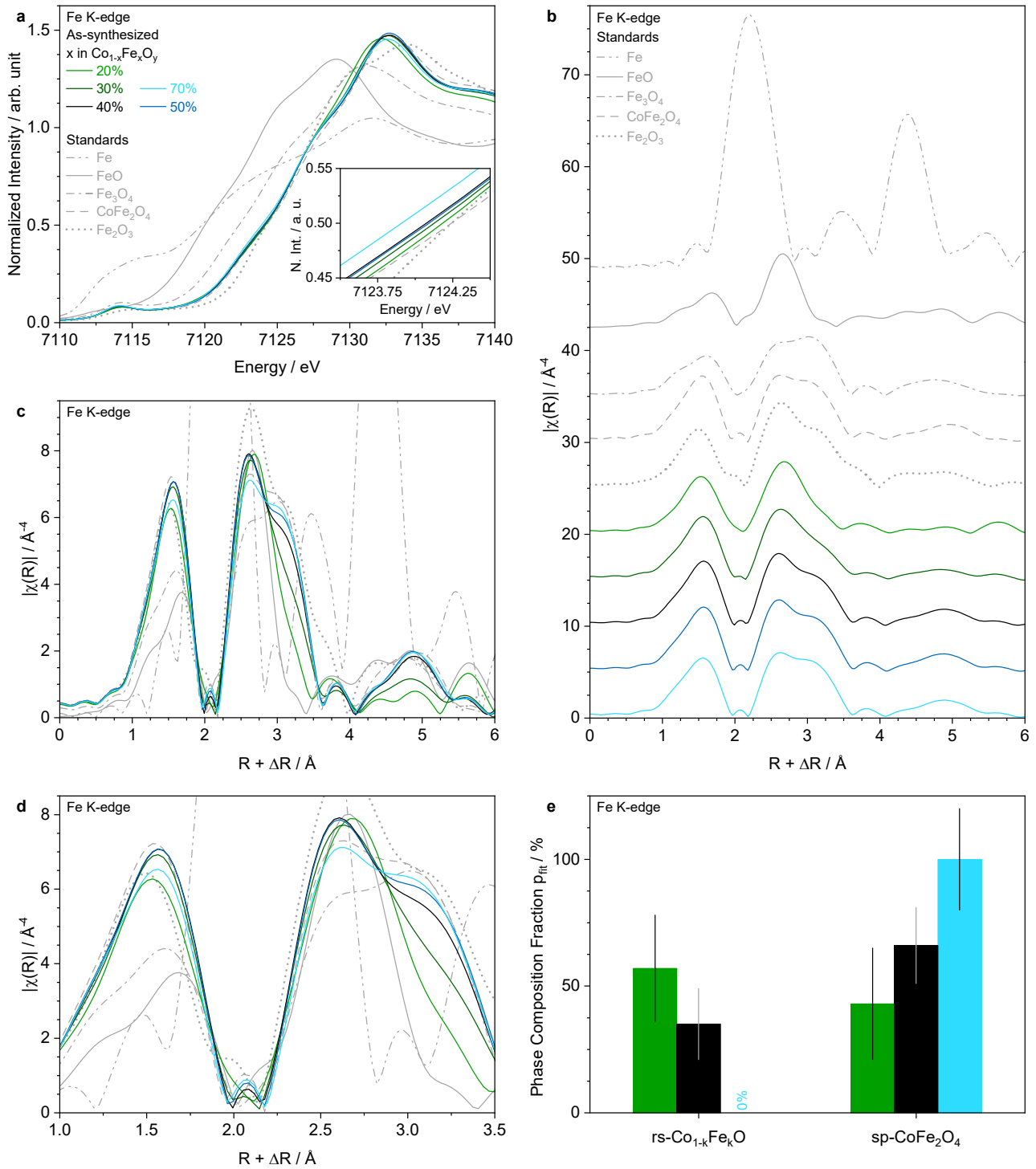


Figure S7. As-synthesized Fe-K edge XAS: Fe^{3+} but gradual rock-salt (rs) to spinel (sp) structure change within $\text{Co}_{1-x}\text{Fe}_x\text{O}_y$ series. (a) XANES of Fe K-edge spectra of the $\text{Co}_{1-x}\text{Fe}_x\text{O}_y$ series. Inset (a) Magnified XANES around half-normalized intensity. (b) Magnitude of k^3 -weighted FT-EXAFS from Fe K-edge spectra (k -range from 2.7 to 11.4 \AA^{-1}). (c) and (d) Same data as shown in (b) but overlaid or overlaid and magnified. (e) Phase composition fractions (p_{fit}) for as-synthesized materials with $x = 0.20, 0.40$, and 0.70 extracted from FT-EXAFS best fits in Figure S9 with fitting errors as vertical lines. Refer to Methods for ICSD collection code of the standards used in hard XAS (XANES, FT EXAFS, and fitting process) and to Tables S6-S8 for the fitting values. The color code of the $\text{Co}_{1-x}\text{Fe}_x\text{O}_y$ series as defined in (a) is valid in all figures.

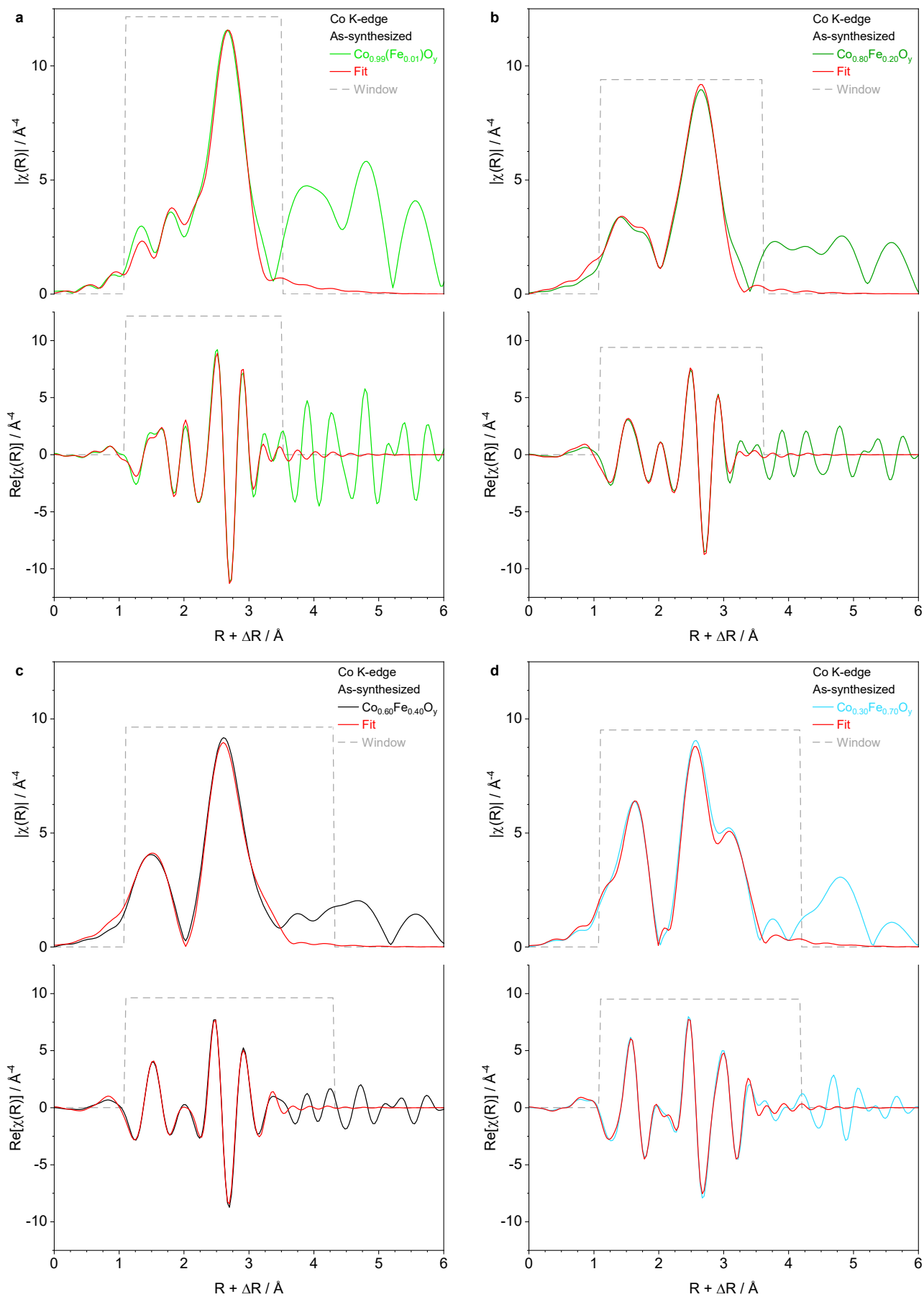


Figure S8. As-synthesized Co K-edge FT-EXAFS best fits: Gradual rock-salt (rs) to spinel (sp) structure change within $\text{Co}_{1-x}\text{Fe}_x\text{O}_y$ series. (a)-(d) Magnitude and real parts of k^3 -weighted FT-EXAFS best fits at Co K-edge for $\text{Co}_{1-x}\text{Fe}_x\text{O}_y$ series with $x = 0.01, 0.20, 0.40$, and 0.70 (k -range from 3 to 11.5 \AA^{-1}). Refer to Methods for ICSD collection code of the standards used in the fitting and to Tables S2-S5 for the fitting values.

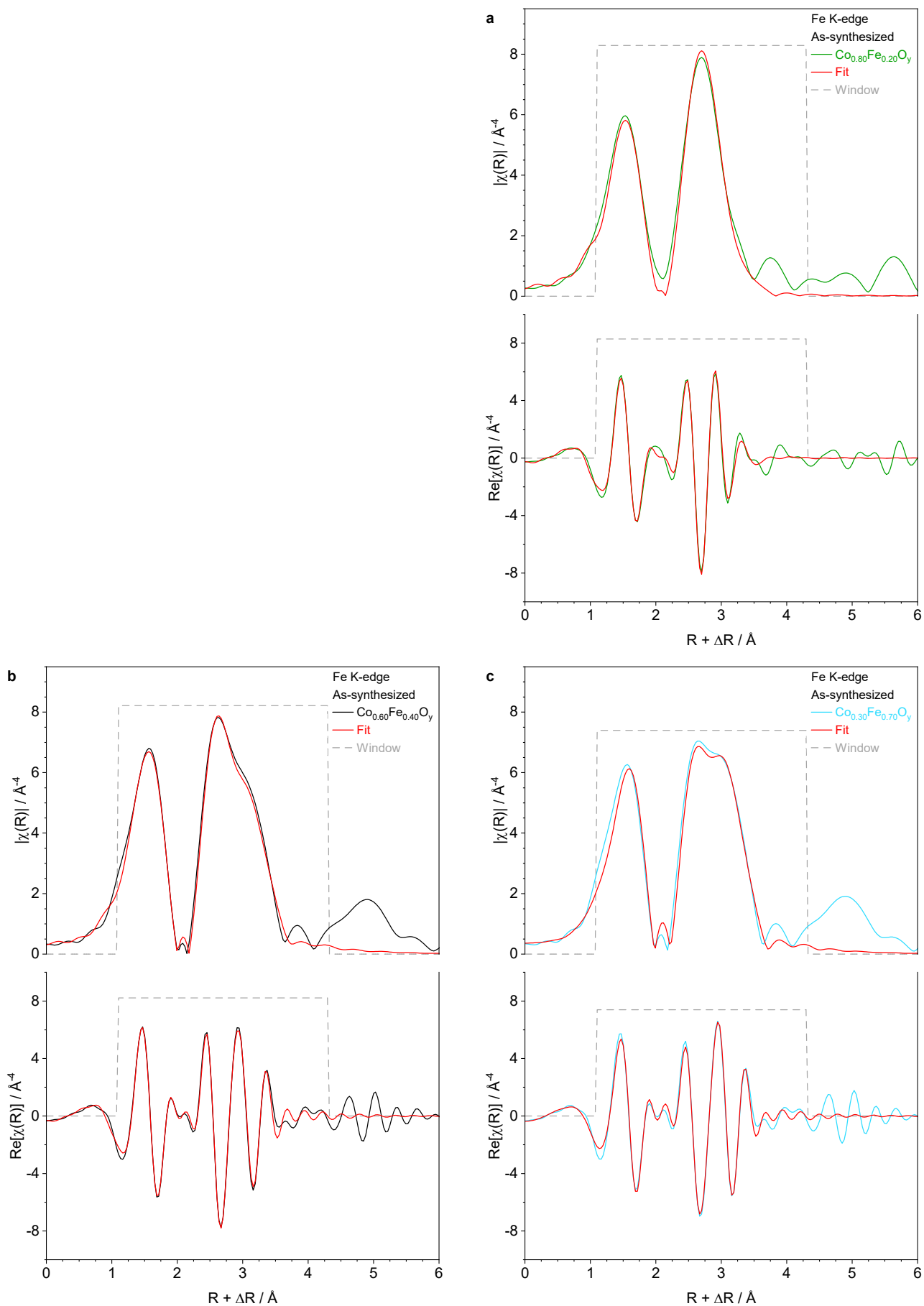


Figure S9. As-synthesized Fe K-edge FT-EXAFS best fits: Gradual rock-salt (rs) to spinel (sp) structure change within $\text{Co}_{1-x}\text{Fe}_x\text{O}_y$ series. (a)-(c) Magnitude and real parts of k^3 -weighted FT-EXAFS best fits at Fe K-edge for $\text{Co}_{1-x}\text{Fe}_x\text{O}_y$ series with $x = 0.20, 0.40$, and 0.70 (k -range from 3 to 11.3 \AA^{-1}). Refer to Methods for ICSD collection code of the fitting models and to Tables S6-S8 for the fitting values.

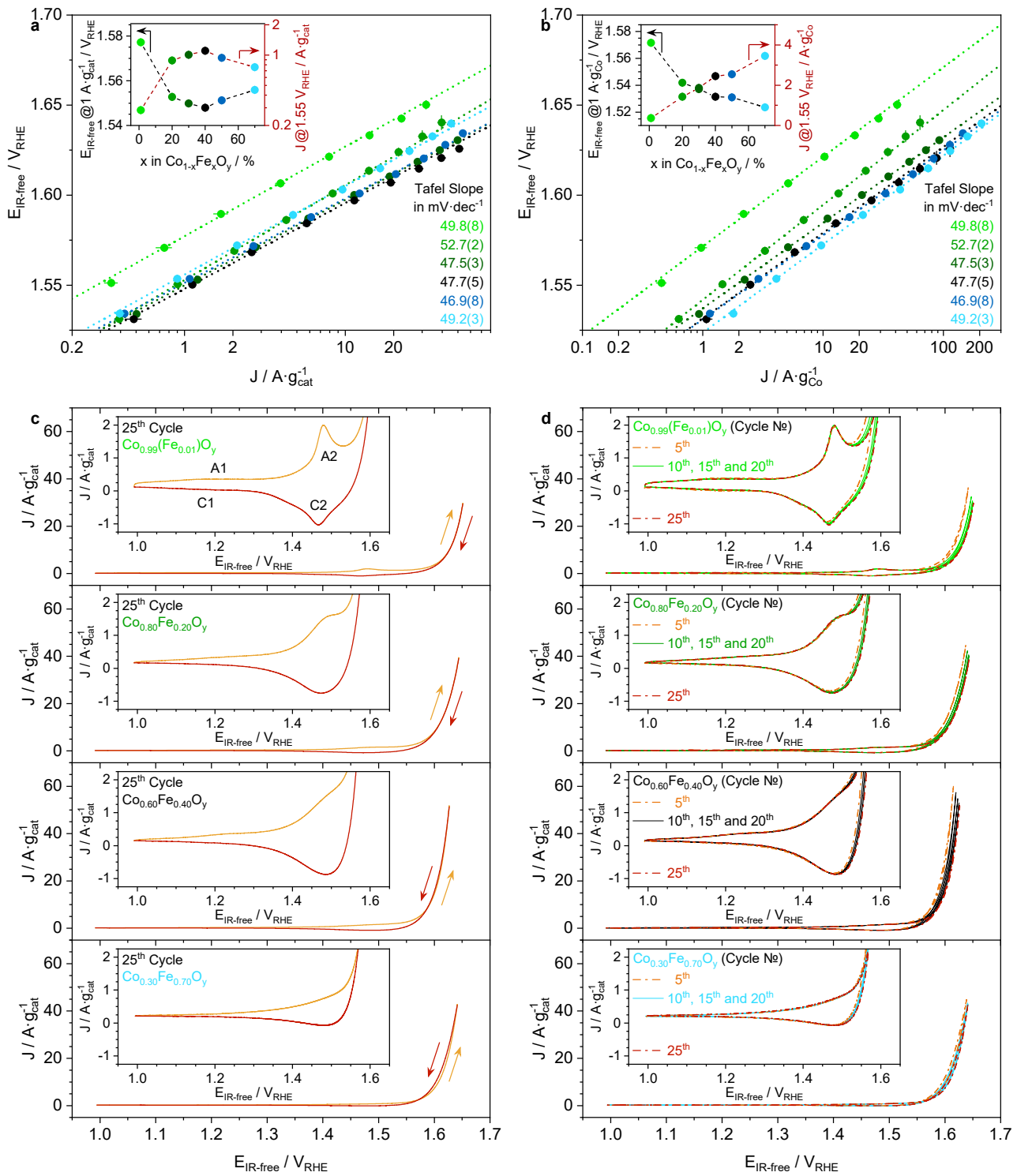


Figure S10. OER performance: Volcano-shaped activity, but with beneficial enhanced surface modifications within $\text{Co}_{1-x}\text{Fe}_x\text{O}_y$ series. (a) Tafel plot of RDE CA measurements with linear fit (dotted line). The horizontal and vertical lines indicate the error bar of three independent averaged measurements. Inset (a) U-shaped OER potentials at $1 \text{ A} \cdot \text{g}_{\text{cat}}^{-1}$ (left axis in black) and volcano-shaped OER current densities at $1.55 V_{\text{RHE}}$ (right axis in red) as a function of the Fe-content. (b) Same plot as (a) but the OER current is normalized by the Co-mass (from ICP-OES) and not by the total mass of the electrocatalyst. (c) Positive (orange) and negative going potential scan afterwards (red) of the 25th (last) CV cycle measured with $10 \text{ mV} \cdot \text{s}^{-1}$ prior to CA's. (d) 5th (orange dash-dotted line), 10th, 15th, 20th, and 25th (red dash-dotted line) CV cycle measured with $10 \text{ mV} \cdot \text{s}^{-1}$ prior to CA's. All electrochemical experiments were performed in 0.1 M KOH (saturated with syn air) at room temperature.

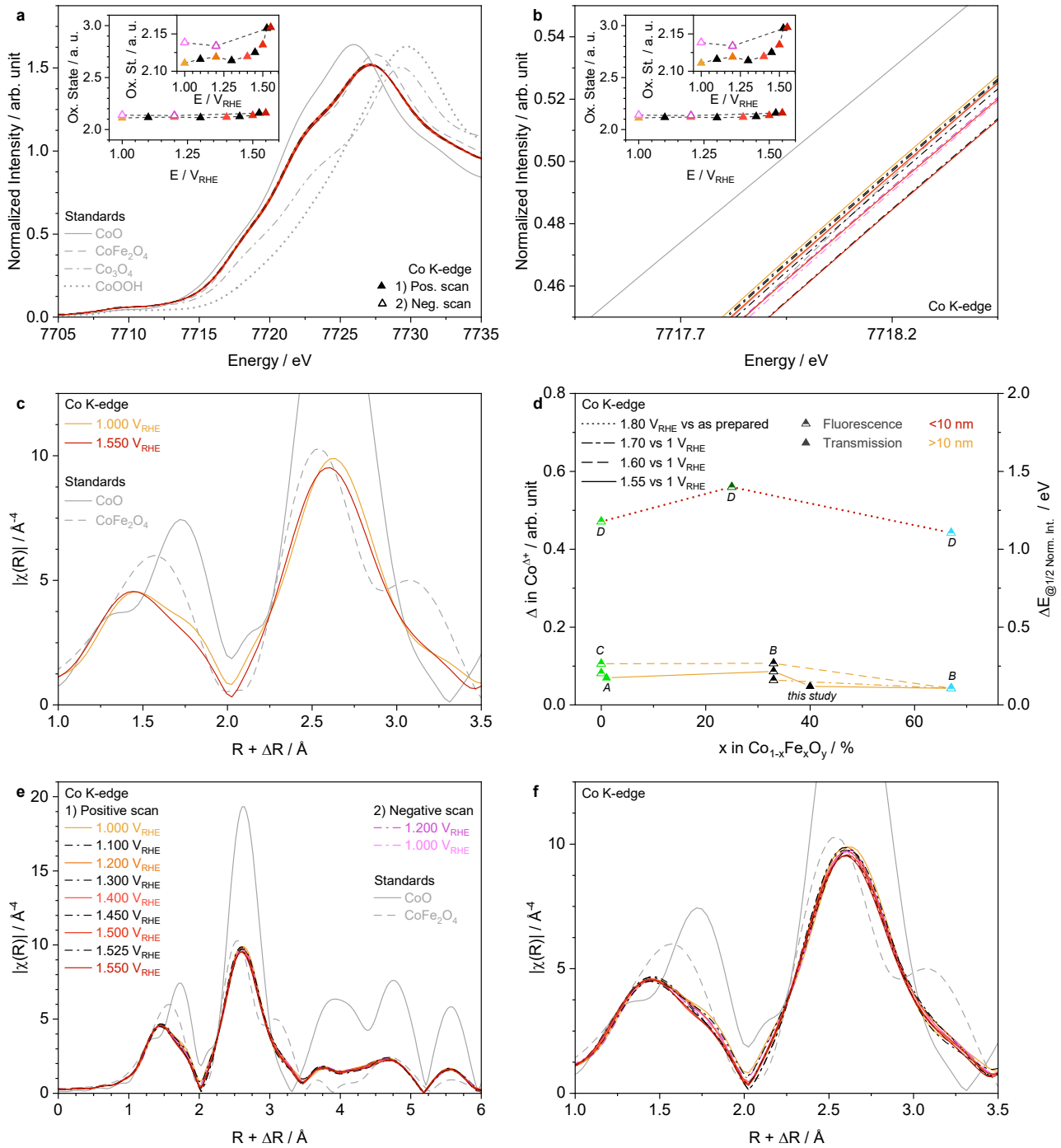


Figure S11. Bulk during OER process: Minor changes at the Co K-edge of $\text{Co}_{0.60}\text{Fe}_{0.40}\text{O}_y$. (a) and (b) Operando XANES of all measured potentials in the positive and negative going potential scan afterwards once over the whole energy range and once magnified in the range of the half-normalized intensity. Inset (a) and (b) Operando Co oxidation state for all measured potentials. (c) Operando magnitudes of FT-EXAFS at 1.00 and 1.55 V_{RHE} (not IR-free) magnified overlaid. (d) Operando Co oxidation state change (left axis) and energy shift (right axis) at half-normalized intensity (~7718-7719 eV) of nanoparticles above 10 nm (>10 nm) from this study and from literature (A^{46} (0.1 M KOH), B^{47} (0.1 M KOH) and C^{48} (0.1 M KPi at pH 7)), and sub-10 nm (<10 nm) from literature (D^{49} (0.1 M KOH)). The energy shift for 1.55 V in B was linearly interpolated between 1.40 and 1.60 V. The energy shift for 1.60 V in C was linearly interpolated between 1.55 and 1.62 V. (e) and (f) Overlaid and magnified overlaid operando magnitudes of FT-EXAFS for all measured potentials in the positive and negative going potential scan afterwards. The corresponding operando Fe K-edge XANES and FT-EXAFS magnitudes are shown in Figure S12. The color code for the different potentials as defined in (e) and the symbols as defined in (a) is valid in all figures.

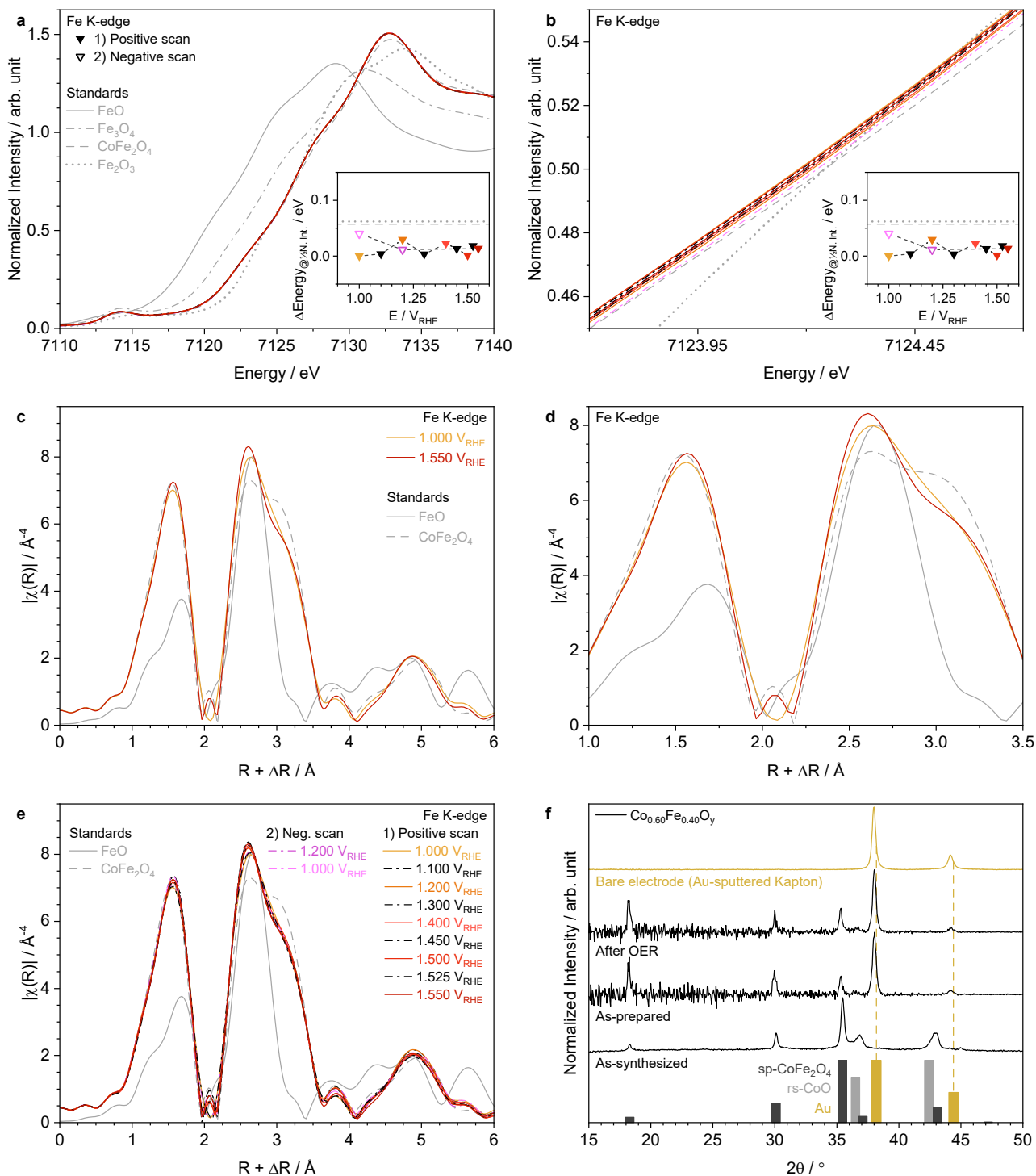


Figure S12. Bulk during OER process: No changes at the Fe K-edge and XRD of $\text{Co}_{0.60}\text{Fe}_{0.40}\text{O}_y$. (a) and (b) Operando XANES of all measured potentials in the positive and negative going potential scan afterwards once over the whole energy range and once magnified in the range of the half-normalized intensity. Inset (a) and (b) Energy shift at half-normalized intensity relative to the spectra measured at 1.00 V_{RHE} (not IR-free) for all measured potentials. (c) and (d) Operando magnitudes of FT-EXAFS at 1.00 and 1.55 V_{RHE} (not IR-free) overlaid and magnified overlaid. (e) Overlaid operando magnitudes of FT-EXAFS for all measured potentials in the positive and negative going potential scan afterwards. The color code for the different potentials as defined in (e) and the symbols as defined in (a) is valid in all figures. (f) XRD of $\text{Co}_{0.60}\text{Fe}_{0.40}\text{O}_y$ as-synthesized power, as-prepared electrode for operando XAS and ex situ after operando XAS measurement (after OER). The XRD patter of the bare Au-sputtered and carbon coated Kapton® electrode is added to identify the additional diffraction peaks of the as-prepared and after OER electrode from Au. The electrodes were measured in transmission leading to larger noise at low 2θ and a decreasing intensity towards higher 2θ . The missing peak at 43° in the as-prepared and after OER XRD pattern is explained by the low intensity at this high 2θ value. Refer to Methods for ICSD collection code of the standards.

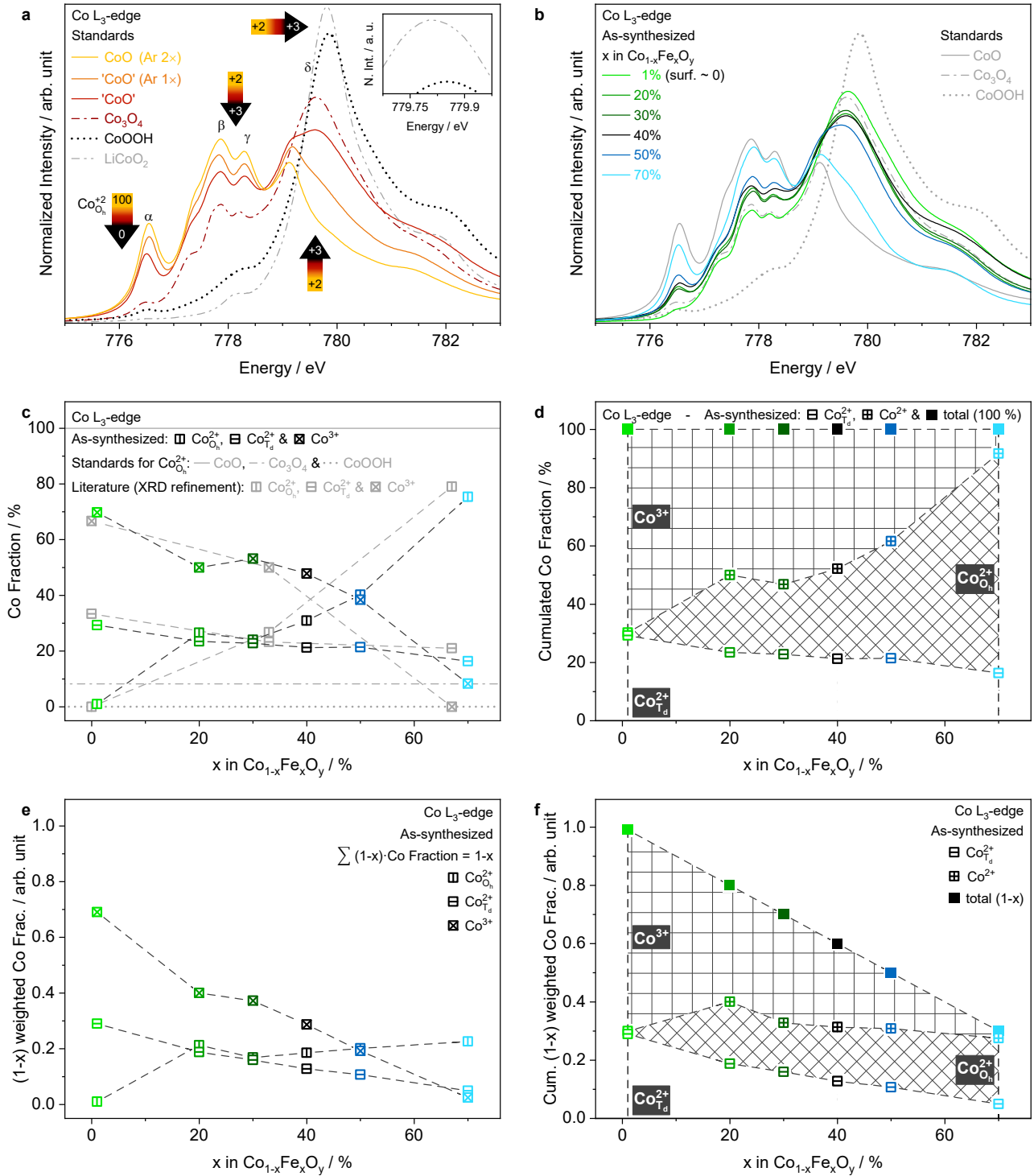


Figure S13. As-synthesized surface: From Co^{2.67+} to Co²⁺ within Co_{1-x}Fe_xO_y series. (a) Co L₃-edge TEY-XAS spectra of standard materials including LiCoO₂. Inset (a) Magnified (a) around the maximum of the δ peak for the Co³⁺ standards (CoOOH and LiCoO₂) revealing a similar peak position on the energy scale and thus, a similar oxidation state since the δ peak will shift towards higher energy, when the oxidation state is higher than +3.^{24,50,51} (b) Co L₃-edge TEY-XAS spectra of the complete as-synthesized Co_{1-x}Fe_xO_y series. (c) The fraction of Co, which is +2 and octahedrally (O_h) coordinated by oxygen atoms (B in AB₂O₄), of Co, which is +2 and tetrahedrally (T_d) coordinated by oxygen atoms (A in AB₂O₄), and of Co³⁺ (sum of the three types is 100%) in the complete as-synthesized Co_{1-x}Fe_xO_y series. The Co²⁺ in O_h-sites fraction for the standard materials are shown as horizontal line. The Co fractions for all types in the as-synthesized Co_{1-x}Fe_xO_y series determined from the Co L₃-edge are in good agreement with literature values determined with XRD refinement for Co₃O₄ (assuming a Co²⁺ in O_h-sites fraction of 0%), FeCo₂O₄, and CoFe₂O₄ (assuming for both to have only Fe³⁺).^{8,9} (d) Cumulative Co²⁺ in T_d-sites (bottom area), Co²⁺ in O_h-sites (middle area), and Co³⁺ fractions (top area) relative to all Co-atoms in the complete as-synthesized Co_{1-x}Fe_xO_y series. (e) Co mole fraction weighted Co²⁺ in O_h-sites, Co²⁺ in T_d-sites, and Co³⁺ fractions (sum of all is 1-x) as a function of the Fe-content. (f) Cumulated Co mole fraction weighted Co²⁺ in T_d-sites (bottom area), Co²⁺ in O_h-sites (middle area), and Co³⁺ fractions (top area) (sum of all is 1-x) as a function of the Fe-content. Refer to Methods for the procedure to assign the Co fractions.

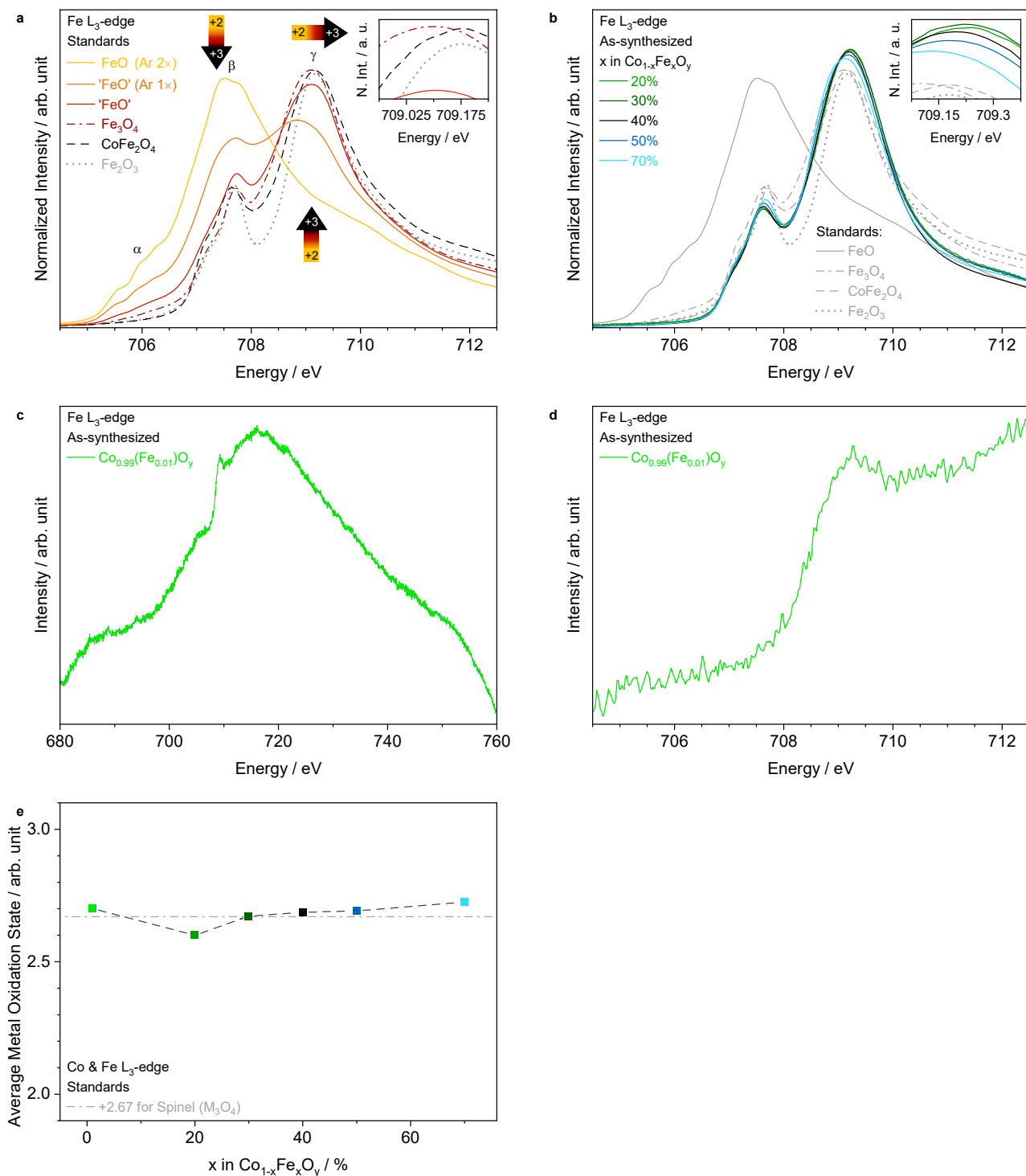


Figure S14. As-synthesized surface: Fe³⁺ within Co_{1-x}Fe_xO_y series. (a) and (b) Fe L₃-edge TEY-XAS spectra of standard materials and of the complete (except x = 0.01) Co_{1-x}Fe_xO_y series. As-purchased 'FeO' showed an oxidized surface layer and had to be sputtered 2x with argon-ions to achieve a Fe²⁺ standard spectra. Inset (a) Magnified (a) around the maximum of the γ peak revealing a similar peak position on the energy scale for the Fe³⁺ standards (CoFe₂O₄ and Fe₂O₃) and thus, a similar oxidation state e.g. in contrast to Fe₃O₄. The difference in the L₃-edge peak shape for the Fe³⁺ standards is coming from the different population of O_h-sites and T_d-sites within these materials. In α-Fe₂O₃ are all Fe-atoms in O_h-sites, while in CoFe₂O₄ are 40% of all Fe-atoms occupying the A-sites (T_d) of the spinel and 60% the B-sites (O_h).⁸ This difference leads then to a growth of the 'T_d' peak in the CoFe₂O₄ spectra, which lies between the two 'O_h' peaks (β and γ) as similarly seen in Fe₃O₄.²⁹ Inset (b) Magnified (b) around the maximum of the γ peak in the Co_{1-x}Fe_xO_y series. (c) and (d) I₀ corrected but not baseline corrected Fe L₃-edge TEY-XAS spectra of Co_{0.99}(Fe_{0.01})O_y over the whole scanning range and magnified revealing a barely detectable surface Fe signal. (e) Mole fraction weighted average surface metal oxidation state (OS) calculated with (1-x) · OS_{Co} + x · 3 as function of the Fe-content in the complete as-synthesized Co_{1-x}Fe_xO_y series. The mole fraction weighted average surface metal OS is in the complete series around +2.67, which is typical for a spinel-type composition.

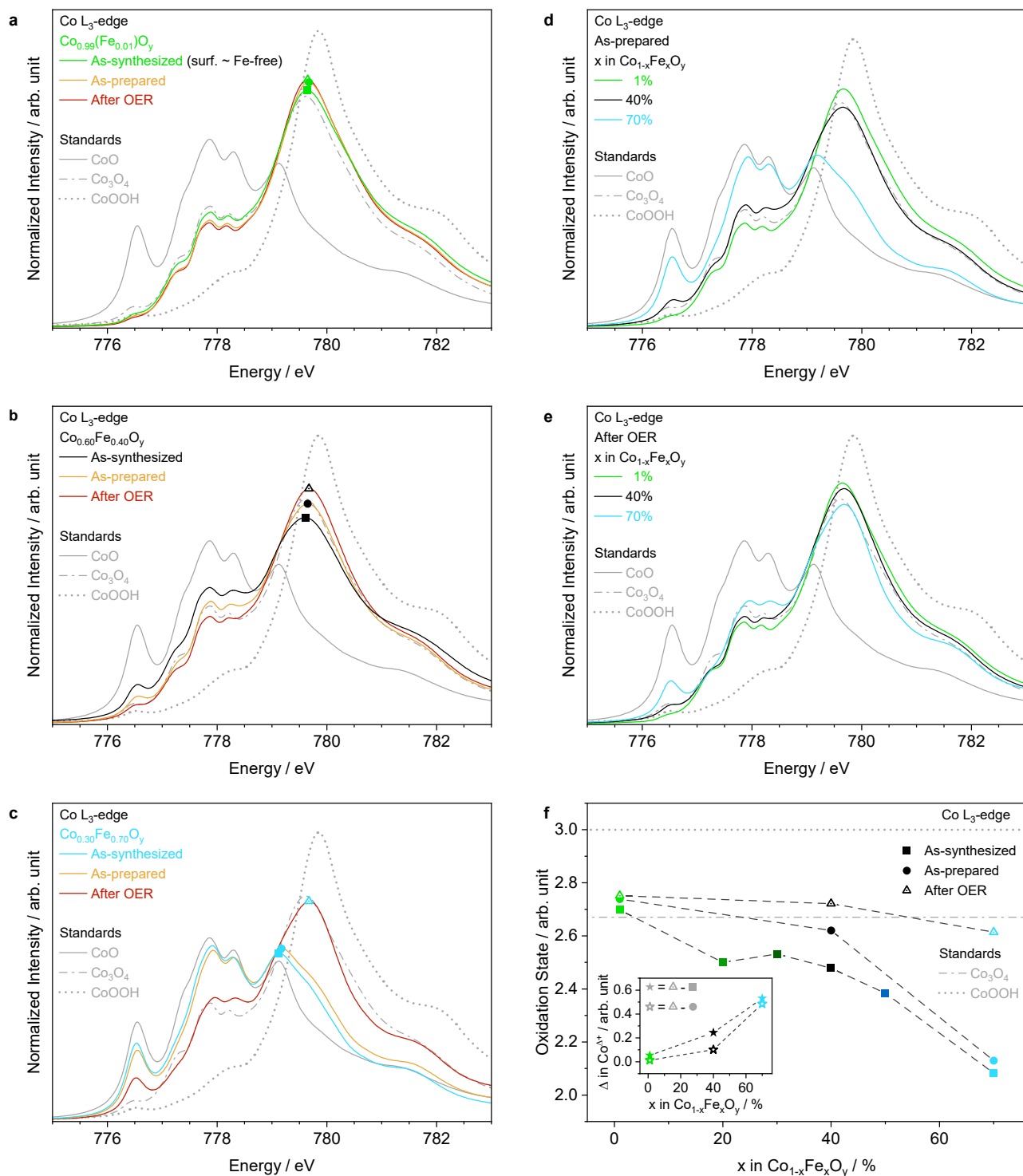


Figure S15. Surface after OER process: Irreversible surface Co oxidation within Co_{1-x}Fe_xO_y series. (a)-(c) Co L₃-edge TEY-XAS spectra of as-synthesized powder, 'as-prepared', and ex situ 'after OER' for Co_{0.99}(Fe_{0.01})O_y, Co_{0.60}Fe_{0.40}O_y, and Co_{0.30}Fe_{0.70}O_y. (d) Co L₃-edge TEY-XAS spectra of 'as-prepared' sample for Co_{0.99}(Fe_{0.01})O_y, Co_{0.60}Fe_{0.40}O_y, and Co_{0.30}Fe_{0.70}O_y. (e) Ex situ Co L₃-edge TEY-XAS spectra of 'after OER' sample for Co_{0.99}(Fe_{0.01})O_y, Co_{0.60}Fe_{0.40}O_y, and Co_{0.30}Fe_{0.70}O_y. (f) Surface Co oxidation state trend in the 'as-synthesized', 'as-prepared', and 'after OER' Co_{1-x}Fe_xO_y series. Inset (f) Trend in the surface Co oxidation state change 'after OER' revealing the independence of using either the 'as-synthesized' or 'as-prepared' spectra as baseline. The corresponding Fe L₃-edge spectra are shown in Figures S16 and S17. Refer to Methods for the procedure to assign the surface Co oxidation states.

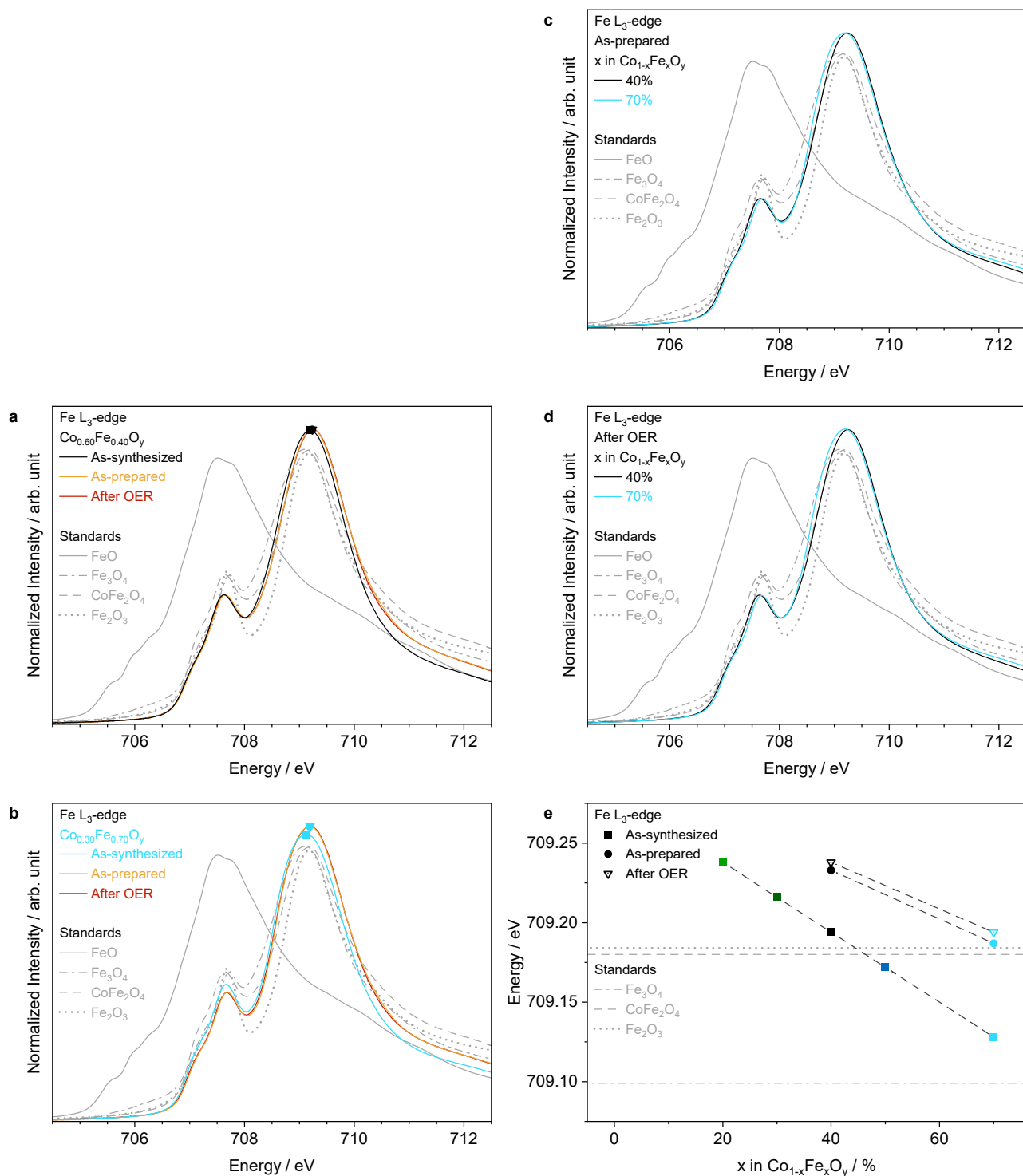


Figure S16. Surface after OER process: Minor irreversible surface Fe oxidation within Co_{1-x}Fe_xO_y series. (a) and (b) Fe L₃-edge TEY-XAS spectra of as-synthesized powder, 'as-prepared' electrode, and ex situ 'after OER' for Co_{0.60}Fe_{0.40}O_y and Co_{0.30}Fe_{0.70}O_y. (c) Fe L₃-edge TEY-XAS spectra of 'as-prepared' Co_{0.60}Fe_{0.40}O_y and Co_{0.30}Fe_{0.70}O_y. (d) Ex situ Fe L₃-edge TEY-XAS spectra of 'after OER' for Co_{0.60}Fe_{0.40}O_y and Co_{0.30}Fe_{0.70}O_y. (e) Energy position of the γ Fe L₃-edge peak maximum of 'as-synthesized', 'as-prepared', and 'after OER' sample for Co_{1-x}Fe_xO_y series to assign a surface Fe oxidation state trend.

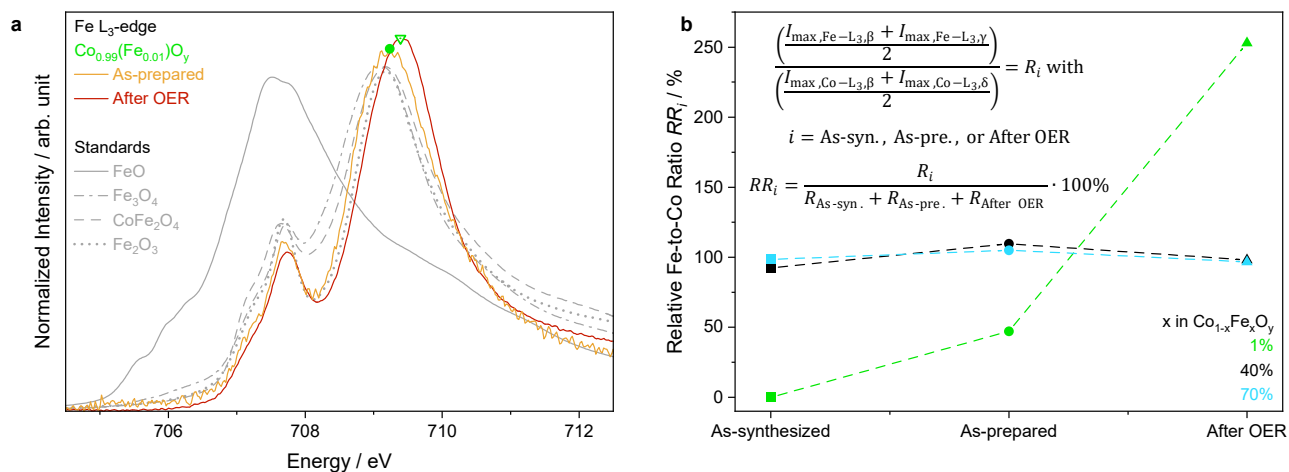


Figure S17. Surface after OER process: Increasing signal intensity at the Fe L₃-edge in $\text{Co}_{0.99}(\text{Fe}_{0.01})\text{O}_y$. (a) Fe L₃-edge TEY-XAS spectra of 'as-prepared' electrode and ex situ 'after OER' sample for $\text{Co}_{0.99}(\text{Fe}_{0.01})\text{O}_y$. (b) Relative surface Fe-to-Co ratio change in the different samples calculated by using the averaged intensity per edge (baseline corrected but not normalized), which were used e.g. to normalize the spectra. The surface Fe-to-Co ratio is almost unchanged in $\text{Co}_{0.60}\text{Fe}_{0.40}\text{O}_y$ and $\text{Co}_{0.30}\text{Fe}_{0.70}\text{O}_y$, but is significantly increasing in $\text{Co}_{0.99}(\text{Fe}_{0.01})\text{O}_y$ relative from a negligible surface Fe signal in the as-synthesized power (Figure S14c,d), to a clear but noisy peak in the 'as-prepared' sample and finally, to a noise-free signal 'after OER'. The absolute surface Fe-to-Co ratio in the 'after OER' sample of $\text{Co}_{0.99}(\text{Fe}_{0.01})\text{O}_y$ is still significantly less than for the higher Fe-content samples, but experienced within the sample series ('as-synthesized', 'as-prepared' and 'after OER') of $\text{Co}_{0.99}(\text{Fe}_{0.01})\text{O}_y$ the biggest increase relative to the other two materials ($x = 0.40$ and 0.70). The ICP-OES showed that the 0.1 M KOH was not the source of Fe and not responsible for the significant increase in the relative Fe-to-Co ratio in $\text{Co}_{0.99}(\text{Fe}_{0.01})\text{O}_y$ 'after OER'. It is more likely that the Fe-source is the bulk of the $\text{Co}_{0.99}(\text{Fe}_{0.01})\text{O}_y$ nanoparticles. Thus, Fe is moving from the bulk to the surface and gets there accumulated by forming probably a separate phase of Fe_2O_3 during sample preparation (probably due to the sonication) and more enhanced during the OER process itself.⁵² Overall, this proves that also irreversible changes are possible on the surface of $\text{Co}_{0.99}(\text{Fe}_{0.01})\text{O}_y$ and at the Fe L₃-edge. Moreover, soft XAS in TEY can also deliver information about the relative ratios of different elements and their changes during processes on the electrocatalyst surface.

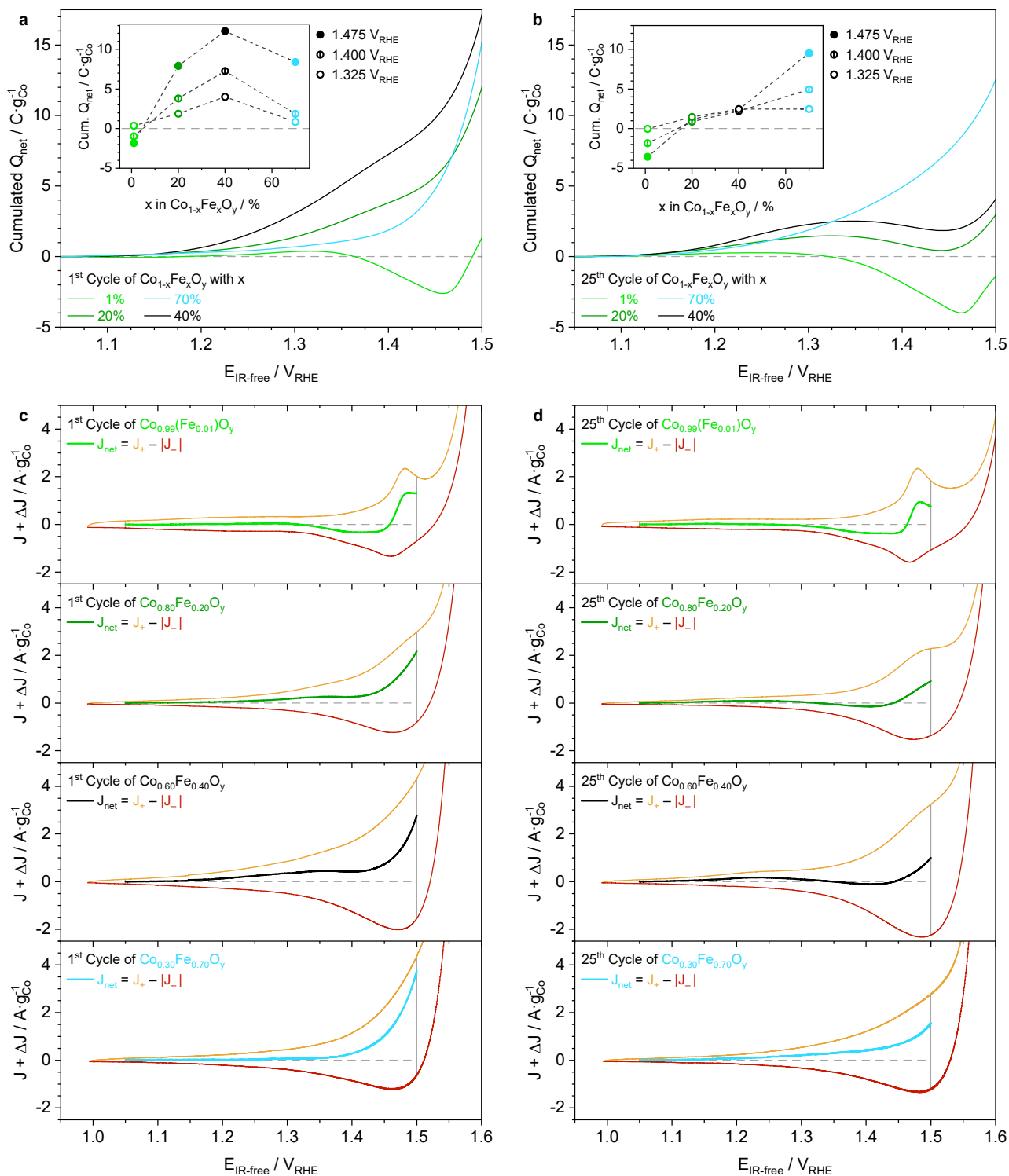


Figure S18. Enhanced irreversible surface Co oxidation within $\text{Co}_{1-x}\text{Fe}_x\text{O}_y$ series by pseudocapacitive processes. (a) and (b) Co-mass (from ICP-OES) normalized cumulated net charge (Q_{net}) from pseudocapacitive processes calculated for the 1st and 25th CV cycle between 1.05 and 1.5 V_{RHE} . Inset (a) and (b) Cumulated Q_{net} values at 1.325, 1.400, and 1.475 V_{RHE} for the 1st and 25th CV cycle as a function of the Fe-content. (c) and (d) Co-mass (from ICP-OES) normalized 1st and 25th CV cycle, respectively. The CVs were shifted on the y-axis so that the modulus of the current density for the positive (orange) and negative going potential scan afterwards (red) are equal at 1.05 V_{RHE} . The horizontal dashed grey line indicates 0 $\text{A} \cdot \text{g}_{\text{Co}}^{-1}$. The net current density (J_{net}), which is used to determine Q_{net} , represents the difference in the modulus of the current density between the positive (orange) and negative going potential scan afterwards (red) as calculated between 1.05 to 1.5 V_{RHE} as indicated with the vertical grey lines. The non-capacitive faradaic current density was not subtracted to determine J_{net} or Q_{net} so that the values above $\sim 1.45 V_{\text{RHE}}$ has to be considered with caution. However, the data clearly indicated an enhanced irreversible surface Co oxidation towards the higher Fe-content materials in the $\text{Co}_{1-x}\text{Fe}_x\text{O}_y$ series, (partially) excluding $\text{Co}_{0.30}\text{Fe}_{0.70}\text{O}_y$ due to the shift of the redox couple peak into OER potential range, and explains the observed trend in the ex situ 'after OER' Co L_3 -edge TEY-XAS spectra. Refer to Methods for more information regarding the analysis approach.

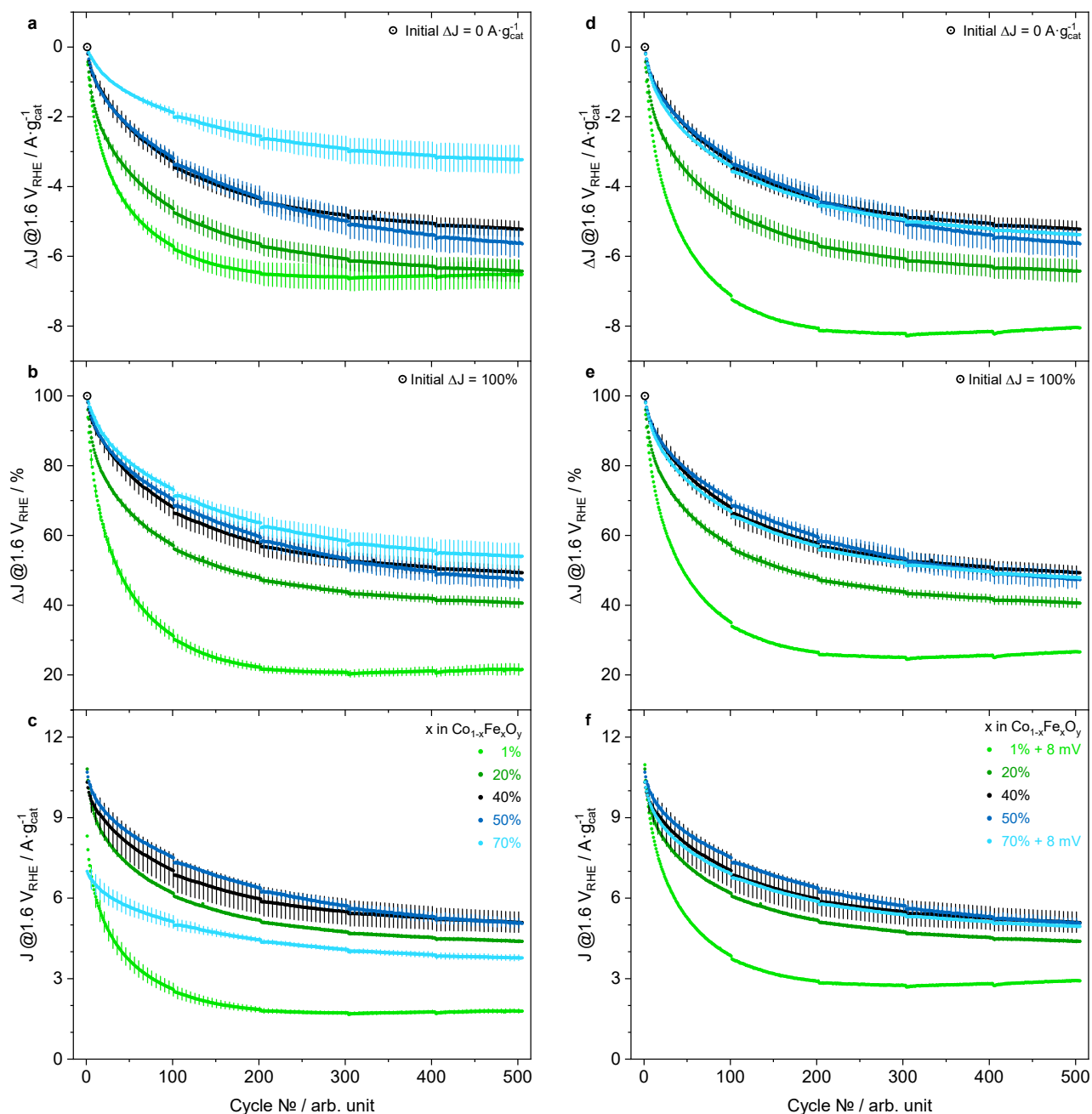


Figure S19. OER stability performance: Decreasing stability but less significant within $\text{Co}_{1-x}\text{Fe}_x\text{O}_y$ series. (a)–(c) Stability measurements shown as absolute OER current density changes in $\text{A}\cdot\text{g}_{\text{cat}}^{-1}$, as relative OER current density changes in % and as OER current density in $\text{A}\cdot\text{g}_{\text{cat}}^{-1}$ all taken at $1.6\text{ V}_{\text{RHE}}$ (not IR-free). (d)–(f) Differential potentiostatic stability measurements shown as absolute OER current density changes in $\text{A}\cdot\text{g}_{\text{cat}}^{-1}$, as relative OER current density changes in % and as OER current density in $\text{A}\cdot\text{g}_{\text{cat}}^{-1}$ taken at $1.6\text{ V}_{\text{RHE}}$ (not IR-free) for the initially more OER active electrocatalysts ($x = 0.20, 0.40$, and 0.50) and at $1.608\text{ V}_{\text{RHE}}$ (not IR-free) for the initially less OER active electrocatalysts ($x = 0.01$ and 0.70). The vertical lines indicate the error bar of four independent averaged measurements. The differential potentiostatic stability measurements at $1.608\text{ V}_{\text{RHE}}$ (not IR-free) for $x = 0.01$ and 0.70 were only performed once. All electrochemical experiments were performed in 0.1 M KOH (saturated with syn air) at room temperature. The color code of the $\text{Co}_{1-x}\text{Fe}_x\text{O}_y$ series as defined in (c) is valid in (a) and (b), and as defined in (f) is valid in figure (d) and (e).

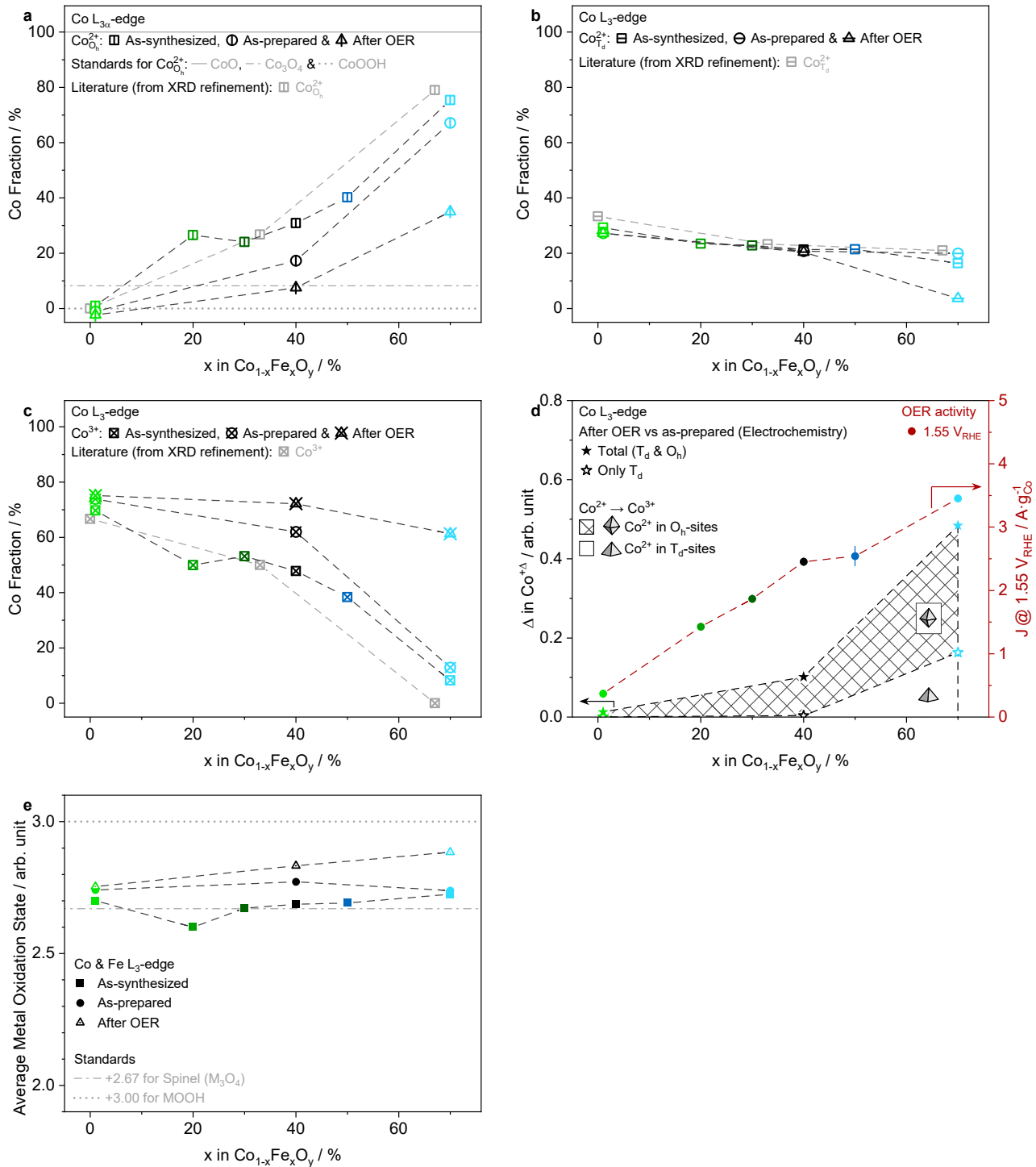


Figure S20. After OER vs as-prepared vs as-synthesized surface: Irreversible oxidation of Co²⁺ in O_h-sites within Co_{1-x}Fe_xO_y series. (a)-(c) Co²⁺ in O_h-sites (B in AB₂O₄), Co²⁺ in T_d-sites (A in AB₂O₄), and Co³⁺ fractions relative to all Co-atoms in the as-synthesized, as-prepared and after OER Co_{1-x}Fe_xO_y series. The negative fraction of Co²⁺ in O_h-sites after OER for x = 0.01 lies in the assumed error range of 10%. (d) Total irreversible change of the surface Co oxidation state 'after OER' relative to 'as-prepared' assigned to the two different Co²⁺ sources of T_d-sites (bottom area) and O_h-sites (top area) on left axis (in black) vs OER current normalized per mass of Co at 1.55 V_{RHE} on right axis (in red) as a function of the Fe-content. The vertical lines for the OER current densities indicate the error bar of three independent averaged measurements. All electrochemical experiments were performed in 0.1 M KOH (saturated with syn air) at room temperature. (e) The 'as-synthesized' (same as Figure S14e), 'as-prepared', and ex situ 'after OER' mole fraction weighted average surface metal oxidation state (OS) calculated with (1-x) · OS_{Co} + x · 3 as function of the Fe-content in the complete Co_{1-x}Fe_xO_y series. Refer to Methods for the procedure to assign the surface Co oxidation state and fraction changes.

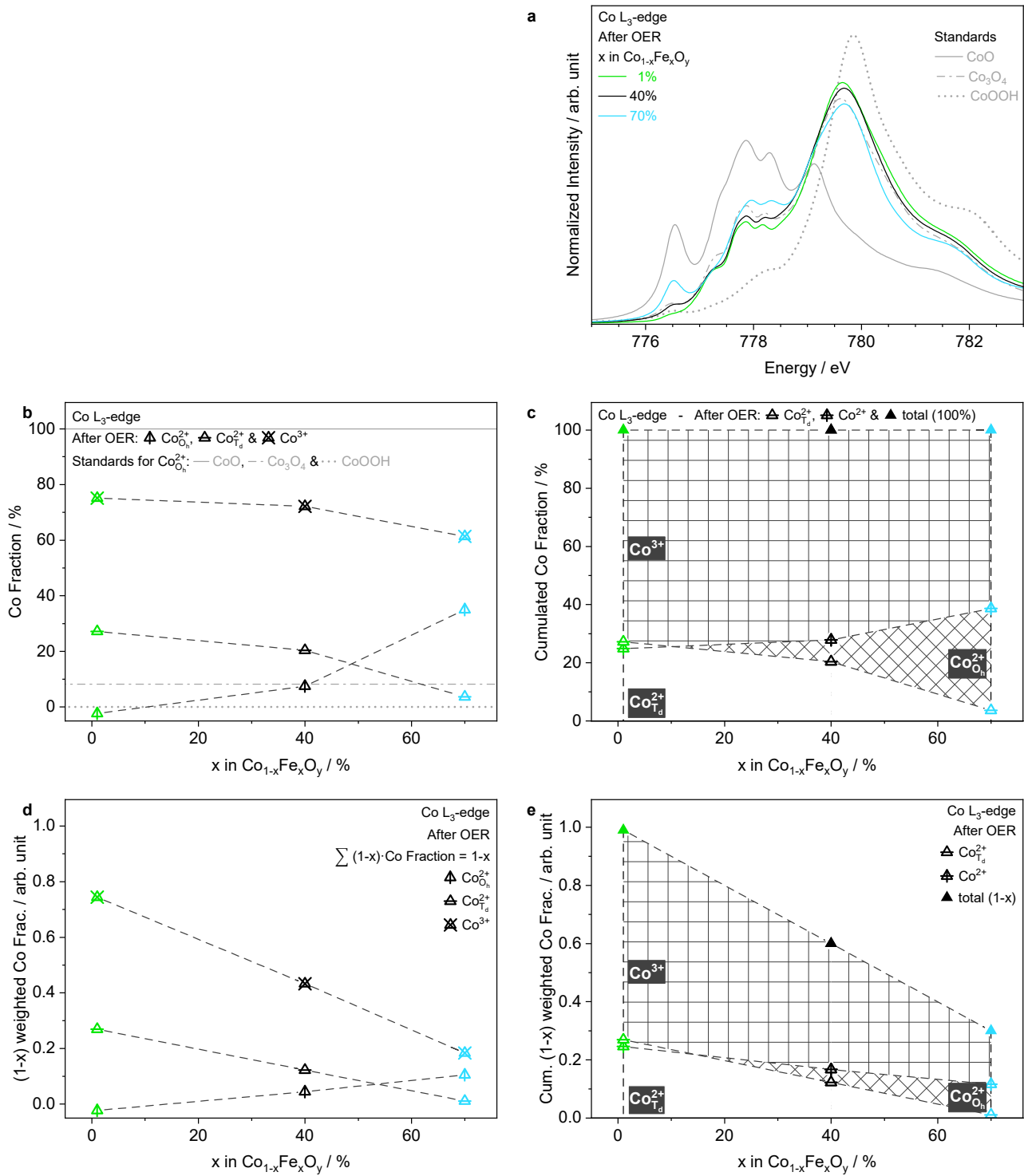


Figure S21. Surface after OER process: Increase of Co³⁺ and decrease of Co²⁺ fractions. (a) Ex situ Co L₃-edge TEY-XAS spectra at of the Co_{1-x}Fe_xO_y series after OER. (b) Co²⁺ in O_h-sites (B in AB₂O₄), Co²⁺ in T_d-sites (A in AB₂O₄), and Co³⁺ fractions relative to all Co-atoms (sum of the three types is 100%) in the Co_{1-x}Fe_xO_y series after OER. The Co²⁺ in O_h-sites fraction of the standard materials are shown as horizontal line. The negative fraction of Co²⁺ in O_h-sites after OER for x = 0.01 lies in the assumed error range of 10%. (c) Cumulative Co²⁺ in T_d-sites (bottom area), Co²⁺ in O_h-sites (middle area), and Co³⁺ fractions (top area) relative to all Co-atoms in the Co_{1-x}Fe_xO_y series after OER. (d) Co mole fraction weighted Co²⁺ in O_h-sites, Co²⁺ in T_d-sites, and Co³⁺ fractions (sum of all is 1-x) in the Co_{1-x}Fe_xO_y series after OER. (e) Cumulated Co mole fraction weighted Co²⁺ in T_d-sites (bottom area), Co²⁺ in O_h-sites (middle area), and Co³⁺ fractions (top area) (sum of all is 1-x) in the Co_{1-x}Fe_xO_y series after OER. Refer to Methods for the procedure to assign the Co fractions.

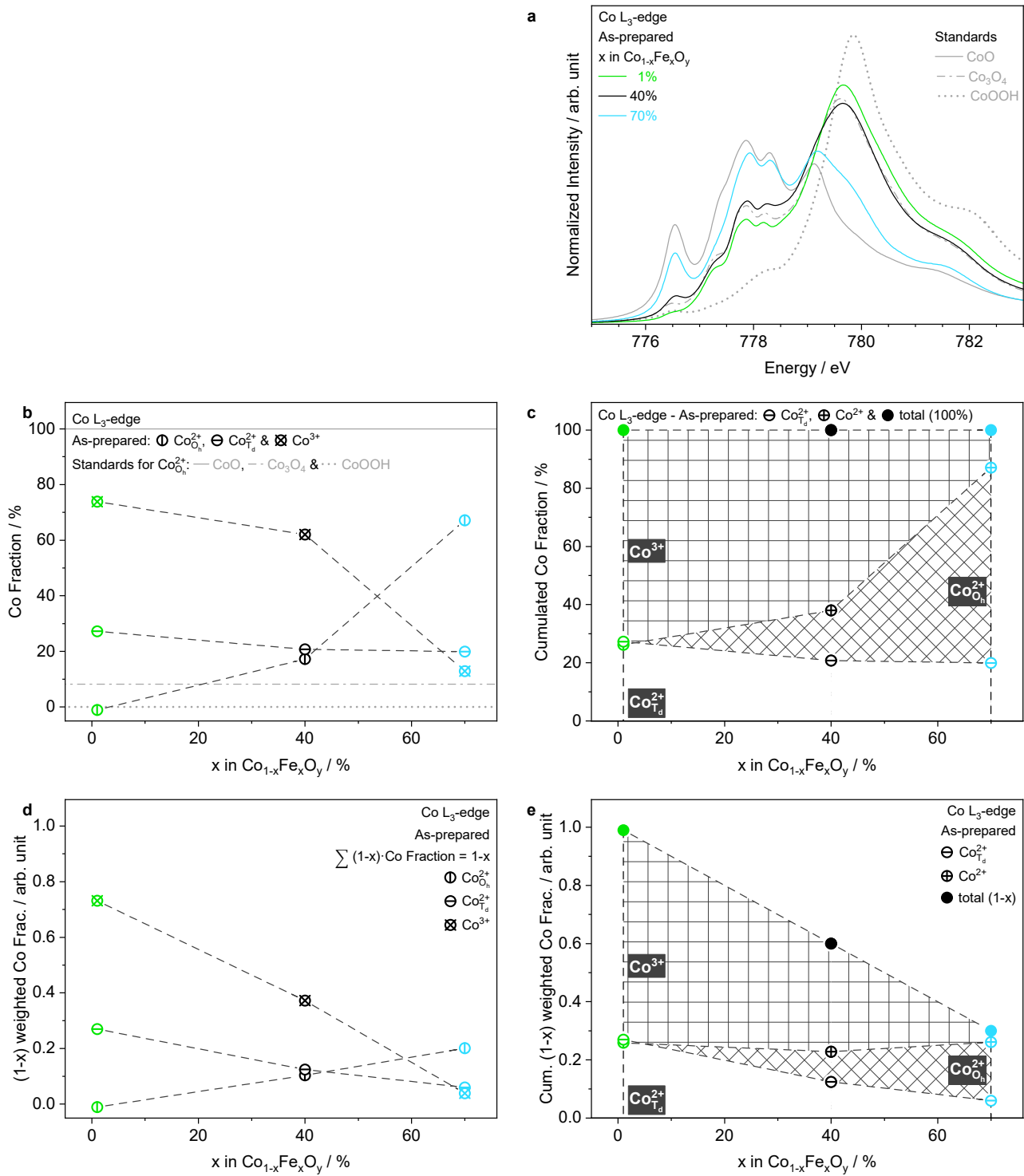


Figure S22. As-prepared surface: Minimal oxidation relative to as-synthesized Co_{1-x}Fe_xO_y series. (a) Co L₃-edge TEY-XAS of the as-prepared Co_{1-x}Fe_xO_y series. (b) Co²⁺ in O_h-sites (B in AB₂O₄), Co²⁺ in T_d-sites (A in AB₂O₄), and Co³⁺ fractions relative to all Co-atoms (sum of the three types is 100%) in the as-prepared Co_{1-x}Fe_xO_y series. The Co²⁺ in O_h-sites fraction of the standard materials are shown as horizontal line. (c) Cumulated Co²⁺ in T_d-sites (bottom area), Co²⁺ in O_h-sites (middle area), and Co³⁺ fractions (top area) relative to all Co-atoms in the as-prepared Co_{1-x}Fe_xO_y series. (d) Co mole fraction weighted Co²⁺ in O_h-sites, Co²⁺ in T_d-sites, and Co³⁺ fractions (sum of all is 1-x) in the as-prepared Co_{1-x}Fe_xO_y series. (e) Cumulated Co mole fraction weighted Co²⁺ in T_d-sites (bottom area), Co²⁺ in O_h-sites (middle area), and Co³⁺ fractions (top area) (sum of all is 1-x) in the as-prepared Co_{1-x}Fe_xO_y series. Refer to Methods for the procedure to assign the Co fractions.

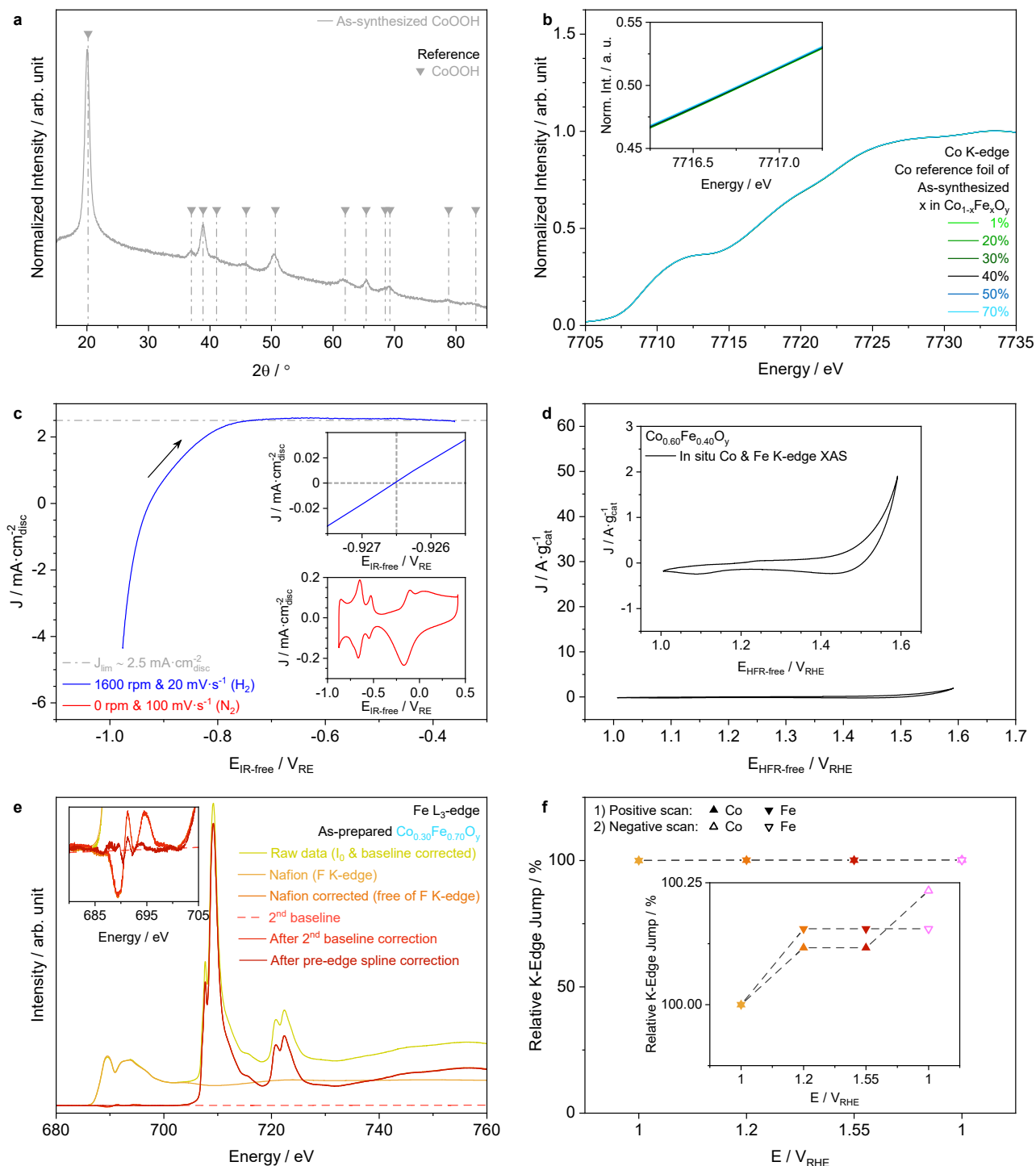


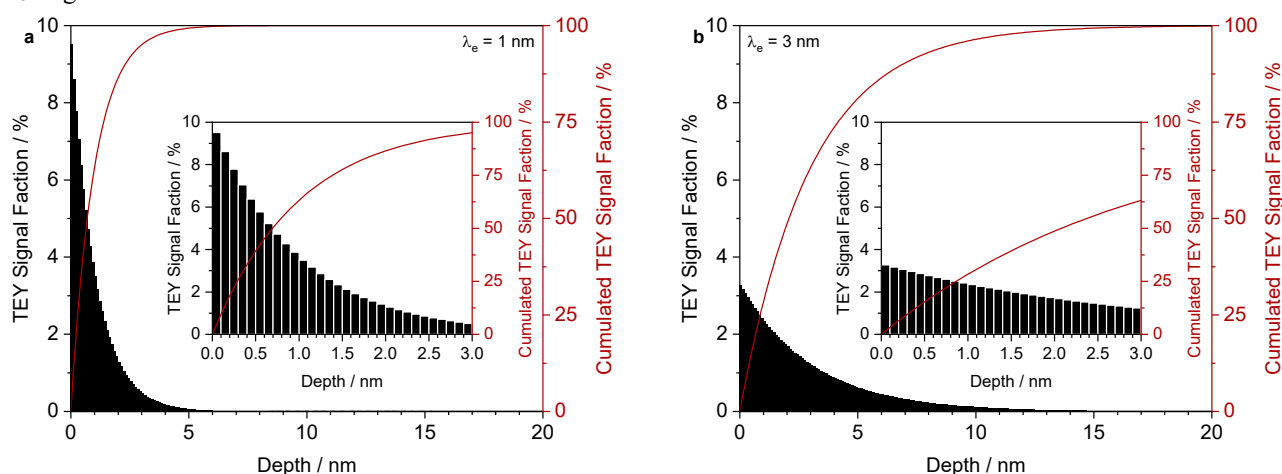
Figure S23. Detailed information about Methods: Varia. (a) Powder XRD of as-synthesized CoOOH standard material measured in Bragg-Brentano mode. The dash-dotted vertical lines were added for the reference pattern to guide the eyes of the reader. Refer to Methods for ICSD collection code of the reference pattern. (b) Aligned reference foil XANES at Co K-edge. Inset (b) Magnified (b) around the half-normalized intensity revealing the well aligned reference foil spectra representative for all shown spectra in this study. (c) Hg/HgO reference electrode calibration against the RHE in hydrogen (H_2) saturated 0.1 M KOH electrolyte solution. The overlap between the experimental and theoretical diffusion limited hydrogen oxidation reaction (HOR) current density (J_{lim}) indicates a satisfying hydrogen saturation in the electrolyte solution.^{2,38–40,53} Insets (c) Top: Magnified (c) around zero current density to precisely determine the potential offset of around $-0.9265 \text{ V}_{\text{RHE}}$ vs Hg/HgO . Bottom: CV of polycrystalline platinum disk insert in nitrogen (N_2) saturated 0.1 M KOH prior to reference electrode calibration to prove an initial clean surface. (d) CV measured with $10 \text{ mV} \cdot \text{s}^{-1}$ after the operando hard XAS experiments inside the flow cell using 0.1 M KOH . The cathodic and anodic redox peak at 1.1 and $1.25 \text{ V}_{\text{RHE}}$ (not IR but high frequency resistance (HFR) corrected) respectively, are coming from the Au of the working electrode. (e) Step-wise description of F K-edge correction originating from Nafion in all measured 'as-prepared' and 'after OER' Fe L_3 -edge spectra. (f) Relative change of the Co and Fe K-edge jump in the operando hard XAS experiments of $\text{Co}_{0.60}\text{Fe}_{0.40}\text{O}_y$ revealing no material losses during the measurements.

Supporting Information Notes

Note S1. The term 'operando' is used in this study according to the definition by Bert M. Weckhuysen⁵⁴ and Miguel A. Bañares et al.⁵⁵⁻⁵⁸ They defined that spectroscopic studies of catalysts are called operando when they are performed under real reaction conditions and when the structure and activity/selectivity of the catalyst is measured simultaneously. In this study, electrocatalysis is interpreted as a special case, where spectroscopic measurements are always operando during non-capacitive faradaic processes such as OER, since the recording of the OER current density acts as an on-line activity measurement.

Note S2. The presence of both, cobalt and iron, are required to maximize the OER activity and stability for these materials. However, some studies claim that iron is the active site in those mixed oxides and cobalt forms only the conductive host,⁵⁹ while results from other studies are questioning this due to the missing OER activity of iron-sites in other conductive cobalt-free materials such as carbon black⁶⁰ or metal-organic frameworks (MOFs).⁶¹⁻⁶³ There is more consensus in the literature regarding the non-beneficial effect of iron towards the higher Fe-content oxides. These materials suffer from the insulating property of iron oxides, which is responsible for the decrease of OER activity, when the Fe-content becomes too high.⁵⁹

Note S3. The surface-sensitivity of Co and Fe L₃-edge TEY-XAS is specified with the probing depths of ~1-3 nm from literature.⁶⁴⁻⁶⁷ The probing depths / electron escape depths (λ_e) are experimentally determined by detecting the signal intensity change as a function of the sample thickness. The change is mathematically described with $1 - \exp(-t / \lambda_e)$, where t is the sample layer thickness and λ_e is the probing depth / electron escape depth.⁶⁴⁻⁷³ Overall, the TEY signal is the sum of the individual contributions from all atom layers, but with an exponential decreasing contribution the deeper the atom layer lies normal to the surface. The probing depth / electron escape depth describes the thickness of the sample normal to the surface, which is responsible for 63% ($0.63 = 1 - \exp(-1)$) for $t = \lambda_e$ of the TEY signal. The smaller the probing depth / electron escape depth is, the higher is the contribution of the 1st atom layer to the TEY signal and the more surface-sensitive is the measurement. The (cumulated) TEY signal fraction per atom layer is shown in the Note S3 Figure for the two extreme cases of $\lambda_e = 1$ and 3 nm as experimentally expected for uniform flat samples at the Co and Fe L₃-edge.⁶⁴⁻⁶⁷



Note S3 Figure. Total-electron-yield signal fraction versus depth. (a) and (b) The estimated (cumulated) TEY signal fraction as a function of the sample depth for the two extreme cases with probing depths / electron escape depths (λ_e) of 1 and 3 nm as experimentally expected for uniform flat samples at the Co and Fe L₃-edge.⁶⁴⁻⁶⁷ Inset (a) and (b) Same data as shown in (a) and (b) but magnified between 0 and 3 nm, which is necessary to reach the 63% cumulated TEY signal fraction for $\lambda_e = 3$ nm (Inset (b)). Contrarily, the cumulated TEY signal fraction is already 95% at 3 nm for $\lambda_e = 1$ nm (Inset (a)) and has therefore a more surface-sensitive TEY signal. Each column has a width of 0.1 nm and represents roughly a single atom layer.

Note S4. Co²⁺ (d⁷) with a high-spin (hs) or a low-spin (ls) state, which is octahedrally (O_h) coordinated by oxygen atoms, has an electronic configuration of $t_{2g}^5 e_g^2$ or $t_{2g}^6 e_g^1$, respectively, for the valence electrons. The same ion, which is tetrahedrally (T_d) coordinated by oxygen atoms, has an electronic configuration of $e_g^4 t_{2g}^3$ for the valence electrons (no difference between LS and HS state). Co³⁺ (d⁶) with a HS or a LS state in O_h-site has an electronic configuration of $t_{2g}^4 e_g^2$ or $t_{2g}^6 e_g^0$, respectively, for the valence electrons. The same ion with a HS or a LS state in T_d-sites has an electronic configuration of $e_g^3 t_{2g}^3$ and $e_g^4 t_{2g}^2$, respectively, for the valence electrons. These simplified configurations allow assigning the α peak in the Co L₃-edge exclusively to the transition from 2p_{3/2} into the low energetic orbital of t_{2g}^5 for HS Co²⁺ in O_h-sites based on two reasons:

(1) The transition into the low energetic orbital of t_{2g}^4 for HS Co^{3+} in O_h -sites or of e_g^3 for HS Co^{3+} in T_d -sites is shifted towards higher energy due to the higher oxidation state.

(2) In all other situations is the transition not possible as the low energetic orbital is completely filled.

Moreover, the HS state for Co^{2+} in an oxide is very typical (O^{2-} is a weak-field ligand) no matter if in O_h -sites (CoO^{74-76} or $\text{CoFe}_2\text{O}_4^{77}$) or in T_d -sites ($\text{Co}_3\text{O}_4^{78}$). This allows assigning the remaining Co^{2+} , which does not contribute to the α peak, to the Co^{2+} in T_d -sites fraction and not to the LS Co^{2+} in O_h -sites fraction, which would also not contribute to the α peak.

Note S5. The proposed surface composition of $\text{Co}(\text{Co}_{(1-1.5x)}\text{Fe}_{(1.5x)})_2\text{O}_4$ predicts a Co_3O_4 for $x = 0$, $\text{Co}(\text{Co}_{0.5}\text{Fe}_{0.5})_2\text{O}_4$ ($=\text{FeCo}_2\text{O}_4$) for $x = 1/3$, and CoFe_2O_4 for $x = 2/3$. However, both metals, if present, can occupy in reality the A- and B-sites of AB_2O_4 as known for CoFe_2O_4 , where 40% of the Fe^{3+} -atoms are sitting on the A-site.⁸

Note S6. The phase pure flame-spray synthesis of rock-salt CoO (rs- CoO) is known to be challenging. The first try in literature was not successful using cost-efficient nitrates as precursor by observing the spinel structure of Co_3O_4 (sp- Co_3O_4) as secondary phase.⁷⁹ Modifications of the precursor solution helped to decrease the amount of secondary phase, but it never vanished completely in all the trials. It was hypothesized that the broadening and decrease in the XRD peaks of the secondary sp- Co_3O_4 phase of the best trial is coming either from the fact that sp- Co_3O_4 starts forming smaller particles than rs- CoO or sp- Co_3O_4 starts covering the surface of all rs- CoO nanoparticles like a passivation layer. Anyway, similar results were obtained using different solvent mixtures^{46,80} or using less cost-efficient acetates precursor.⁸¹ This systematic problem of having phase impurities of sp- Co_3O_4 in rs- CoO is coming from two different aspects, the flame-spray synthesis itself and the nature of cobalt oxides.

First of all, the scalable flame-spray synthesis (FSS) technique is capable for the industrial production of nanoparticle metal oxides^{82,83} and thus, this synthesis technique is attractive to produce (electro-)catalysts for large-scale applications. Briefly, combustible metal precursors are dissolved in a solvent-mixture and gets then dispersed into small droplets followed by injection into the flame, where the nanoparticle metal oxides are formed. These nanoparticles will be guided with the help of vacuum pumps in a baghouse filter, where the product is collected. The metal ions and the formed nanoparticles will experience during the synthesis heating and cooling rates above more than several $1000 \text{ K} \cdot \text{s}^{-1}$, which make the technique quite unique.^{1,2} Especially the high cooling rate, which can be considered as a quenching step, when the particles are leaving the flame, is an important characteristic, so that the particles keeps its properties, formed at these high-temperatures, also afterwards at room temperature (RT) and atmospheric pressure. Next to these temperature rates is the high-temperature particle residence time (HTPRT) a crucial parameter to adjust the properties of the formed nanoparticles.^{2,84} Nevertheless, these characteristics of the technique allows only forming phase pure nanoparticles, when the difference in the properties at this high-temperature and at RT is small enough, so that no phase changes are occurring during the quenching, when the particles are leaving the flame. However, this seem to be exactly the problem for cobalt oxides. The rs- CoO / sp- Co_3O_4 phase diagram reveals that the rock-salt structure is preferentially formed at high-temperatures and lower oxygen partial pressures, while the opposite is the case for the spinel phase.⁸⁵⁻⁸⁷ At atmospheric pressure is the phase transition temperature between the spinel and rock-salt structure at around 1200 K. Therefore, the rs- CoO structure will be preferentially formed in the flame of the FSS ($\gg 1000 \text{ K}$), but then back at RT, a passivation layer of sp- Co_3O_4 can be formed on the surface, explaining why the spinel phase can be present on the surface of a FSS rs- CoO and why a surface-bulk discrepancy is existing already after the synthesis.

Note S7. The influence of the 0.1 M KOH electrolyte solution on the surface of the materials with $x = 0.01$, 0.40, and 0.70 was not investigated because Co^{2+} containing oxides most likely form a $\text{Co}(\text{OH})_2$ layer on their top surface (1st atom layer) in an alkaline solution. $\text{Co}(\text{OH})_2$ itself oxidizes only in an alkaline solution when an oxidation agent such as H_2O_2 is present, as shown here by the synthesis of the CoOOH standard from this precursor (refer to Methods).

Note S8. Irreversible structure changes such as amorphization and / or increase of the OER active surface area leading to larger redox peaks and higher activity cannot be completely excluded, since these processes can be masked by opposite resulting phenomena as indicated by the continuously decreasing OER current density during cycling (Figure 3d and Figure S10c,d). Possible phenomena include: Bubbles accumulation on the electrocatalyst surface⁸⁸⁻⁹² and the formation of an insulating (OER inactive) Fe_2O_3 surface layer.⁵² The latter is most likely observed in the 'after OER' Fe $\text{L}_{3\text{-edge}}$ peak relative to the 'as-prepared' or 'as-synthesized' spectra (Figure S17), where the $\text{Co}_{0.99}\text{Fe}_{0.01}\text{O}_y$ bulk is assumed as Fe-source and not the electrolyte⁵⁹ (0.1 M KOH), as ICP-OES demonstrated a Fe (and Co) signal below the detection limit (0.6 and 0.7 ppb for Fe and Co, respectively) in the electrolyte.⁹³

Note S9. One reason of the overall OER current density drop during CV cycling or stability protocols in RDE setups is masking of the electrocatalyst's surface by trapped oxygen bubbles. This decrease in the OER active surface area leads to a disproportionate "instability" in RDE relative to membrane electrode assembly (MEA) measurements, which are closer

to an industrial scale electrolyzer.⁸⁸⁻⁹² The absolute stability trend is therefore only of limited significance, but the relative trend in a material series can still yield meaningful insight. A stability trend, which is less influenced by a relative difference in bubble accumulation due to differences in the initial OER activity (and thus oxygen formation) for the individual electrocatalysts, was obtained by performing a so-called differential potentiostatic stability protocol (refer to Methods). The stability trend observed with this alternative type of protocol, which still neglects relative differences in bubble accumulation due to differences in morphology (particle size and porosity) for the individual electrocatalysts, confirmed the same Fe-content dependence as already observed in the original potentiostatic protocol (Figure S19).

Note S10. The OER as a complex interface process cannot be fully described with a single ex situ surface descriptor. An optimal OER activity descriptor has to include several factors such as particle size, conductivity and surface state. If the latter is characterized only ex situ, as in this study, only irreversible changes are detectable. Therefore, a complete picture on OER requires also the understanding of reversible changes as observed for $\text{Co}_{0.99}\text{(Fe}_{0.01}\text{)}\text{O}_y$, which will help to unveil the role of the formation or suppression of the probably highly reversible Co^{4+} -sites for a high OER activity.^{94,95} However, this would require an operando surface oxidation state sensitive technique, which is technically still challenging.

Note S11. Consequently, the remaining Co^{2+} in O_h -sites fraction in the ex situ 'after OER' Co L_{3} -edge TEY-XAS spectra of the material with $x = 0.70$ is attributed mostly likely to Co^{2+} -atoms, which are octahedrally coordinated by hydroxide ions within the new Co-Fe-(oxyhydr)oxide surface layer (Figure S21b-e).

Note S12. Which Co^{2+} -site, O_h or T_d , enhances the OER activity intrinsically more cannot be answered here and would require well-controlled model electrocatalysts to enlighten the geometrical-site-dependent OER activity question, which has been discussed contradictorily in the literature.^{96,97}

Supporting Information Tables

Table S1. ICP-OES Data

$\text{Co}_{1-x}\text{Fe}_x\text{O}_y$	Cobalt		Iron		Oxygen (estimated)	
	Total mass fraction $w_{\text{Co}} / -$	Metal mole fraction $1-x / -$	Total mass fraction $w_{\text{Fe}} / -$	Metal mole fraction $x / -$	Total mass fraction $w_{\text{O}} / -$	Corresponding oxygen mole fraction $y / -$
$\text{Co}_{0.99}\text{Fe}_{0.01}\text{O}_{1.05}$	0.77	0.99	0.01	0.01	0.22	1.05
$\text{Co}_{0.80}\text{Fe}_{0.20}\text{O}_{1.15}$	0.62	0.80	0.14	0.20	0.24	1.15
$\text{Co}_{0.70}\text{Fe}_{0.30}\text{O}_{1.20}$	0.54	0.70	0.21	0.30	0.25	1.20
$\text{Co}_{0.60}\text{Fe}_{0.40}\text{O}_{1.30}$	0.45	0.60	0.28	0.40	0.27	1.30
$\text{Co}_{0.50}\text{Fe}_{0.50}\text{O}_{1.38}$	0.37	0.50	0.35	0.50	0.28	1.38
$\text{Co}_{0.30}\text{Fe}_{0.70}\text{O}_{1.54}$	0.22	0.30	0.48	0.70	0.30	1.54

The relative standard deviation for the Co and Fe signals is estimated to be less than 5% for the absolute mass fractions (including ICP-OES, weight, and volume measurement errors) and less than 2% for the relative mole fractions (including only ICP-OES measurement errors). The relative standard deviations of the estimated absolute mass fractions and mole fractions for oxygen are higher as they also includes the error from adsorbed water on the weighed material and cation losses during the digestion process.

Table S2. Co K-Edge FT-EXAFS Magnitude Fitting Values of As-Synthesized $\text{Co}_{0.99}(\text{Fe}_{0.01})\text{O}_y$

Amplitude Reduction Factor $S_0^2 = 0.78 \pm 0.04$ & Energy Shift $\Delta E_0 = 6 \pm 3$ eV							
Scattering Path (Model)	Half Path Length R / Å	Theoretical Co- ordination Number N_{th} / -	Phase Composition Fraction p_{fit} / -	Coordination Number $N_{\text{th}} \cdot p_{\text{fit}} = N_{\text{fit}}$ / -	Cumulated Co- ordination Number N_{cum} / -	Mean Square Displacement σ^2 / Å ²	R-Factor R' / -
Co _{Oh} -O ₁ (Co ₃ O ₄ (B-site))	1.94 ± 0.05	6	0.19 ± 0.12 (2/3 in Co ₃ O ₄)	1.2 ± 0.7	5.2 ± 1.8	0.008 ± 0.007	0.012
Co _{Td} -O ₁ (Co ₃ O ₄ (A-site))	1.96 ± 0.05	4	0.10 ± 0.06 (1/3 in Co ₃ O ₄)	0.4 ± 0.2			
Co-O ₁ (CoO)	2.15 ± 0.04	6	0.60 ± 0.15	3.6 ± 0.9			
Co-Co ₁ (Co)	2.53 ± 0.04	12	0.13 ± 0.06	1.5 ± 0.7	8.7 ± 2.4	0.007 ± 0.002	
Co-Co ₁ (CoO)	3.03 ± 0.02	12	Same as Co-O ₁ (CoO)	7.2 ± 1.7			

Table S3. Co K-Edge FT-EXAFS Magnitude Fitting Values of As-Synthesized $\text{Co}_{0.80}\text{Fe}_{0.20}\text{O}_y$

Amplitude Reduction Factor $S_0^2 = 0.78 \pm 0.04$ & Energy Shift $\Delta E_0 = 5 \pm 3$ eV							
Scattering Path (Model)	Half Path Length R / Å	Theoretical Co- ordination Number N _{th} / -	Phase Composition Fraction p _{fit} / -	Coordination Number N _{th} ·p _{fit} = N _{fit} / -	Cumulated Co- ordination Number N _{cum} / -	Mean Square Displacement σ ² / Å ²	R-Factor R' / -
Co _{Td} -O ₁ (CoFe ₂ O ₄ (A-site))	1.91 ± 0.09	4	0.03 ± 0.07 (0.28 in CoFe ₂ O ₄)	0.1 ± 0.3	5.0 ± 1.3	0.011 ± 0.009	0.013
Co _{Oh} -O ₁ (FeCo ₂ O ₄ (B-site))	2.01 ± 0.06	6	0.08 ± 0.05 (0.72 in CoFe ₂ O ₄)	0.5 ± 0.3			
Co-O ₁ (CoO)	2.19 ± 0.06	6	0.73 ± 0.11	4.4 ± 0.7			
Co-Co ₁ (Co)	2.53 ± 0.05	12	0.14 ± 0.07	1.7 ± 0.8	10.5 ± 2.1	0.011 ± 0.002	
Co-Co ₁ (CoO)	3.03 ± 0.02	12	Same as Co-O ₁ (CoO)	8.8 ± 1.3			

Table S4. Co K-Edge FT-EXAFS Magnitude Fitting Values of As-Synthesized Co_{0.60}Fe_{0.40}O_y

Amplitude Reduction Factor $S_0^2 = 0.77 \pm 0.04$ & Energy Shift $\Delta E_0 = 0 \pm 3$ eV							
Scattering Path (Model)	Half Path Length R / Å	Theoretical Co- ordination Number N _{th} / -	Phase Composition Fraction p _{fit} / -	Coordination Number N _{th} · p _{fit} = N _{fit} / -	Cumulated Co- ordination Number N _{cum} / -	Mean Square Displacement σ ² / Å ²	R-Factor R' / -
Co _{Td} -O ₁ (CoFe ₂ O ₄ (A-site))	1.87 ± 0.23	4	0.16 ± 0.08 (0.28 in CoFe ₂ O ₄)	0.6 ± 0.3	5.7 ± 2.7	0.006 ± 0.011	0.035
Co-O ₁ (CoO)	1.96 ± 0.05	6	0.44 ± 0.23	2.6 ± 1.4			
Co _{Oh} -O ₁ (FeCo ₂ O ₄ (B-site))	2.10 ± 0.06	6	0.42 ± 0.17 (0.72 in CoFe ₂ O ₄)	2.5 ± 1.0			
Co _{Oh} -Co _{Oh} ¹ (FeCo ₂ O ₄ (B-site))	2.94 ± 0.07	6	Same as Co _{Oh} -O ₁ (FeCo ₂ O ₄ (B-site))	2.5 ± 1.0	11.9 ± 6	0.010 ± 0.002	
Co-Co ₁ (CoO)	2.98 ± 0.04	12	Same as Co-O ₁ (CoO)	5 ± 3			
Co _{Oh} -Fe _{Td} ¹ (FeCo ₂ O ₄ (B-site))	3.44 ± 0.06	6	Same as Co _{Oh} -O ₁ (FeCo ₂ O ₄ (B-site))	2.5 ± 1.0			
Co _{Td} -Fe _{Oh} ¹ (CoFe ₂ O ₄ (A-site))	3.44 ± 0.07	12	Same as Co _{Td} -O ₁ (CoFe ₂ O ₄ (A-site))	1.9 ± 1.0			
Co _{Td} -O ₂ (CoFe ₂ O ₄ (A-site))	3.46 ± 0.07	12	Same as Co _{Td} -O ₁ (CoFe ₂ O ₄ (A-site))	1.9 ± 1.0	1.9 ± 1.0	0.006 ± 0.011	

Table S5. Co K-Edge FT-EXAFS Magnitude Fitting Values of As-Synthesized Co_{0.30}Fe_{0.70}O_y

Amplitude Reduction Factor $S_0^2 = 0.78 \pm 0.04$ & Energy Shift $\Delta E_0 = 1.7 \pm 1.3$ eV							
Scattering Path (Model)	Half Path Length R / Å	Theoretical Co- ordination Number N _{th} / -	Phase Composition Fraction p _{fit} / -	Coordination Number N _{th} · p _{fit} = N _{fit} / -	Cumulated Co- ordination Number N _{cum} / -	Mean Square Displacement σ ² / Å ²	R-Factor R' / -
Co _{Td} -O ₁ (CoFe ₂ O ₄ (A-site))	1.91 ± 0.02	4	0.28 ± 0.10	1.1 ± 0.4	5.4 ± 1.0	0.005 ± 0.002	0.016
Co _{Oh} -O ₁ (FeCo ₂ O ₄ (B-site))	2.06 ± 0.02	6	0.72 ± 0.10	4.3 ± 0.6			
Co _{Oh} -Co _{Oh} ¹ (FeCo ₂ O ₄ (B-site))	2.95 ± 0.01	6	Same as Co _{Oh} -O ₁ (FeCo ₂ O ₄ (B-site))	4.3 ± 0.6	13.1 ± 2.8 (all M-M)	0.007 ± 0.001	
Co _{Oh} -Fe _{Td} ¹ (FeCo ₂ O ₄ (B-site))	3.45 ± 0.03	6	Same as Co _{Oh} -O ₁ (FeCo ₂ O ₄ (B-site))	4.3 ± 0.6			
Co _{Td} -O ₂ (CoFe ₂ O ₄ (A-site))	3.46 ± 0.03	12	Same as Co _{Td} -O ₁ (CoFe ₂ O ₄ (A-site))	3.4 ± 1.2	7.7 ± 1.8 (all M-O ₂)	0.005 ± 0.002	
Co _{Td} -Fe _{Oh} ¹ (CoFe ₂ O ₄ (A-site))	3.51 ± 0.02	12	Same as Co _{Td} -O ₁ (CoFe ₂ O ₄ (A-site))	3.4 ± 1.2	Part of all M-M	0.007 ± 0.001	
Co _{Td} -Co _{Td} ¹ (CoFe ₂ O ₄ (A-site))	3.62 ± 0.10	4	Same as Co _{Td} -O ₁ (CoFe ₂ O ₄ (A-site))	1.1 ± 0.4			
Co _{Oh} -O ₂ (FeCo ₂ O ₄ (B-site))	3.62 ± 0.03	6	Same as Co _{Oh} -O ₁ (FeFe ₂ O ₄ (B-site))	4.3 ± 0.6	Part of all M-O ₂	0.005 ± 0.002	

Table S6. Fe K-Edge FT-EXAFS Magnitude Fitting Values of As-Synthesized $\text{Co}_{0.80}\text{Fe}_{0.20}\text{O}_y$

Amplitude Reduction Factor $S_0^2 = 0.66 \pm 0.21$ & Energy Shift $\Delta E_0 = 4.8 \pm 2.3$ eV							
Scattering Path (Model)	Half Path Length R / Å	Theoretical Co- ordination Number N_{th} / -	Phase Composition Fraction p_{fit} / -	Coordination Number $N_{th} \cdot p_{fit} = N_{fit}$ / -	Cumulated Co- ordination Number N_{cum} / -	Mean Square Displacement σ^2 / Å ²	R-Factor R' / -
Fe _{Td} -O ₁ (FeCo ₂ O ₄ (A-site))	1.91 ± 0.05	4	0.17 ± 0.09 (0.4 in CoFe ₂ O ₄)	0.7 ± 0.4	5.7 ± 2.5	0.006 ± 0.004	0.022
Fe-O ₁ (FeO)	1.97 ± 0.03	6	0.57 ± 0.21	3.4 ± 1.3			
Fe _{Oh} -O ₁ (CoFe ₂ O ₄ (B-site))	2.08 ± 0.05	6	0.26 ± 0.13 (0.6 in CoFe ₂ O ₄)	1.6 ± 0.8			
Fe _{Oh} -Fe _{Oh,1} (CoFe ₂ O ₄ (B-site))	2.94 ± 0.05	6	Same as Fe _{Oh} -O ₁ (CoFe ₂ O ₄ (B-site))	1.6 ± 0.8	12.1 ± 5.2	0.001 ± 0.002	
Fe-Fe ₁ (FeO)	3.03 ± 0.02	12	Same as Fe-O ₁ (FeO)	6.8 ± 2.5			
Fe _{Td} -Co _{Oh,1} (FeCo ₂ O ₄ (A-site))	3.43 ± 0.04	12	Same as Fe _{Td} -O ₁ (FeCo ₂ O ₄ (A-site))	2.1 ± 1.1			
Fe _{Oh} -Co _{Td,1} (CoFe ₂ O ₄ (B-site))	3.43 ± 0.04	6	Same as Fe _{Oh} -O ₁ (CoFe ₂ O ₄ (B-site))	1.6 ± 0.8	2.1 ± 1.1	0.006 ± 0.004	
Fe _{Td} -O ₂ (FeCo ₂ O ₄ (A-site))	3.52 ± 0.05	12	Same as Fe _{Td} -O ₁ (FeCo ₂ O ₄ (A-site))	2.1 ± 1.1			

Table S7. Fe K-Edge FT-EXAFS Magnitude Fitting Values of As-Synthesized $\text{Co}_{0.60}\text{Fe}_{0.40}\text{O}_y$

Amplitude Reduction Factor $S_0^2 = 0.65 \pm 0.20$ & Energy Shift $\Delta E_0 = 5.0 \pm 1.8$ eV							
Scattering Path (Model)	Half Path Length R / Å	Theoretical Co- ordination Number N_{th} / -	Phase Composition Fraction p_{fit} / -	Coordination Number $N_{th} \cdot p_{fit} = N_{fit}$ / -	Cumulated Co- ordination Number N_{cum} / -	Mean Square Displacement σ^2 / Å ²	R-Factor R' / -
Fe _{Td} -O ₁ (FeCo ₂ O ₄ (A-site))	1.87 ± 0.05	4	0.26 ± 0.06 (0.4 in CoFe ₂ O ₄)	1.1 ± 0.2	5.6 ± 1.5	0.001 ± 0.004	0.011
Fe-O ₁ (FeO)	1.94 ± 0.02	6	0.35 ± 0.14	2.1 ± 0.8			
Fe _{Oh} -O ₁ (CoFe ₂ O ₄ (B-site))	2.05 ± 0.04	6	0.40 ± 0.09 (0.6 in CoFe ₂ O ₄)	2.4 ± 0.5			
Fe _{Oh} -Fe _{Oh,1} (CoFe ₂ O ₄ (B-site))	2.94 ± 0.02	6	Same as Fe _{Oh} -O ₁ (CoFe ₂ O ₄ (B-site))	2.4 ± 0.5	12.1 ± 3.4 (all M-M)	0.008 ± 0.001	
Fe-Fe ₁ (FeO)	3.02 ± 0.02	12	Same as Fe-O ₁ (FeO)	4.1 ± 1.7			
Fe _{Td} -O ₂ (FeCo ₂ O ₄ (A-site))	3.46 ± 0.02	12	Same as Fe _{Td} -O ₁ (FeCo ₂ O ₄ (A-site))	3.2 ± 0.7	3.2 ± 0.7	0.001 ± 0.004	
Fe _{Td} -Co _{Oh,1} (FeCo ₂ O ₄ (A-site))	3.46 ± 0.05	12	Same as Fe _{Td} -O ₁ (FeCo ₂ O ₄ (A-site))	3.2 ± 0.7	Part of all M-M	0.008 ± 0.001	
Fe _{Oh} -Co _{Td,1} (CoFe ₂ O ₄ (B-site))	3.50 ± 0.02	6	Same as Fe _{Oh} -O ₁ (CoFe ₂ O ₄ (B-site))	2.4 ± 0.5			

Table S8. Fe K-Edge FT-EXAFS Magnitude Fitting Values of As-Synthesized $\text{Co}_{0.30}\text{Fe}_{0.70}\text{O}_y$

Amplitude Reduction Factor $S_o^2 = 0.66 \pm 0.22$ & Energy Shift $\Delta E_0 = 5.6 \pm 1.4$ eV							
Scattering Path (Model)	Half Path Length R / Å	Theoretical Co- ordination Number N_{th} / -	Phase Composition Fraction p_{fit} / -	Coordination Number $N_{th} \cdot p_{fit} = N_{fit}$ / -	Cumulated Co- ordination Number N_{cum} / -	Mean Square Displacement σ^2 / Å ²	R-Factor R' / -
$Fe_{Td}\text{-}O_1$ ($FeCo_2O_4$ (A-site))	1.89 ± 0.07	4	0.40 ± 0.10	1.6 ± 0.4	5.2 ± 1.0	0.005 ± 0.005	0.016
$Fe_{Oh}\text{-}O_1$ ($CoFe_2O_4$ (B-site))	2.01 ± 0.02	6	0.60 ± 0.10	3.6 ± 0.6			
$Fe_{Oh}\text{-}Fe_{Oh,1}$ ($CoFe_2O_4$ (B-site))	2.99 ± 0.02	6	Same as $Fe_{Oh}\text{-}O_1$ ($CoFe_2O_4$ (B-site))	3.6 ± 0.6	13.7 ± 2.8 (all M-M)	0.006 ± 0.002	
$Fe_{Oh}\text{-}Co_{Td,1}$ ($CoFe_2O_4$ (B-site))	3.44 ± 0.03	6	Same as $Fe_{Oh}\text{-}O_1$ ($CoFe_2O_4$ (B-site))	3.6 ± 0.6			
$Fe_{Td}\text{-}O_2$ ($FeCo_2O_4$ (A-site))	3.46 ± 0.03	12	Same as $Fe_{Td}\text{-}O_1$ ($FeCo_2O_4$ (A-site))	4.9 ± 1.2	8.5 ± 1.8 (all M-O ₂)	0.005 ± 0.005	
$Fe_{Td}\text{-}Co_{Oh,1}$ ($FeCo_2O_4$ (A-site))	3.50 ± 0.02	12	Same as $Fe_{Td}\text{-}O_1$ ($FeCo_2O_4$ (A-site))	4.9 ± 1.2	Part of all M-M	0.006 ± 0.002	
$Fe_{Oh}\text{-}O_2$ ($CoFe_2O_4$ (B-site))	3.63 ± 0.03	6	Same as $Fe_{Oh}\text{-}O_1$ ($CoFe_2O_4$ (B-site))	3.6 ± 0.6	Part of all M-O ₂	0.005 ± 0.005	
$Fe_{Td}\text{-}Fe_{Td,1}$ ($FeCo_2O_4$ (A-site))	3.64 ± 0.09	4	Same as $Fe_{Td}\text{-}O_1$ ($FeCo_2O_4$ (A-site))	1.6 ± 0.4	Part of all M-M	0.006 ± 0.002	

References

- (1) Heel, A.; Holtappels, P.; Hug, P.; Graule, T. Flame spray synthesis of nanoscale $\text{La}_{0.6}\text{Sr}_{0.4}\text{Co}_{0.2}\text{Fe}_{0.8}\text{O}_{3-\delta}$ and $\text{Ba}_{0.5}\text{Sr}_{0.5}\text{Co}_{0.8}\text{Fe}_{0.2}\text{O}_{3-\delta}$ as cathode materials for intermediate temperature solid oxide fuel cells. *Fuel Cells* **2010**, *10* (3), 419-432. DOI: 10.1002/fuce.200900093
- (2) Aegerter, D.; Borlaf, M.; Fabbri, E.; Clark, A. H.; Nachtegaal, M.; Graule, T.; Schmidt, T. J. Tuning the Co oxidation state in $\text{Ba}_{0.5}\text{Sr}_{0.5}\text{Co}_{0.8}\text{Fe}_{0.2}\text{O}_{3-\delta}$ by flame spray synthesis towards high oxygen evolution reaction activity. *Catalysts* **2020**, *10* (9), 984. DOI: 10.3390/catal10090984
- (3) Yang, J.; Liu, H. W.; Martens, W. N.; Frost, R. L. Synthesis and characterization of cobalt hydroxide, cobalt oxyhydroxide, and cobalt oxide nanodiscs. *J. Phys. Chem. C* **2010**, *114* (1), 111-119. DOI: 10.1021/jp908548f
- (4) Seo, B.; Sa, Y. J.; Woo, J.; Kwon, K.; Park, J.; Shin, T. J.; Jeong, H. Y.; Joo, S. H. Size-dependent activity trends combined with in situ X-ray absorption spectroscopy reveal insights into cobalt oxide/carbon nanotube-catalyzed bifunctional oxygen electrocatalysis. *ACS Catal.* **2016**, *6* (7), 4347-4355. DOI: 10.1021/acscatal.6b00553
- (5) Khort, A. R., S.; Loginov, P. Solution combustion synthesis of single-phase bimetallic nanomaterials. *Nano-Struct. Nano-Objects* **2021**, *26*, 100727. DOI: 10.1016/j.nanoso.2021.100727
- (6) Sasaki, S.; Fujino, K.; Takeuchi, Y. X-ray determination of electron-density distributions in oxides, MgO, MnO, CoO, and NiO, and atomic scattering factors of their constituent atoms. *Proc. Jpn. Acad., Ser. B* **1979**, *55* (2), 43-48. DOI: DOI 10.2183/pjab.55.43
- (7) Hong, K. H.; Solana-Madruga, E.; Coduri, M.; Attfield, J. P. Complex cation and spin orders in the high-pressure ferrite CoFe_3O_5 . *Inorg. Chem.* **2018**, *57* (22), 14347-14352. DOI: 10.1021/acs.inorgchem.8b02458
- (8) Dojcinovic, M. P.; Vasiljevic, Z. Z.; Pavlovic, V. P.; Barisic, D.; Pajic, D.; Tadic, N. B.; Nikolic, M. V. Mixed Mg-Co spinel ferrites: Structure, morphology, magnetic and photocatalytic properties. *J. Alloys Compd.* **2021**, *855*, 157429. DOI: 10.1016/j.jallcom.2020.157429
- (9) Ferreira, T. A. S.; Waerenborgh, J. C.; Mendonca, M. H. R. M.; Nunes, M. R.; Costa, F. M. Structural and morphological characterization of FeCo_2O_4 and CoFe_2O_4 spinels prepared by a coprecipitation method. *Solid State Sci.* **2003**, *5* (2), 383-392. DOI: 10.1016/S1293-2558(03)00011-6
- (10) Picard, J. P.; Baud, G.; Besse, J. P.; Chevalier, R. Crystal-growth and structural study of Co_3O_4 . *J. Less-Common Met.* **1980**, *75* (1), 99-104. DOI: 10.1016/0022-5088(80)90373-2
- (11) Beauregard, P. Behavior of particle size distributions, means and BET values in ideal and non-ideal morphology systems in a TEM. *Microsc. Today* **2004**, *12* (1), 30-33. DOI: 10.1017/S1551929500051798
- (12) Handbook of Chemistry and Physics 102nd edition, CRC Press, Taylor & Francis Group. Available online: https://hbcpc.chemnetbase.com/faces/documents/04_02/04_02_0001.xhtml (accessed on 17.10.2022).
- (13) Muller, O.; Nachtegaal, M.; Just, J.; Lutzenkirchen-Hecht, D.; Frahm, R. Quick-EXAFS setup at the SuperXAS beamline for in situ X-ray absorption spectroscopy with 10 ms time resolution. *J. Synchrotron Rad.* **2016**, *23*, 260-266. DOI: 10.1107/S1600577515018007
- (14) Clark, A. H.; Imbao, J.; Frahm, R.; Nachtegaal, M. ProQEXAFS: A highly optimized parallelized rapid processing software for QEXAFS data. *J. Synchrotron Rad.* **2020**, *27*, 551-557. DOI: 10.1107/S1600577519017053
- (15) Ravel, B.; Newville, M. ATHENA, ARTEMIS, HEPHAESTUS: Data analysis for X-ray absorption spectroscopy using IFEFFIT. *J. Synchrotron Rad.* **2005**, *12*, 537-541. DOI: 10.1107/S0909049505012719
- (16) Natta, G.; Strada, M. Ossidi ed idrossidi del cobalto. *Gazz. Chim. Ital.* **1928**, *58*, 419-433.
- (17) Delaplane, R. G.; Ibers, J. A.; Ferraro, J. R.; Rush, J. J. Diffraction and spectroscopic studies of the cobaltic acid system $\text{HCoO}_2\text{-DCoO}_2$. *J. Chem. Phys.* **1969**, *50* (5), 1920-1927. DOI: 10.1063/1.1671307
- (18) Orlova, I. G.; Eliseev, A. A.; Chuprikov, G. E.; Rukk, F. Tb-Fe system. *Zh. Neorg. Khim.* **1977**, *22* (9), 2557-2562.

- (19) Taylor, D. Thermal-expansion data. I: Binary oxides with the sodium-chloride and wurtzite structures, MO. *Trans. J. Br. Ceram. Soc.* **1984**, 83 (1), 5-9.
- (20) Piamonteze, C.; Flechsig, U.; Rusponi, S.; Dreiser, J.; Heidler, J.; Schmidt, M.; Wetter, R.; Calvi, M.; Schmidt, T.; Pruchova, H.; Krempasky, J.; Quitmann, C.; Brune, H.; Nolting, F. X-Treme beamline at SLS: X-ray magnetic circular and linear dichroism at high field and low temperature. *J. Synchrotron Rad.* **2012**, 19, 661-674. DOI: 10.1107/S0909049512027847
- (21) Bergmann, A.; Jones, T. E.; Moreno, E. M.; Teschner, D.; Chervnev, P.; Gliech, M.; Reier, T.; Dau, H.; Strasser, P. Unified structural motifs of the catalytically active state of Co(oxyhydr)oxides during the electrochemical oxygen evolution reaction. *Nat. Catal.* **2018**, 1 (9), 711-719. DOI: 10.1038/s41929-018-0141-2
- (22) Regan, T. J.; Ohldag, H.; Stamm, C.; Nolting, F.; Luning, J.; Stohr, J.; White, R. L. Chemical effects at metal/oxide interfaces studied by X-ray-absorption spectroscopy. *Phys. Rev. B* **2001**, 64 (21), 214422. DOI: 10.1103/PhysRevB.64.214422
- (23) Morales, F.; de Groot, F. M. F.; Glatzel, P.; Kleimenov, E.; Bluhm, H.; Havecker, M.; Knop-Gericke, A.; Weckhuysen, B. M. In situ X-ray absorption of Co/Mn/TiO₂ catalysts for Fischer-Tropsch synthesis. *J. Phys. Chem. B* **2004**, 108 (41), 16201-16207. DOI: DOI 10.1021/jp0403846
- (24) Mefford, J. T.; Akbashev, A. R.; Kang, M. K.; Bentley, C. L.; Gent, W. E.; Deng, H. T. D.; Alsem, D. H.; Yu, Y. S.; Salmon, N. J.; Shapiro, D. A.; Unwin, P. R.; Chueh, W. C. Correlative operando microscopy of oxygen evolution electrocatalysts. *Nature* **2021**, 593 (7857), 67-73. DOI: 10.1038/s41586-021-03454-x
- (25) van Schooneveld, M. M.; Kurian, R.; Juhin, A.; Zhou, K.; Schlappa, J.; Strocov, V. N.; Schmitt, T.; de Groot, F. M. F. Electronic structure of CoO nanocrystals and a single crystal probed by resonant X-ray emission spectroscopy. *J. Phys. Chem. C* **2012**, 116 (29), 15218-15230. DOI: 10.1021/jp302847h
- (26) Liang, Y. Y.; Li, Y. G.; Wang, H. L.; Zhou, J. G.; Wang, J.; Regier, T.; Dai, H. J. Co₃O₄ nanocrystals on graphene as a synergistic catalyst for oxygen reduction reaction. *Nat. Mater.* **2011**, 10 (10), 780-786. DOI: 10.1038/Nmat3087
- (27) Wang, R. P.; Huang, M. J.; Hariki, A.; Okamoto, J.; Huang, H. Y.; Singh, A.; Huang, D. J.; Nagel, P.; Schuppler, S.; Haarmann, T.; Liu, B. Y.; de Groot, F. M. F. Analyzing the local electronic structure of Co₃O₄ using 2p3d resonant inelastic X-ray scattering. *J. Phys. Chem. C* **2022**, 126 (20), 8752-8759. DOI: 10.1021/acs.jpcc.2c01521
- (28) Miedema, P. S.; de Groot, F. M. F. The iron L edges: Fe 2p X-ray absorption and electron energy loss spectroscopy. *J. Electron. Spectrosc. Relat. Phenom.* **2013**, 187, 32-48. DOI: 10.1016/j.elspec.2013.03.005
- (29) Suturin, S. M.; Korovin, A. M.; Gastev, S. V.; Volkov, M. P.; Sitnikova, A. A.; Kirilenko, D. A.; Tabuchi, M.; Sokolov, N. S. Tunable polymorphism of epitaxial iron oxides in the four-in-one ferroic-on-GaN system with magnetically ordered α -, γ -, ϵ -Fe₂O₃, and Fe₃O₄ layers. *Phys. Rev. Materials* **2018**, 2 (7), 073403. DOI: 10.1103/PhysRevMaterials.2.073403
- (30) Chen, C. L.; Dong, C. L.; Rao, S. M.; Chern, G.; Chen, M. C.; Wu, M. K.; Chang, C. L. Investigation of the valence states of Fe and Co in Fe_{1-x}Co_xO_y (0 < x < 1) thin films by X-ray absorption spectroscopy. *J. Phys.: Condens. Matter* **2008**, 20 (25), 255236. DOI: 10.1088/0953-8984/20/25/255236
- (31) Zhou, S. Q.; Potzger, K.; Xu, Q. Y.; Kuepper, K.; Talut, G.; Marko, D.; Mucklich, A.; Helm, M.; Fassbender, J.; Arenholz, E.; Schmidt, H. Spinel ferrite nanocrystals embedded inside ZnO: Magnetic, electronic, and magnetotransport properties. *Phys. Rev. B* **2009**, 80 (9), 094409. DOI: 10.1103/PhysRevB.80.094409
- (32) Wang, J. W.; Zhang, H.; Lv, X. X.; Nie, K. Q.; Gao, X. J.; Zhong, J.; Sun, X. H. Self-supported ultrathin mesoporous CoFe₂O₄/CoO nanosheet arrays assembled from nanowires with enhanced lithium storage performance. *J. Mater. Sci.* **2016**, 51 (14), 6590-6599. DOI: 10.1007/s10853-016-9902-y
- (33) Ohtsuki, T.; Chainani, A.; Eguchi, R.; Matsunami, M.; Takata, Y.; Taguchi, M.; Nishino, Y.; Tamasaku, K.; Yabashi, M.; Ishikawa, T.; Oura, M.; Senba, Y.; Ohashi, H.; Shin, S. Role of Ti 3d carriers in mediating the ferromagnetism of Co : TiO₂ anatase thin films. *Phys. Rev. Lett.* **2011**, 106 (4), 047602. DOI: 10.1103/PhysRevLett.106.047602
- (34) Liang, H. W.; Kroll, T.; Nordlund, D.; Weng, T.-C.; Sokaras, D.; Pierpont, C. G.; Gaffney, K. J. Charge and spin-state characterization of cobalt bis(o-dioxolene) valence tautomers using Co K β X-ray emission and L-edge X-ray absorption spectroscopies. *Inorg. Chem.* **2017**, 56 (2), 737-747. DOI: 10.1021/acs.inorgchem.6b01666

- (35) Hibberd, A. M.; Doan, H. Q.; Glass, E. N.; de Groot, F. M. F.; Hill, C. L.; Cuk, T. Co polyoxonmetalates and a Co_3O_4 thin film investigated by L-edge X-ray absorption spectroscopy. *J. Phys. Chem. C* **2015**, *119* (8), 4173-4179. DOI: 10.1021/jp5124037
- (36) Nappini, S.; Magnano, E.; Bondino, F.; Pis, I.; Barla, A.; Fantechi, E.; Pineider, F.; Sangregorio, C.; Vaccari, L.; Venturelli, L.; Baglioni, P. Surface charge and coating of CoFe_2O_4 nanoparticles: Evidence of preserved magnetic and electronic properties. *J. Phys. Chem. C* **2015**, *119* (45), 25529-25541. DOI: 10.1021/acs.jpcc.5b04910
- (37) Schmidt, T. J.; Gasteiger, H. A.; Stab, G. D.; Urban, P. M.; Kolb, D. M.; Behm, R. J. Characterization of high-surface area electrocatalysts using a rotating disk electrode configuration. *J. Electrochem. Soc.* **1998**, *145* (7), 2354-2358. DOI: Doi 10.1149/1.1838642
- (38) Sheng, W. C.; Gasteiger, H. A.; Shao-Horn, Y. Hydrogen oxidation and evolution reaction kinetics on platinum: Acid vs alkaline electrolytes. *J. Electrochem. Soc.* **2010**, *157* (11), B1529-B1536. DOI: 10.1149/1.3483106
- (39) Rheinlander, P. J.; Henning, S.; Herranz, J.; Gasteiger, H. A. Comparing hydrogen oxidation and evolution reaction kinetics on polycrystalline platinum in 0.1 M and 1 M KOH. *ECS Trans.* **2013**, *50* (2), 2163-2174. DOI: 10.1149/05002.2163ecst
- (40) Rheinlander, P. J.; Herranz, J.; Durst, J.; Gasteiger, H. A. Kinetics of the hydrogen oxidation/evolution reaction on polycrystalline platinum in alkaline electrolyte reaction order with respect to hydrogen pressure. *J. Electrochem. Soc.* **2014**, *161* (14), F1448-F1457. DOI: 10.1149/2.0501414jes
- (41) Suntivich, J.; Gasteiger, H. A.; Yabuuchi, N.; Shao-Horn, Y. Electrocatalytic measurement methodology of oxide catalysts using a thin-film rotating disk electrode. *J. Electrochem. Soc.* **2010**, *157* (8), B1263-B1268. DOI: 10.1149/1.3456630
- (42) Binninger, T.; Fabbri, E.; Patru, A.; Garganourakis, M.; Han, J.; Abbott, D. F.; Sereda, O.; Kotz, R.; Menzel, A.; Nachtegaal, M.; Schmidt, T. J. Electrochemical flow-cell setup for in situ X-ray Investigations I. Cell for SAXS and XAS at synchrotron facilities. *J. Electrochem. Soc.* **2016**, *163* (10), H906-H912. DOI: 10.1149/2.0201610jes
- (43) Povia, M.; Herranz, J.; Binninger, T.; Nachtegaal, M.; Diaz, A.; Kohlbrecher, J.; Abbott, D. F.; Kim, B. J.; Schmidt, T. J. Combining SAXS and XAS to study the operando degradation of carbon-supported Pt-nanoparticle fuel cell catalysts. *ACS Catal.* **2018**, *8* (8), 7000-7015. DOI: 10.1021/acscatal.8b01321
- (44) Diklic, N.; Clark, A. H.; Herranz, J.; Diercks, J. S.; Aegerter, D.; Nachtegaal, M.; Beard, A.; Schmidt, T. J. Potential pitfalls in the operando XAS study of oxygen evolution electrocatalysts. *ACS Energy Lett.* **2022**, *7* (5), 1735-1740. DOI: 10.1021/acsenenergylett.2c00727
- (45) Straumanis, M. E. Neubestimmung der Gitterparameter, Dichten und thermischen Ausdehnungskoeffizienten von Silber und Gold, und Vollkommenheit der Struktur. *Monatsh. Chem.* **1971**, *102* (5), 1377-1386. DOI: 10.1007/BF00917194
- (46) Fabbri, E.; Nachtegaal, M.; Binninger, T.; Cheng, X.; Kim, B. J.; Durst, J.; Bozza, F.; Graule, T.; Schaublin, R.; Wiles, L.; Pertoso, M.; Danilovic, N.; Ayers, K. E.; Schmidt, T. J. Dynamic surface self-reconstruction is the key of highly active perovskite nano-electrocatalysts for water splitting. *Nat. Mater.* **2017**, *16* (9), 925-932. DOI: 10.1038/Nmat4938
- (47) Calvillo, L.; Carraro, F.; Vozniuk, O.; Celorrio, V.; Nodari, L.; Russell, A. E.; Debellis, D.; Fermin, D.; Cavani, F.; Agnoli, S.; Granozzi, G. Insights into the durability of Co-Fe spinel oxygen evolution electrocatalysts via operando studies of the catalyst structure. *J. Mater. Chem. A* **2018**, *6* (16), 7034-7041. DOI: 10.1039/c7ta10892c
- (48) Bergmann, A.; Martinez-Moreno, E.; Teschner, D.; Chernev, P.; Gliech, M.; de Araujo, J. F.; Reier, T.; Dau, H.; Strasser, P. Reversible amorphization and the catalytically active state of crystalline Co_3O_4 during oxygen evolution. *Nat. Commun.* **2015**, *6*, 8625. DOI: 10.1038/ncomms9625
- (49) Saddeler, S.; Bendt, G.; Salamon, S.; Haase, F. T.; Landers, J.; Timoshenko, J.; Rettenmaier, C.; Jeon, H. S.; Bergmann, A.; Wende, H.; Cuenya, B. R.; Schulz, S. Influence of the cobalt content in cobalt iron oxides on the electrocatalytic OER activity. *J. Mater. Chem. A* **2021**, *9* (45), 25381-25390. DOI: 10.1039/d1ta06568h
- (50) Grimaud, A.; Carlton, C. E.; Risch, M.; Hong, W. T.; May, K. J.; Shao-Horn, Y. Oxygen evolution activity and stability of $\text{Ba}_6\text{Mn}_5\text{O}_{16}$, $\text{Sr}_4\text{Mn}_2\text{CoO}_9$, and $\text{Sr}_6\text{Co}_5\text{O}_{15}$: The influence of transition metal coordination. *J. Phys. Chem. C* **2013**, *117* (49), 25926-25932. DOI: 10.1021/jp408585z

- (51) Altin, S.; Bayri, A.; Demirel, S.; Oz, E.; Altin, E.; Avci, S. Structural, magnetic, electrical, and electrochemical properties of Sr-Co-Ru-O: A hybrid-capacitor application. *J. Am. Ceram. Soc.* **2018**, *101* (10), 4572-4581. DOI: 10.1111/jace.15698
- (52) Xiang, W.; Yang, N.; Li, X.; Linnemann, J.; Hagemann, U.; Ruediger, O.; Heidelmann, M.; Falk, T.; Aramini, M.; DeBeer, S.; Muhler, M.; Tschulik, K.; Li, T. 3D atomic-scale imaging of mixed Co-Fe spinel oxide nanoparticles during oxygen evolution reaction. *Nat. Commun.* **2022**, *13* (1), 179. DOI: 10.1038/s41467-021-27788-2
- (53) Campos-Roldán, C. A.; González-Huerta, R. G.; Alonso-Vante, N. Experimental protocol for HOR and ORR in alkaline electrochemical measurements. *J. Electrochem. Soc.* **2018**, *165* (15), J3001. DOI: 10.1149/2.0011815jes
- (54) Weckhuysen, B. M. Snapshots of a working catalyst: Possibilities and limitations of in situ spectroscopy in the field of heterogeneous catalysis. *Chem. Commun.* **2002**, (2), 97-110. DOI: DOI 10.1039/b107686h
- (55) Banares, M. A.; Wachs, I. E. Molecular structures of supported metal oxide catalysts under different environments. *J. Raman Spectrosc.* **2002**, *33* (5), 359-380. DOI: 10.1002/jrs.866
- (56) Cortez, G. G.; Banares, M. A. A Raman spectroscopy study of alumina-supported vanadium oxide catalyst during propane oxidative dehydrogenation with online activity measurement. *J. Catal.* **2002**, *209* (1), 197-201. DOI: 10.1006/jcat.2002.3600
- (57) Guerrero-Perez, M. O.; Banares, M. A. Operando raman study of alumina-supported Sb-V-O catalyst during propane ammoxidation to acrylonitrile with on-line activity measurement. *Chem. Commun.* **2002**, (12), 1292-1293. DOI: 10.1039/b202556f
- (58) Banares, M. A.; Guerrero-Perez, M. O.; Fierro, J. L. G.; Cortez, G. G. Raman spectroscopy during catalytic operations with on-line activity measurement (operando spectroscopy): A method for understanding the active centres of cations supported on porous materials. *J. Mater. Chem.* **2002**, *12* (11), 3337-3342. DOI: 10.1039/b204494c
- (59) Burke, M. S.; Kast, M. G.; Trotochaud, L.; Smith, A. M.; Boettcher, S. W. Cobalt-iron (oxy)hydroxide oxygen evolution electrocatalysts: The role of structure and composition on activity, stability, and mechanism. *J. Am. Chem. Soc.* **2015**, *137* (10), 3638-3648. DOI: 10.1021/jacs.5b00281
- (60) Cheng, X.; Kim, B. J.; Fabbri, E.; Schmidt, T. J. Co/Fe oxyhydroxides supported on perovskite oxides as oxygen evolution reaction catalyst systems. *ACS Appl. Mater. Interfaces* **2019**, *11* (38), 34787-34795. DOI: 10.1021/acsami.9b04456
- (61) Shen, J. Q.; Liao, P. Q.; Zhou, D. D.; He, C. T.; Wu, J. X.; Zhang, W. X.; Zhang, J. P.; Chen, X. M. Modular and stepwise synthesis of a hybrid metal-organic framework for efficient electrocatalytic oxygen evolution. *J. Am. Chem. Soc.* **2017**, *139* (5), 1778-1781. DOI: 10.1021/jacs.6b12353
- (62) Li, F. L.; Wang, P. T.; Huang, X. Q.; Young, D. J.; Wang, H. F.; Braunstein, P.; Lang, J. P. Large-scale, bottom-up synthesis of binary metal-organic framework nanosheets for efficient water oxidation. *Angew. Chem. Int. Ed.* **2019**, *58* (21), 7051-7056. DOI: 10.1002/anie.201902588
- (63) Li, F.; Li, J. X.; Zhou, L. H.; Dai, S. Enhanced OER performance of composite Co-Fe-based MOF catalysts via a one-pot ultrasonic-assisted synthetic approach. *Sustain. Energy Fuels* **2021**, *5* (4), 1095-1102. DOI: 10.1039/d0se01750g
- (64) Nakajima, R.; Stohr, J.; Idzerda, Y. U. Electron-yield saturation effects in L-edge X-ray magnetic circular dichroism spectra of Fe, Co, and Ni. *Phys. Rev. B* **1999**, *59* (9), 6421-6429. DOI: 10.1103/PhysRevB.59.6421
- (65) Frazer, B. H.; Gilbert, B.; Sonderegger, B. R.; De Stasio, G. The probing depth of total electron yield in the sub-keV range: TEY-XAS and X-PEEM. *Surf. Sci.* **2003**, *537* (1-3), 161-167. DOI: 10.1016/S0039-6028(03)00613-7
- (66) Akgul, G.; Aksoy, F.; Bozduman, A.; Ozkendir, O. M.; Ufuktepe, Y.; Luning, J. Study of the L_{2,3} edges of 3d transition metals by X-ray absorption spectroscopy. *Thin Solid Films* **2008**, *517* (2), 1000-1004. DOI: 10.1016/j.tsf.2008.08.173
- (67) Ufuktepe, Y.; Akgul, G.; Luning, J. X-Ray photoabsorption and total electron yield of Fe thin films at the L_{2,3} edge. *J. Alloys Compd.* **2005**, *401* (1-2), 193-196. DOI: 10.1016/j.jallcom.2005.02.056
- (68) Martens, G.; Rabe, P.; Tolkiehn, G.; Werner, A. EXAFS in photoelectron yield spectra at K edges of Cu, Ni, and Ge. *Phys. Stat. Sol. (a)* **1979**, *55* (1), 105-108. DOI: 10.1002/pssa.2210550110

- (69) Jones, R. G.; Woodruff, D. P. Sampling depths in total yield and reflectivity SEXAFS studies in the soft X-ray region. *Surf. Sci.* **1982**, *114* (1), 38-46. DOI: 10.1016/0039-6028(82)90454-X
- (70) Erbil, A.; Cargill Iii, G. S.; Frahm, R.; Boehme, R. F. Total-electron-yield current measurements for near-surface extended X-ray-absorption fine structure. *Phys. Rev. B* **1988**, *37* (5), 2450-2464. DOI: 10.1103/PhysRevB.37.2450
- (71) Abbate, M.; Goedkoop, J. B.; de Groot, F. M. F.; Grioni, M.; Fuggle, J. C.; Hofmann, S.; Petersen, H.; Sacchi, M. Probing depth of soft X-ray absorption spectroscopy measured in total-electron-yield mode. *Surf. Interface Anal.* **1992**, *18* (1), 65-69. DOI: 10.1002/sia.740180111
- (72) Schroeder, S. L. M.; Moggridge, G. D.; Ormerod, R. M.; Rayment, T.; Lambert, R. M. What determines the probing depth of electron yield XAS? *Surf. Sci.* **1995**, *324* (2), L371-L377. DOI: 10.1016/0039-6028(94)00779-9
- (73) Kasrai, M.; Lennard, W. N.; Brunner, R. W.; Bancroft, G. M.; Bardwell, J. A.; Tan, K. H. Sampling depth of total electron and fluorescence measurements in Si L- and K-edge absorption spectroscopy. *Appl. Surf. Sci.* **1996**, *99* (4), 303-312. DOI: 10.1016/0169-4332(96)00454-0
- (74) Jauch, W.; Reehuis, M.; Bleif, H. J.; Kubanek, F.; Pattison, R. Crystallographic symmetry and magnetic structure of CoO. *Phys. Rev. B* **2001**, *64* (5). DOI: DOI 10.1103/PhysRevB.64.052102
- (75) Wdowik, U. D.; Parlinski, K. Lattice dynamics of CoO from first principles. *Phys. Rev. B* **2007**, *75* (10). DOI: 10.1103/PhysRevB.75.104306
- (76) Negi, D. S.; Datta, R.; Rusz, J. Defect driven spin state transition and the existence of half-metallicity in CoO. *J. Phys.: Condens. Matter* **2019**, *31* (11). DOI: 10.1088/1361-648X/aafd11
- (77) Hossain, A.; Sarker, M. S. I.; Khan, M. K. R.; Rahman, M. M. Spin effect on electronic, magnetic and optical properties of spinel CoFe₂O₄: A DFT study. *Mater. Sci. Eng., B* **2020**, *253*, 114496. DOI: 10.1016/j.mseb.2020.114496
- (78) Brabers, V. A. M.; Broemme, A. D. D. Low-spin-high-spin transition in the Co₃O₄ spinel. *J. Magn. Magn. Mater.* **1992**, *104-107*, 405-406. DOI: 10.1016/0304-8853(92)90853-G
- (79) Strobel, R.; Pratsinis, S. E. Effect of solvent composition on oxide morphology during flame spray pyrolysis of metal nitrates. *Phys. Chem. Chem. Phys.* **2011**, *13* (20), 9246-9252. DOI: 10.1039/c0cp01416h
- (80) Pozio, A.; Bozza, F.; Lisi, N.; Chierchia, R.; Migliorini, F.; Donde, R.; De Iuliis, S. Cobalt oxide synthesis via flame spray pyrolysis as anode electrocatalyst for alkaline membrane water electrolyzer. *Materials* **2022**, *15* (13), 4626. DOI: 10.3390/ma15134626
- (81) Belles, L.; Moularas, C.; Smykala, S.; Deligiannakis, Y. Flame spray pyrolysis Co₃O₄/CoO as highly-efficient nanocatalyst for oxygen reduction reaction. *Nanomaterials* **2021**, *11* (4), 925. DOI: 10.3390/nano11040925
- (82) Grass, R. N.; Athanassiou, E. K.; Stark, W. J. Covalently functionalized cobalt nanoparticles as a platform for magnetic separations in organic synthesis. *Angew. Chem. Int. Ed.* **2007**, *46* (26), 4909-4912. DOI: 10.1002/anie.200700613
- (83) Pratsinis, S. E. Aerosol-based technologies in nanoscale manufacturing: From functional materials to devices through core chemical engineering. *AIChE J.* **2010**, *56* (12), 3028-3035. DOI: 10.1002/aic.12478
- (84) Grohn, A. J.; Pratsinis, S. E.; Sanchez-Ferrer, A.; Mezzenga, R.; Wegner, K. Scale-up of nanoparticle synthesis by flame spray pyrolysis: The high-temperature particle residence time. *Ind. Eng. Chem. Res.* **2014**, *53* (26), 10734-10742. DOI: 10.1021/ie501709s
- (85) Bartunek, V.; Huber, S.; Sedmidubsky, D.; Sofer, Z.; Simek, P.; Jankovsky, O. CoO and Co₃O₄ nanoparticles with a tunable particle size. *Ceram. Int.* **2014**, *40* (8), 12591-12595. DOI: 10.1016/j.ceramint.2014.04.082
- (86) Schrader, A. J.; Muroyama, A. P.; Loutzenhiser, P. G. Solar electricity via an air Brayton cycle with an integrated two-step thermochemical cycle for heat storage based on Co₃O₄/CoO redox reactions: Thermodynamic analysis. *Sol. Energy* **2015**, *118*, 485-495. DOI: 10.1016/j.solener.2015.05.045
- (87) Zyla, M.; Smola, G.; Knapik, A.; Rysz, J.; Sitarz, M.; Grzesik, Z. The formation of the Co₃O₄ cobalt oxide within CoO substrate. *Corros. Sci.* **2016**, *112*, 536-541. DOI: 10.1016/j.corsci.2016.08.016

- (88) Bernt, M.; Hartig-Weiss, A.; Tovini, M. F.; El-Sayed, H. A.; Schramm, C.; Schroter, J.; Gebauer, C.; Gasteiger, H. A. Current challenges in catalyst development for PEM water electrolyzers. *Chem. Ing. Tech.* **2020**, *92* (1-2), 31-39. DOI: 10.1002/cite.201900101
- (89) Garcia, A. C.; Koper, M. T. M. Effect of saturating the electrolyte with oxygen on the activity for the oxygen evolution reaction. *ACS Catal.* **2018**, *8* (10), 9359-9363. DOI: 10.1021/acscatal.8b01447
- (90) El-Sayed, H. A.; Weiss, A.; Olbrich, L. F.; Putro, G. P.; Gasteiger, H. A. OER catalyst stability investigation using RDE technique: A stability measure or an artifact? *J. Electrochem. Soc.* **2019**, *166* (8), F458-F464. DOI: 10.1149/2.0301908jes
- (91) Hartig-Weiss, A.; Tovini, M. F.; Gasteiger, H. A.; El-Sayed, H. A. OER catalyst durability tests using the rotating disk electrode technique: The reason why this leads to erroneous conclusions. *ACS Appl. Energy Mater.* **2020**, *3* (11), 10323-10327. DOI: 10.1021/acsaem.0c01944
- (92) Tovini, M. F.; Hartig-Weiss, A.; Gasteiger, H. A.; El-Sayed, H. A. The discrepancy in oxygen evolution reaction catalyst lifetime explained: RDE vs MEA-dynamicity within the catalyst layer matters. *J. Electrochem. Soc.* **2021**, *168* (1), 014512. DOI: 10.1149/1945-7111/abdcc9
- (93) Liu, L.; Twight, L. P.; Fehrs, J. L.; Ou, Y.; Sun, D.; Boettcher, S. W. Purification of residual Ni and Co hydroxides from Fe-free alkaline electrolyte for electrocatalysis studies. *ChemElectroChem* **2022**, *9* (15), e202200279. DOI: 10.1002/celec.202200279
- (94) Friebel, D.; Bajdich, M.; Yeo, B. S.; Louie, M. W.; Miller, D. J.; Casalongue, H. S.; Mbuga, F.; Weng, T. C.; Nordlund, D.; Sokaras, D.; Alonso-Mori, R.; Bell, A. T.; Nilsson, A. On the chemical state of Co oxide electrocatalysts during alkaline water splitting. *Phys. Chem. Chem. Phys.* **2013**, *15* (40), 17460-17467. DOI: 10.1039/c3cp52981a
- (95) Risch, M.; Ringleb, F.; Kohlhoff, M.; Bogdanoff, P.; Chernev, P.; Zaharieva, I.; Dau, H. Water oxidation by amorphous cobalt-based oxides: In situ tracking of redox transitions and mode of catalysis. *Energy Environ. Sci.* **2015**, *8* (2), 661-674. DOI: 10.1039/c4ee03004d
- (96) Wang, H. Y.; Hung, S. F.; Chen, H. Y.; Chan, T. S.; Chen, H. M.; Liu, B. In operando identification of geometrical-site-dependent water oxidation activity of spinel Co₃O₄. *J. Am. Chem. Soc.* **2016**, *138* (1), 36-39. DOI: 10.1021/jacs.5b10525
- (97) Xu, Y.; Zhang, F. C.; Sheng, T.; Ye, T.; Yi, D.; Yang, Y. J.; Liu, S. J.; Wang, X.; Yao, J. N. Clarifying the controversial catalytic active sites of Co₃O₄ for the oxygen evolution reaction. *J. Mater. Chem. A* **2019**, *7* (40), 23191-23198. DOI: 10.1039/c9ta08379k